UCLouvain
Institute of Mechanics,
Materials and Civil Engineering

Modelling dike failure by overtopping coupling hydraulics and geomechanics

Nathan Delpierre

Thesis typescript submitted in partial fulfilment of the requirements for the Ph.D Degree in Engineering Science

Thesis Committee

Advisors	Hadrien Rattez	UCLouvain
	Sandra Soares-Frazão	UCLouvain
Jury	Mathieu Javaux	UCLouvain
	Frédéric Collin	ULiège
	Daniel Caviedes Voullième	Forschungszentrum Jülich
Chairman	Grégoire Winckelmans	UCLouvain

Louvain-la-Neuve, March 2026

"Geotechnical engineering is the art and science of developing safe and workable solutions to unsolvable problems, armed with inadequate data and insufficient budget."

— H. Bolton Seed

Remerciements

Au moment de conclure cette thèse, je voudrais remercier toutes les personnes qui ont contribué à rendre ces années de recherche si agréables et passionnantes.

Mes premiers remerciements sont pour mes promoteurs de thèse, les Professeurs Sandra Soares-Frazão et Hadrien Rattez. Je les remercie vivement pour l'opportunité qu'ils m'ont donnée, il y a presque 4 ans, de démarrer une thèse dans leurs équipes respectives. Je les remercie également pour leur encadrement quotidien, leurs conseils avisés, les nombreuses discussions spontanées sur mes recherches. Il me semble difficile de dire en quelques phrases l'admiration que j'ai pour eux, pour leur dévouement au monde de la recherche et pour leur capacité à mettre en perspective, et à toujours trouver de nouvelles idées.

Je remercie chaleureusement les membres de mon jury de thèse, les Professeurs Daniel Caviedes-Voullième, Frédéric Collin et Mathieu Javaux pour leurs précieux commentaires et suggestions qui ont grandement contribué à la finalisation de ce travail. Merci également au Professeur Grégoire Winckelmans d'avoir accepté de présider le jury de thèse.

La réalisation de cette thèse n'aurait pas pu être aussi agréable sans la contribution enthousiaste de tous les chercheurs du pôle GCE, présents et passés. La bonne ambiance qui règne dans le pôle m'a procuré un vrai complément de motivation et m'a toujours rendu heureux de venir travailler au Vinci.

Je voudrais adresser un merci particulier à mes amis pour tous les moments partagés ensemble et pour leur soutien qui m'est si précieux.

Merci à mes parents de m'avoir offert, ainsi qu'à ma soeur, un cadre si propice au développement de la curiosité et du goût de l'effort. Je voudrais les remercier tous les trois de m'avoir toujours soutenu au cours de mon parcours.

Pour finir, je voudrais remercier Marie-Thérèse, pour sa patience et ses encouragements au quotidien. Nous formons une excellente équipe, qui n'est encore qu'au début d'un superbe voyage.

Contents

Contents **3**

1 Introduction **5**

2 Modelling dam breaching with a sediment transport-based approach **29**
2.1 Context 32
2.2 Experimental setup 36
2.3 Measurement techniques 37
2.4 Experimental results 41
2.5 Numerical models 47
2.6 Discussion of the numerical simulations and the experiments . 52
2.7 Conclusion 57

3 Coupled surface-subsurface flow modelling in earth dikes **61**
3.1 Context 64
3.2 The Richards equation and flow in unsaturated porous media . 66
3.3 Finite-volume resolution of the Richards equations 74
3.4 Coupling between Richards and shallow water equations 79
3.5 Model validation 82
3.6 Conclusion 87

4 Slope failure initiation in unsaturated earth dikes: shear strength reduction method **89**
4.1 Context 92
4.2 On stress variables in unsaturated soils mechanics 95
4.3 Model application to dike failures 102
4.4 Rainfall-induced shallow landslide 113

4.5 Conclusion 121

5 Slope failure propagation in unsaturated earth dikes: Particle Finite Element method 125
5.1 Context 128
5.2 The Particle Finite Element Method 133
5.3 Application in the classical Cauchy mechanics framework . . . 139
5.4 Cosserat continuum theory to mitigate mesh dependence . . . 159
5.5 Conclusion 168

6 Proof-of-concept for a coupled hydraulics and geomechanics model 171
6.1 Description of the model 173
6.2 Erosive failure of the dike 174
6.3 Downstream slope failure scenario 176

7 Conclusion 183

Bibliography 189

CHAPTER 1

Introduction

The impact of floods has always been a major concern for human societies. The devastating consequences are easy to understand: houses are destroyed, infrastructure is threatened and people are injured or killed. In order to counterbalance these tragic consequences, governments and local organizations developed strategies known as flood management. Flood management can refer to various methodologies that aim to mitigate the impact of floods on people and the economy. The most effective way to reduce the impact of floods would, of course, be to prevent people from building houses and carrying out economic activities in flood-prone areas. However, this is most of the time not possible. Indeed, historically, cities have been built along rivers or close to the sea, as these locations were favourable for trade and transport. This means that countermeasures must be taken to protect these areas from flooding or at least to reduce the impact of such events. These countermeasures can be categorized as either non-structural or structural.

Non-Structural measures
Generally speaking, these measures are defined by the UNDRR (United Nations Office for Disaster Risk Reduction, 2017) as measures that do not involve the construction of physical mitigation structures. These measures rather aim to reduce the risks by implementing forecasting strategies, early warning systems or improved land use planning. This type of measures will not be the focus of this work, nevertheless it is important to consider the role they play in a comprehensive flood management strategy.

Structural measures
The main focus of this work will be on the use of structural measures. This type of mitigation measure includes man-made infrastructures that allow to reduce risks and floods effects. Examples of structural measures include flood protection structures, retention basins, or underground drainage systems. These structures are designed to fullfill various goals, e.g. reducing the maximum runoff quantity, reducing the peak discharge, or delaying the time to peak.

Among the structural measures, dikes play a key role in flood defence but also in water resource management or energy production. Constructed from locally excavated earth, they offer a simple solution for

protecting flood-prone areas. In the North of Belgium and the Netherlands, millions of people are living under the current sea-level. They are thus greatly dependent on the proper functioning of these structural measures. For the Netherlands only, a 22000 km long network of dikes has been developed, while the country only counts 880 km of coastline. The role of these geotechnical structures is not limited to flood defence. They are also facilitating fluvial transport and are widely used for the disposal of mining wastes. Most of the time, dikes are integrated in a larger flood defence system that can include pumps, adjacent channels, bypasses or detention basins. The consequences of their failure can be severe, resulting in human casualties, destruction of cities, and damage to infrastructure.

Some terminological clarifications: The attentive reader who is not particularly familiar with civil engineering vocabulary may be confused by the terms employed. To avoid any confusion, the terms dam, dike, levee, and embankment are defined below. Note that these four terms will be interchangeably used throughout this work.

Dam: is a barrier that is constructed to retain water. It is typically built across a river or a stream to create a reservoir or to control water flow. In the context of mining, dams are used to store mining waste. In these cases, the term tailings dam is often used.

Dike: are built along the rivers, parallel to the water flow. Their main purpose is to prevent flooding for the protected areas but also to maintain water levels for navigation or irrigation.

Levee: is a term interchangeably used with dike.

Embankment: is a more generic term to describe a man-made earth structure. So it can refer to both dikes and dams.

What is a dike?

Defining dikes as an engineered structure is an important step before going further. Dikes were historically designed with a low level of engineering, their height being defined based on historical floods events and their structure being made using locally excavated soils. In the Netherlands, an important part of the dike network is made of peat, a material with poor mechanical properties and sensitive to the water content variations (Bezuijen et al., 2005). Nowadays, dikes are designed using a higher level of engineering. Danka and Zhang (2015) distinguish two types of engineered dikes: earthen dikes and composite dikes (see Figure 1.1).

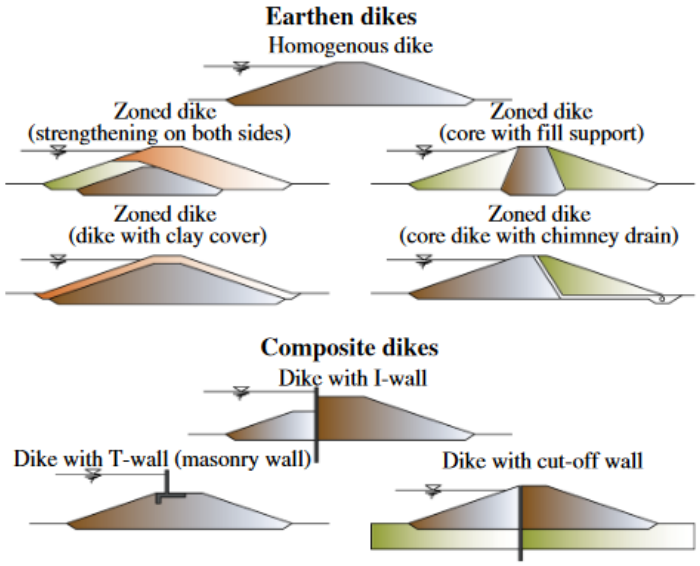


Figure 1.1: Classification of dikes following Danka and Zhang (2015).

Generally speaking, it is convenient to build a homogeneous dike with fine-grained material, such as clay. This type of material presents a low permeability and a high resistance to erosion. However, in many cases zoned dikes are built. These dikes rely on the use of a clay core or a clay cover (see Figure 1.2). The rest of the material is generally sand, silt or material excavated on site. In some cases, designs can be more complex when geotextiles, rock fills, and sheet piles are used. Figure 1.3 illustrates the design of a dike slope in Vlassenbroek, Belgium. The slope



Figure 1.2: Personnal picture of a dike crest that was cut for dike rehearsal purpose in Vlassenbroek, Belgium. A very thin clay cover is visible at the top, while the rest of the dike is made of sand.

is reinforced with geotextiles, covered with a tar layer and a clay cover. The goal is to increase the dike resistance to erosion during important overflow events.

The tragic consequences of dike failures

Wallace et al. (2024) report that around 10% of the world population lives in areas protected by dikes. In the current context of climate change and ageing infrastructures, failures in such structures present high risks for stakeholders and neighbouring communities, with potentially devastating consequences such as human life losses, material or environmental damages. Recent examples include the environmental disaster in Brumadinho, Brazil (2019) where a tailings dam failed causing 259 casualties and releasing 11 million of cubic meters of mining waste downstream (Rotta et al., 2020).

Other examples are the levee failures, depicted in Figure 1.4, in New Orleans (2005) during Hurricane Katrina leaving the city completely flooded for several days, the intense rainfall of July 2021 causing dike failures in the Netherlands and Belgium (Meersen in South Limburg, Herk-de-Stad in Limburg) and the 2013 floods along the Elbe River in Germany causing multiple failures.



Figure 1.3: Personnal picture of a dike slope built with geotextiles, tar and clay cover in Vlassenbroek, Belgium.



Figure 1.4: Levee breaching in New Orleans during Hurricane Katrina (2005) ASCE/EWRI Task Committee on Dam/Levee Breaching (2011).

A particularly striking example occurred in September 2023 in the city of Derna, Libya, which experienced the devastating aftermath of two

consecutive dam failures following an exceptional rainfall with a return period exceeding 1000 years (Storm Daniel). The Mansour dam, depicted in Figure 1.5, located 12 km upstream of Derna and designed to hold 22.5 million cubic meters of water, collapsed after an overtopping event following the intense rainfall. The massive volume of water cascaded towards the Derna dam, located near the city, triggering a second dam failure. This chain of events resulted in impressive discharges that simply wiped out important areas of the city, with an estimated 11000 to 24000 deaths reported by Nemnem et al. (2025). This example, among many others, illustrates how dike failures worsen floods as they suddenly release significant flows into areas intended to be protected.



Figure 1.5: The Mansour dam breaching in Derna, Libya (Gazzini, 2023).

The process of dike failure

The failure of a dike is defined by Morris et al. (2009) as "the situation where erosion or structural failure of the embankment allows the passage of flood water over or through the embankment in an increasingly uncontrolled manner".

Figure 1.6 depicts the various mechanisms through which dike failures can occur. A high pore pressure gradient inside the dike and poor material properties can lead to internal erosion and piping. This piping mechanism, visible in Figure 1.7, occurs when seepage flow detaches grains from the

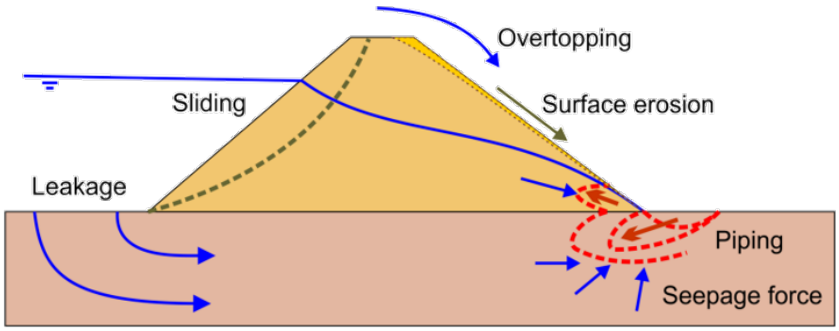


Figure 1.6: A sketch of the main dike failure mechanisms.

soil matrix, resulting in disastrous preferential flow in the dike. This internal flow can create a tunnel that will eventually collapse, leading to the dike breaching.



Figure 1.7: Breaching of an earthen dike due to piping (Morris et al., 2009).

Overtopping of the dam can also be disastrous, as water flowing over the crest can erode the downstream slope, leading to full breaching. This mechanism is illustrated in Figure 1.8.

General slope instability can also occur if the dike is subject to high levels of stress or if the mechanical properties are weakened by the wetting



Figure 1.8: Breaching of a cohesive earthen dike due to overtopping (Morris et al., 2009).

of the soil. In their work, Foster et al. (2000) compared the failure modes of 136 earth dam failures. Their analysis, synthetized in Figure 1.9, revealed that overtopping is the most common failure mechanism for earthen embankments, representing 34.2% of cases. Piping through the dam and piping through the foundation account for respectively 32.5% and 15.7% of the failures.

Danka and Zhang (2015) performed a similar analysis and also focused specifically on dikes. They compiled a database of 1000 failure cases and were able to identify the failure mechanism for 503 cases. Considering only the dike failures, 69% occured following overtopping and only 14% were due to piping (see Figure 1.10). Dikes are therefore more prone to overtopping failures than dams. Most of the time, dikes are not designed to withstand overtopping flows, while dams generally include a spillway to safely evacuate excess water.

Recently, Flynn et al. (2026) presented a dataset of 487 overtopping events that occurred in the U.S. The dataset was compiled from the Levee Loading and Incident Database, which contains aerial imagery, hydrographs and information on the width and depth of breaches. The aim of the dataset is to provide the maximum possible level of information to support the development of overtopping failure models. Özer et al.

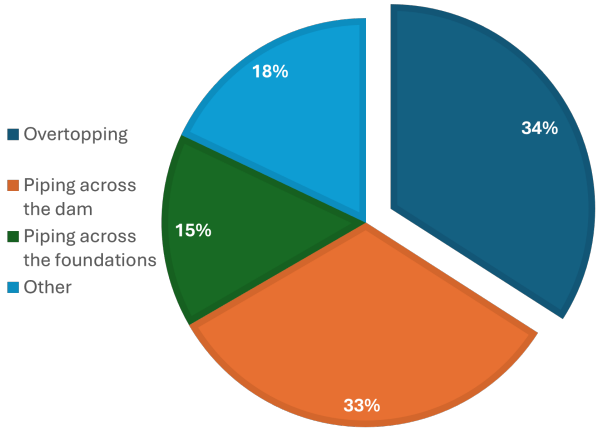


Figure 1.9: The distribution between failure modes in earth dams following Foster et al. (2000).

(2020) provide an International Levee Performance Database (ILPD) that includes information over 1500 events, mostly in Europe and in the U.S. The reported cases concern dikes along rivers in 89% of cases, with the remainder being along coastal areas. Interestingly, multiple dike failures were reported in 38% of cases. The authors also emphasise the importance of transparent data sharing for building a comprehensive database.

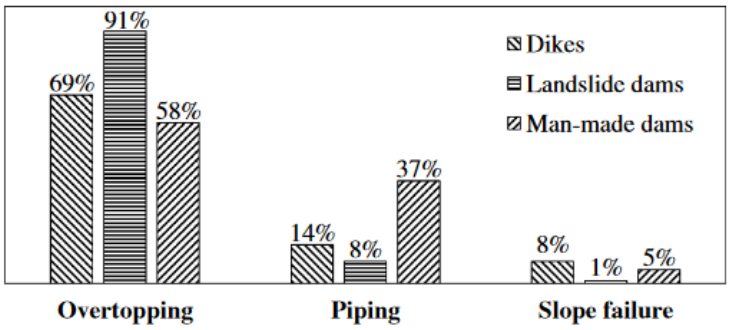


Figure 1.10: The distribution between failure modes in earth dikes following Danka and Zhang (2015).

For example, Sills et al. (2008) report that all dike failures observed during Hurricane Katrina in New Orleans (2005) were due to overtopping. This is why, considering the Northern-Western European context, this work will focus mainly on the overtopping failure mechanism.

Dikes and the broader context of geoscience and natural hazards
The competing effects of water flow, infiltration, and geomechanical failure are central to understanding multiple natural hazards. Landslides, floods, and mudflows share fundamental physical processes with dike failure, particularly the complex interactions between hydrodynamics, sediment transport, infiltration, and geomechanics. A comprehensive model for dike failure could therefore provide insights applicable to a broader range of geoscience hazards.

Landslide dams illustrate this interdependence of processes. When heavy rainfall triggers a landslide -as studied in Ivanov et al. (2020)- the resulting debris can impound water, creating a temporary dam. The water content's influence on mechanical stability is critical in both contexts: in determining landslide occurrence and in controlling subsequent dam failure dynamics. The overtopping or breaching of such landslide dams involves the same complex interplay of processes as engineered dike failures (Yang et al., 2024).

The effect of climate change on the occurrence of dike failure
Two phenomena exacerbate the risks of dike failures in the current global warming context. First, the sea-level rise, and second, increased extreme precipitations and drought events that put additional stress on water control structures. The increasing frequency of long droughts and extreme precipitation events leads earthen structures to undergo high variations of internal water content. Figures 1.11 and 1.12, retrieved from the 2021 IPCC report for policymakers (IPCC, 2021), illustrate these changes all around the world.

Belgium and more generally Northern-Western Europe will not be spared by these changes. A recent study by ULiège and the Royal Meteorological Institute of Belgium (RMI) predicts that a one-day rainfall event with a return period of 20 years could reach up to 100 mm, i.e. 100 l/m^2 (Brajkovic et al., 2025). This represents an increase of 20 to 25% compared to the current situation, knowing that the annual rainfall

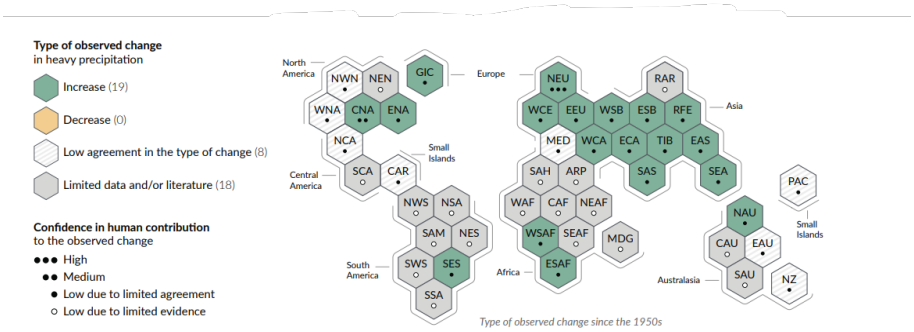


Figure 1.11: Assessment of observed change in extreme precipitation events IPCC (2021) since the 1950s.

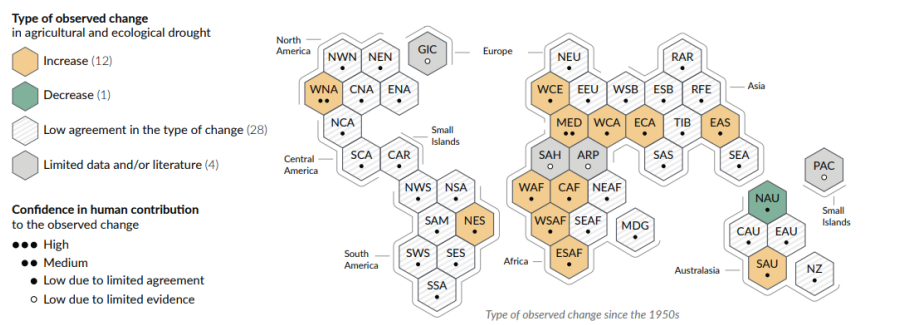


Figure 1.12: Assessment of observed change in extreme drought events IPCC (2021) since the 1950s.

in Belgium is around 850 mm.

Of course, such predictions vary depending on the climate scenario considered, but the trend is clear: extreme precipitation events are becoming more intense and more frequent. The return periods for extreme precipitation events considered for the design of earth structures are currently showing a significant decrease (Salas and Obeysekera, 2014). In other words, many structures designed in the past for events with, for example, a 100-year return period may now be undersized for the more intense events of the 21st century.

Note that both wet periods and droughts can negatively affect the mechanical properties of the soil in dikes. When long wet periods occur,

a decrease of shear strength of the soil is observed as it becomes closer to saturation. On the other hand, when long droughts occur, desiccation cracks might appear due to high suction (Tran et al., 2019), mostly in soils presenting a significant fine content, locally creating mechanically weaker zones and fast infiltration paths for water during subsequent rainfall events (Figure 1.13).

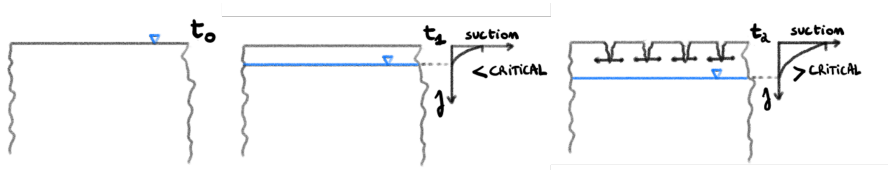


Figure 1.13: Apparition of dessication cracks in the soil. As the soil desaturates, the suction increases, eventually leading to cracks.

Flood mapping based on dike-breach modelling

Following the New-Orleans disaster, several research programs focused on improving the knowledge of the effect of dike failures on flood propagation in protected areas. Van Emelen et al. (2012) present a numerical and experimental study where they used a physical model at a 1:50 scale (depicted in Figure 1.14) to study the effect of the dike breaching along the 17th Street Canal on flood propagation in New Orleans. The dike was not included in the model (thus considered to have 0 thickness) and the breaching was considered to be sudden and instantaneous, both in the experiments and in the numerical simulations.

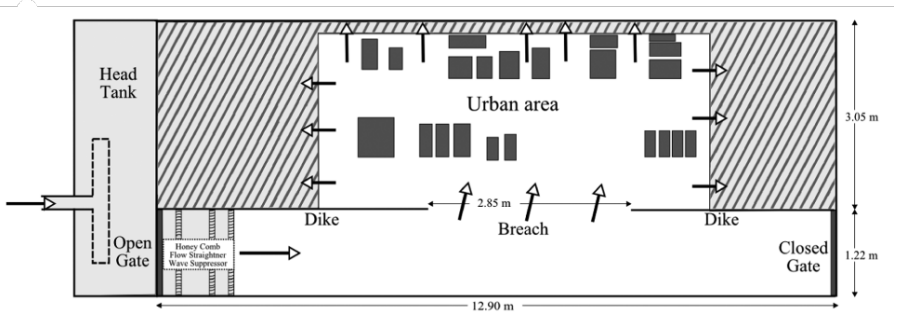


Figure 1.14: Scheme of the physical model at 1:50 scale of the 17th Street Canal in New Orleans retrieved in Van Emelen et al. (2012)

Here, we use this example to introduce the concept of flood mapping based on dike-breach modelling and adapt it to include a 0.95 m long dike. The dike is 0.2 m high with a 1:3 (vertical-horizontal) slope in the upstream part and a 1:2 slope in the downstream part. The crest is 0.05 m wide. The initial situation, before breaching is depicted in Figure 1.15.

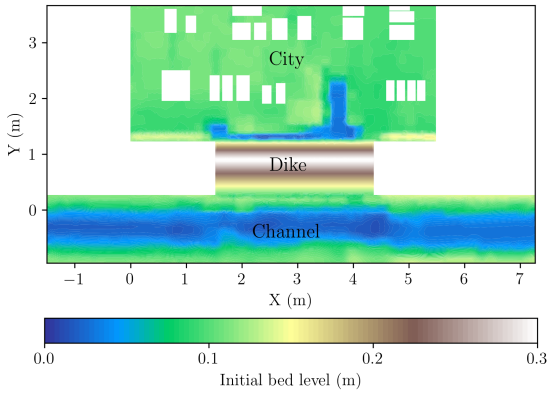


Figure 1.15: Bed level representation before the breaching of the dike.

To model the breaching scenario, a possibility would to simply remove the dike and let the water flow freely into the protected area. This is what we are considering here: simply removing the dike just before water reaches the crest, leading to the bed level represented in Figure 1.16. A constant input discharge of 0.057 m^3/s is imposed at the upstream boundary of the channel.

This constitutes a worst-case scenario. Still, it gives a first order of magnitude of the time it takes for water to reach the houses and of the water depth in the flooded area. This simulation [1] produces a very fast process, with the buildings being reached in a few seconds. Figures 1.17a and 1.17b present the water depth after 1 seconds and 5 seconds respectively.

However, in reality, the dike does not fail instantly, which could provide time for the evacuation of people and goods. The water discharge passing through the breach increases to a maximum value in a certain

[1] Performed using Watlab: https://sites.uclouvain.be/hydraulics-group/watlab/

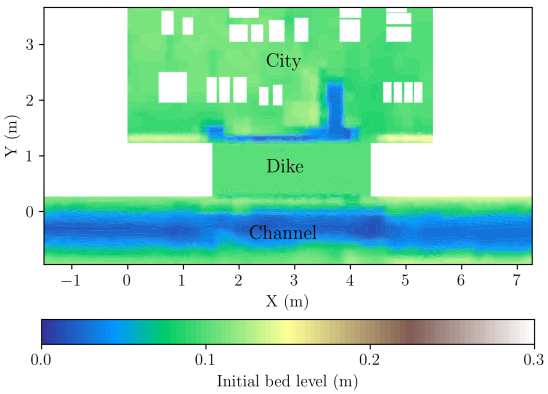
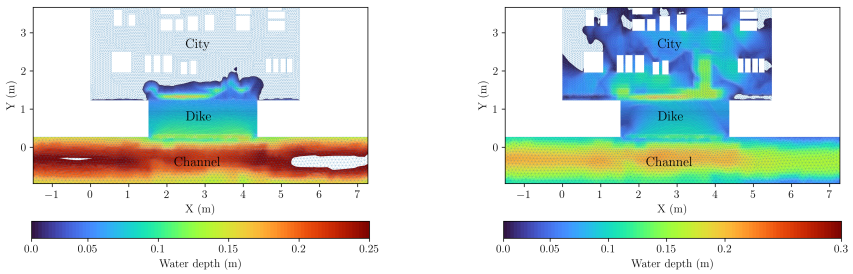


Figure 1.16: Bed level representation after the instantaneous breaching of the dike.



(a) (b)

Figure 1.17: Water depth in the protected area after the instantaneous breaching of the dike: (a) after 1 seconds, (b) after 5 seconds.

time, which depends on many parameters. The relation that links the discharge flowing through the breach and time is called a breach hydrograph. This hydrograph is the key parameter to accurately model the flood propagation in the protected area. An appropriate dike breaching model should therefore deliver this output hydrograph as accurately as possible.

Objectives of the manuscript

In the past pages, we discussed the importance of earthen embankments, and more specifically dikes, for flood defence and water resource management. We saw the dramatic consequences of potential failure and the main failure mechanisms. We have also highlighted that the impact of climate change on extreme meteorological events will increase the risks associated with the exploitation of these structures. For the reasons mentioned earlier, the main focus of the thesis will be on the failure of earthen dikes due to overtopping.

The main objective of the manuscript is to develop a numerical model that simulates the main steps of the process. The development of such a model is crucial for decision makers to gain better knowledge of the remaining time before a dike will break and of the volume of water that will pass through it once water begins to overflow. This information can be utilized as an input hydrograph for flood modelling, i.e. the relation that links time and discharge in the breach, to facilitate the creation of accurate and coherent flood maps, as discussed hereabove.

Building upon a state-of-the art model for dam breaching based on sediment transport, the manuscript aims at improving the physical modelling of the breaching. To achieve this goal, the effects of suction changes and geomechanical failure on the failure mechanism will be investigated in depth. Among the questions adressed in the manuscript, we can cite:

- Is it possible to fully capture the failure based only on sediment transport modelling?
- How can we track suction changes before and during an overtopping event?
- How does suction affect the shear strength of the soil?

- Can we relate a geomechanical safety factor to a given overtopping event?

- Should we consider large displacements of the geomaterial?

Organization of the manuscript
Several distinct steps can be identified during the overtopping failure of a dike. The various physical processes involved in dike breaching and their impact will be discussed in depth in the different chapters of the manuscript. This introduction aims at fixing the general steps of the work and to link these steps to the actual physical process. To illustrate the different steps, we will refer to an overtopping experiment performed at the Hydraulics Laboratory of the Direction des Recherches Hydrauliques (Service Public de Wallonie, Belgium). This experiment is described in depth by Ebrahimi et al. (2025). It consists of the overtopping of a medium-scale, 1-meter-high, 3.6-meter-wide, and 6.5-meter-long homogeneous sandy dike.

1. Modelling dam breaching with sediment-based approach
Figure 1.18 shows the initiation of the erosive process. As water starts



(a) Side view of the initial erosion process.

(b) Top view of the initial erosion process.

Figure 1.18: Initiation of the erosive process during dike overtopping: (a) side view, (b) top view.

flowing on the downstream slope, the sand is eroded. The erosion is initially more pronounced at the toe of the slope where a channel begins

to form. Then, the channel widens and progresses in a retrogressive manner towards the crest of the dike.

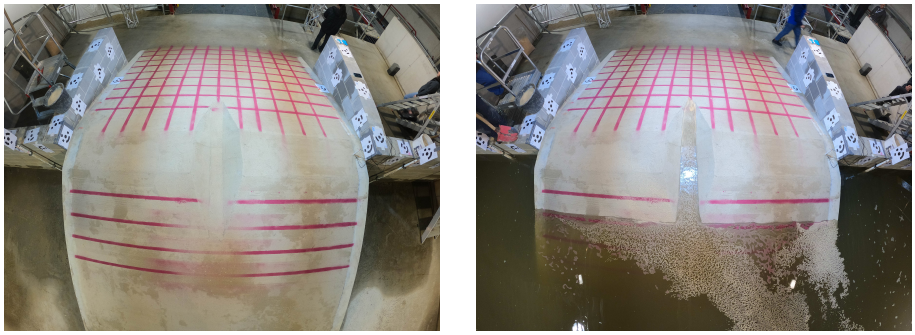
This process will be analysed in depth in Chapter 2, using numerical simulations of the experiments. This chapter describes the shallow-water-Exner equations that govern the flow and a sediment transport-based approach to model non-cohesive dike failure. The model used in the Chapter is part of the open-source software Watlab, developed at in the Hydraulics Group of UCLouvain.

In the field of hydraulic engineering, this approach dominates the literature when it comes to dam breaching or more generally sediment transport problems. The presented sediment transport model based on Soares-Frazão and Zech (2011) is enhanced by the presence of a bank failure operator (Swartenbroekx et al., 2010). This feature accounts, in a simplified manner, for the cohesive block failures on the side of the main breaching channel based only on a calibrated friction angle. Experimental results of a small-scale sandy dam breaching conducted at the LEMSC laboratory are presented and compared to 1D and 2D numerical simulations. The results demonstrate the model's effectiveness in accurately tracking bed level evolution during the event. The discussion addresses the difficulty the bank failure operator faces in following the breach widening during the process. This observation is a cornerstone of the problem. The bank failure operator is difficult to calibrate because it attempts to account for too many physical processes within the same simplified framework. A dry sandy dike will definitely not behave in the same way as a wet dike under the same overtopping flow.

Some questions arise from these first observations: how does the water content influence the geomechanical properties of the soil? How could we account for the meteorological history of the dike in the model? And how could we model the failure of a dike made of cohesive soil?

2. Coupled surface-subsurface flow modelling in earth dikes
Chapter 3 presents the development of a coupled surface-subsurface flow model. This model is based on the principle that pore pressure and degree of saturation are key factors controlling dike stability that should be tracked. Applied to dike overtopping scenarios, it simulates the conditions preceding the overtopping event, such as rainfall episodes, drought periods, and rising, or oscillating, water levels. Considering

the dike breaching case in the Chatelet laboratory, this model could be applied to precisely predict the evolution of the water content from the initial empty condition (see Figure 1.19a) to the time at which the reservoir is filled with water (see Figure 1.19b).



(a) (b)

Figure 1.19: Filling of the reservoir when infiltration and water content evolves in the dike: (a) empty reservoir, (b) full reservoir.

This chapter presents the physical principles governing flow in unsaturated porous media, including the soil-water retention curve and the unsaturated hydraulic conductivity. The laboratory measurements of these properties are also discussed. To model the progressive saturation process, the Richards equation (Richards, 1931), which describes flow in porous media and provides the spatial distribution of pore pressure and saturation degree, is solved using a finite volume scheme. Benchmarks are presented to validate the developed numerical model. Finally, the Richards equation model is coupled with a 1D shallow-water equations model (Franzini and Soares-Frazão, 2016), which is part of the Watlab software, in order to simulate dike overtopping scenarios. A benchmark case retrieved from the literature is presented to demonstrate the capabilities of the model.

3. Effective stress and shear strength reduction method

Chapter 4 focuses on the effects of pore pressure and saturation degree on the geomechanical strength of the soil. Figure 1.20 shows an example of block failure during the breach widening, which is a process that is highly influenced by the suction and by the geomechanical properties of

the soil.

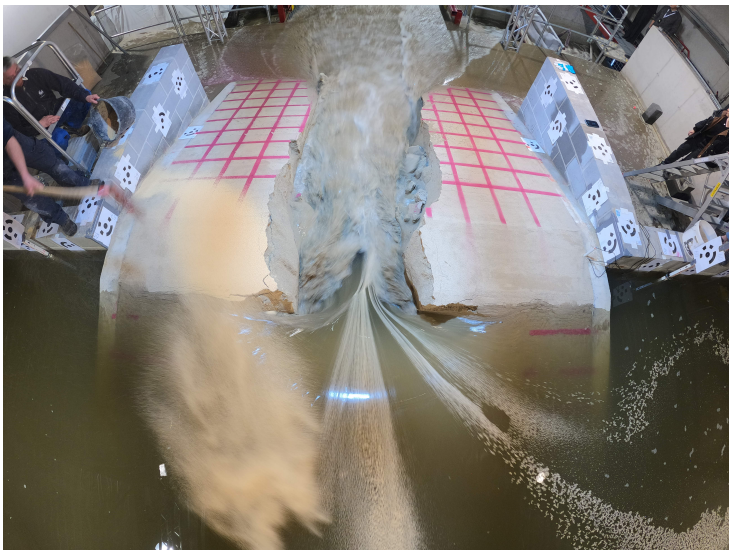


Figure 1.20: Block failure during the breach widening.

This chapter constitutes the first step towards the geomechanical approach proposed in this thesis. It is dedicated to the description of constitutive models for unsaturated soils mechanics. The selected approach based on the effective stress principle, based on Alonso et al. (2010), will be presented in depth. The principle of the shear strength reduction method is recalled. This method is frequently used in geomechanics, in combination with the finite element method, to detect potential shear failure lines and to associate a safety factor to a given situation.

The MOOSE framework (Lindsay et al., 2022; Giudicelli et al., 2024), an open-source Multiphysics Finite Element framework, is used to implement the effective stress approach and to solve the geomechanical problem. The geomechanical model is coupled with the previously presented surface-subsurface flow model to analyze dike slope stability during overtopping. Several cases of longitudinal dike instabilities are examined under idealized overtopping conditions. A benchmark case from the literature is presented to validate the coupled model. It consists of a longitudinal dike slope failure induced by overtopping flow. The model performs very well in predicting the time and location of the failure.

In this chapter, an additional study, performed in collaboration with a research group from Politecnico di Milano (Italy), is also presented. This study investigates the performance of the effective stress approach combined with the shear strength reduction method and the developed Richards equation solver to simulate rainfall-induced landslides. The model is applied to small-scale laboratory experiments performed in Lecco, Italy.

4. Large displacements: the Particle Finite Element Method
Chapter 3 and Chapter 4 are dedicated to the detection of potential failure of a dike. Nevertheless, once the failure is detected, the model is unable to track the post-failure mechanism since the classical finite element method framework is not suitable for large displacements as those resulting from block failures.

Chapter 5 is dedicated to the precise evaluation of the failure mechanism. The chapter will present the various possible approaches to model large displacements in geomechanics. In particular, the Particle Finite Element Method (PFEM, Oñate et al. (2004)) is described and its application to solid mechanics is developed. This Lagrangian method, that is based on an efficient remeshing strategy, is particularly suited for the problem we want to address. The remeshing algorithm developed by Leyssens (2025) is combined with the MOOSE framework to solve the geomechanical problem in a PFEM context.

The chapter will present various test cases of geomechanical problems solved with PFEM, such as slope instability, granular column collapse or retrogressive landslides. We will discuss the influence of constitutive models. Specifically, we will see that the PFEM does not address strain localization issues or mesh dependence in the case of strain softening. This problem, very specific to computational geomechanics, will be discussed in depth.

Various regularization techniques exist to mitigate this problem. Some of them will be discussed in this chapter. In particular, the Cosserat theory will be presented and combined with the PFEM framework.

5. A proof-of-concept for dike breaching modelling
Chapter 6 provides a proof of concept for the developed modelling framework for dike breaching. The various components introduced in

previous chapters are combined to simulate the overtopping failure. The New Orleans small-scale physical model is used again, but instead of removing the dike instantaneously, overtopping failure is modelled by coupling the different components. The effect on the output breach hydrograph is analysed.

Graphical Abstract of the thesis

Figure 1.21 presents a graphical abstract of the thesis. It summarizes the different steps of the thesis work. The figure recalls the main phenomena driving the overtopping failure of a dike which are explored in the different chapters.

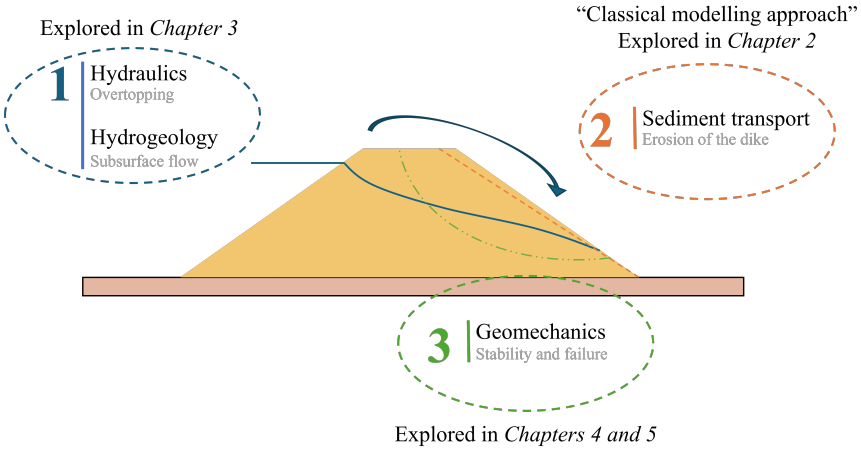


Figure 1.21: Graphical abstract of the thesis.

Publications linked to the thesis

1. Delpierre, N., Rattez, H., Soares-Frazao, S., 2023. Finite-volume coupled surface-subsurface flow modelling in earth dikes. Journal of Hydraulic Research 61, 754–763.

2. Delpierre, N., Franzini, F., Gousenbourger, P.Y., Van Emelen, S., Zech, Y., Soares-Frazao, S., 2024. Breaching of sand dikes: Assessment of 1d and 2d numerical models against laboratory experiments. Journal of Hydraulic Research 62, 461–475.

3. Delpierre, N., Rattez, H., Soares-Frazão, S., 2025. Surface–subsurface flow effect on earthen dikes geomechanical stability during overtopping event. Geomechanics for Energy and the Environment 43, 100709.

4. Panzeri, L., Delpierre, N., Scaioli, A., Rattez, H., Papini, M., Longoni, L., 2025. From small-scale laboratory physical tests to the shear strength reduction method in unsaturated soils. Engineering Geology Under review.

Publications not linked to the thesis

1. Delpierre, N., Ebrahimi, M., Bertholet, A., Scaioli, A., Panzeri, L., Longoni, L., Rattez, H., Soares-Frazão, S., On the use of distributed optical fibre sensors to complement photogrammetric measurements of experimental dike breaching, Journal of Hydraulic Research (Special Issue on dam breaching), Under review.

Conference participation

1. Delpierre, N., Soares-Frazão, S., Rattez, H., Coupled surface and subsurface flows for earthen embankments using finite-volume methods, poster, EGU 2023.

2. Delpierre, N., Soares-Frazão, S., Rattez, H., Finite-volume coupled surface-subsurface flow modelling in earthen dikes, Presentation, IAHR 2023.

3. Delpierre, N., Soares-Frazão, S., Rattez, H., Finite volume method for coupled surface-subsurface flows with geotechnical stability evaluation, Presentation, World Landslide Forum 2023.

4. Zech, Y., Delpierre, N., Gousenbourger, P-Y., Soares Frazao, Sandra. Flood interpretation in case of measurement failure. The Wamme River in 2021. Proceedings of the Riverflow 2024 Conference.

5. Ebrahimi, M., Delpierre, N., Gilles, Arthur, Zgajewski Delforge, C., Swartenbroekx, C., Bousmar, D., Soares-Frazão, S., Monitoring medium-scale dike breaching using photogrammetry: preliminary results. Proceedings of the Riverflow 2024 Conference.

6. Delpierre, N., Leyssens, T., Rattez, H., Soares-Frazão, S., PFEM to simulate earthen dikes failure due to overtopping: A coupled surface-subsurface approach, Presentation, Alert Geomaterials 2024.

7. Delpierre, N., Leyssens, T., Rattez, H., Soares-Frazão, S., PFEM in Moose: modelling earthen dikes breaching due to overtopping, Presentation, Moose Workshop 2025.

8. Delpierre, N., Leyssens, T., Rattez, H., Soares-Frazão, S., Modelling earthen embankment failure using the Particle Finite Element Method, Presentation, Simhydro 2025.

9. Ebrahimi, M. Delpierre, N., Swartenbroekx, C., Bousmar, D., Soares Frazao, S., Investigating the effects of overtopping conditions on dike breach evolution through medium-scale laboratory experiments. Proceedings of the 41st IAHR World Congress, 2025

CHAPTER 2

Modelling dam breaching with a sediment transport-based approach

This chapter focuses on sand dike failure by overtopping and is based on a paper published in the Journal of Hydraulic Research (Delpierre et al., 2024). Sandy dike breaching experiments by overtopping were carried out in the LEMSC laboratory. The impact of the grain size was studied by comparing a fine and a coarser sand. The failure mechanisms look similar in both cases, but some differences could be observed in the evolution of the geometry of the dike. The failure was simulated with 1D and 2D sediment transport models equipped with a bank failure module. The 1D model shows good results for the initial stage of the dike evolution and in predicting the evolution of the width of the breach. The 2D model predicts the morphological evolution more accurately but overestimates the widening of the breach, highlighting the difficult calibration of the bank failure operator.

Contents

2.1 Context **32**

2.2 Experimental setup **36**

2.3 Measurement techniques 37
2.4 Experimental results 41
2.4.1 Breaching process 41
2.4.2 Evolution of the breach geometry 43
2.4.3 Evolution of the water level and discharge . 46
2.5 Numerical models 47
2.5.1 One-Dimensional model 47
2.5.2 Two-Dimensional model 51
2.6 Discussion of the numerical simulations and the experiments 52
2.6.1 Comparison with the one-dimensional model 53
2.6.2 Comparison with the two-dimensional model 54
2.7 Conclusion 57

Symbol	Description	Units
d_{50}	median grain diameter	m
ε_0	bed porosity (after compaction)	– (%)
s	specific gravity of sediment	–
n	Manning friction coefficient	$\mathrm{s} \cdot \mathrm{m}^{-1/3}$
φ_{dry}	dry friction angle	$^\circ$
φ_{wet}	wet friction angle	$^\circ$
Q_{in}	upstream discharge	$\mathrm{m}^3 \cdot \mathrm{s}^{-1}$
A_r	reservoir surface area	m^2
z_w	reservoir water level	m
Q	breach discharge	$\mathrm{m}^3 \cdot \mathrm{s}^{-1}$
x	longitudinal coordinate	m
Q_s	sediment discharge	$\mathrm{m}^3 \cdot \mathrm{s}^{-1}$
B	1D channel width	m
g	gravity	$\mathrm{m} \cdot \mathrm{s}^{-2}$
R	hydraulic radius	m
S_f	friction slope	–
θ_{cr}	critical Shields parameter	–
$\boldsymbol{U}$	conserved variables vector	mixed
A	water area	m^2
A_b	sediment area	m^2
I_1	hydrostatic pressure term	m^3
I_2	lateral pressure term	m^2
$\mathbf{H}$	morpho-coupling matrix	–
B_s	equivalent average sediment width	m
Δz_b	bed elevation change	m
ΔA_b	sediment-area change	m^2
Δt	time step	s
Δx	cell length	m
Ω_i	2D cell area	m^2
L_j	face length	m
u, v	velocity components	$\mathrm{m} \cdot \mathrm{s}^{-1}$
h	water depth	m
q_x, q_y	unit discharges	$\mathrm{m}^2 \cdot \mathrm{s}^{-1}$
z_b	bed level	m
q_{sx}, q_{sy}	sediment discharge components	$\mathrm{m}^2 \cdot \mathrm{s}^{-1}$
S_{fx}, S_{fy}	friction slopes	–
$\mathbf{R}_j$	rotation matrix	–
$\overline{F^*}$	numerical flux	mixed

2.1 Context

The present chapter focuses on overtopping failure of non-cohesive uniform sandy dikes. This type of failure has been studied extensively over the last decades because non-cohesive fill dikes are the most sensitive to surface erosion, which Morris et al. (2009) identifies as the primary failure mechanism for such materials. Visser (1998) first described the failure process for fine sand dikes by clearly identifying the different steps of the breach widening. These steps, illustrated at Figure 2.1, constitute a consensus in the hydraulics community since a number of studies have observed the same behaviour (Morris et al., 2009).

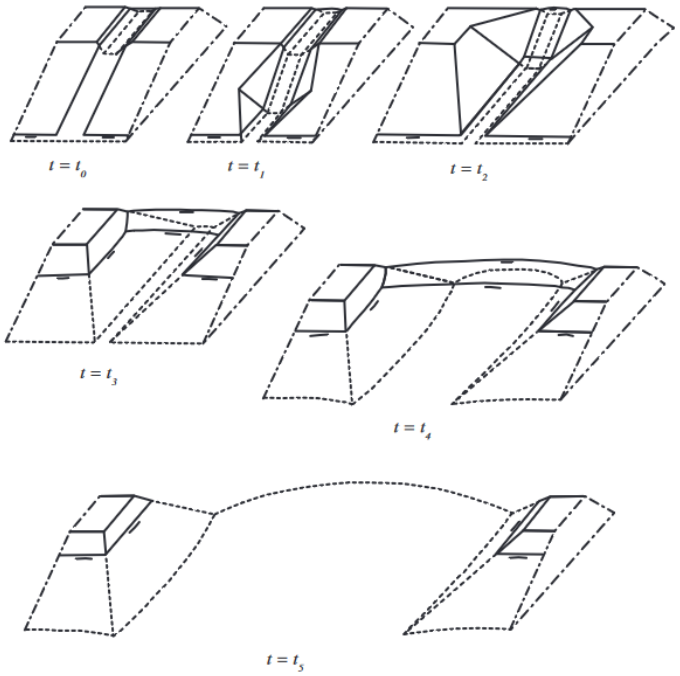


Figure 2.1: Stages of breach widening in non-cohesive material as described by Visser (1998).

The first step (depicted as t_0 in Figure 2.1) starts as soon as water overtops the dike. The material is eroded and a channel is dug in the downstream slope. The channel's slope steepens and progresses

retroactively from the toe of the dike to the crest, forming the second step (t_1). During this step, the erosion channel may widen slightly. The third step (t_2) begins as soon as the channel's backward progression reaches the rear of the crest. From this point, the breach will widen at higher rate following lateral block failures. During such failures, the sides of the breach can remain almost vertical before failing by blocks. The Visser's theory highlights the cohesive behaviour of fine sand that is not expected from non-cohesive material. This is a first hint that the suction, or capillary, effects, may play an important role in the breaching process of dikes.

On the other hand, Coleman et al. (2002) extended the study to coarse non-cohesive sand dikes and highlighted the presence of a pivot point, depicted at Figure 2.2, around which the bottom of the breach rotates while being eroded. This pivot point was also observed in the results presented in Delpierre et al. (2024) and recalled in this chapter.

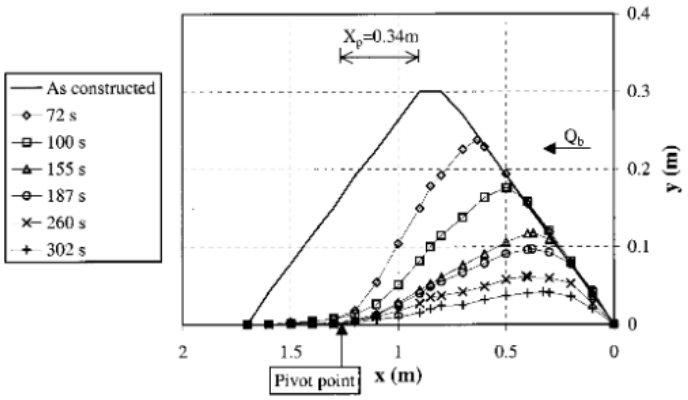


Figure 2.2: Longitudinal profile of the non-cohesive dike breaching performed by Coleman et al. (2002) where the pivot point is visible.

These theories have been further enhanced by Zhang et al. (2017) and Zhou et al. (2019). Experiments usually focus on the influence of parameters such as the sediment nature, dike height and discharge (Schmocker and Hager, 2012), the grain size distribution (Schmocker et al., 2014), the shape and headwater elevation (Müller et al., 2016) or the material constituting an eventual pavement (Pan et al., 2015; Zhang et al., 2017).

As regards numerical simulations, the complexity of the ongoing physical processes and the associated variability make it difficult to model dike breaching in a comprehensive way. Therefore, many authors still rely on parametric breach models using regression equations to estimate the evolution of the failure mechanism and especially the outflow discharge (ASCE/EWRI Task Committee on Dam/Levee Breaching, 2011). Based on multiple case studies, laws describing relations between the overtopping flows and some physical parameters, like the breach width or water inflow, can be derived. Other approaches can be seen as semi-physical as they try to incorporate the geometry of the breach, considered as a rectangle or trapezoidal forms, and to describe its evolution in time considering some simplifications (ASCE/EWRI Task Committee on Dam/Levee Breaching, 2011).

Nevertheless, numerical models are very powerful tools to run predictive simulations. When models are validated by experiments, they can be used to predict the behaviour in real life and hence prevent damages. Many numerical models have now been developed to assess the risk of failure for dikes subject to overtopping flows with attempts to fully solve the physical process. Based on the idea that the breaching process is mostly dominated by erosion for non-cohesive dikes, most of the models consist in solving the shallow water equations combined with the Exner equation. These models build on specific transport laws and the resolution schemes assume equilibrium bedload transport conditions. That is, the transport rate instantaneously adapts to local flow specifications (Wu et al., 2012; Juez et al., 2014; Barzgaran et al., 2019; Meurice and Soares-Frazão, 2020). Recent works consider non-equilibrium bedload transport for dam breaching (Martínez-Aranda et al., 2023). They account for temporal and spatial delay of the sediment transport rate influenced by the flow capacity. Martínez-Aranda et al. (2021) made a specific comparison between equilibrium and non-equilibrium conditions and showed that, under appropriate calibration of the parameters, the non-equilibrium approach performed better in highly transient zones.

In such models, the difficulties to properly describe the process lie mainly in the variability of the material, such as mean grain diameter, compaction or water content. Many transport laws have been developed with often a particular range of application and a wide uncertainty on the results, making this choice critical for the quality of the simulation

as highlighted by Van Emelen et al. (2015). Note that literature provides mostly closure equations for non-cohesive sands. Theoretically, this hypothesis should always be satisfied as soon as the dike is made of sand coarse enough to be considered as non-cohesive. However, suction related to water content confers cohesion and may strongly alter the results. Chapter 3 and Chapter 4 will focus on considering the effects of saturation degree inside the dike.

The current Chapter has two goals. First, we publicly provide a new 1:1 experimental benchmark to the scientific community, with results of dike breaching by overtopping obtained with coarse and fine uniform sands. From the experimental side, an important and interesting development is the extensive use of the laser light sheets, already developed in prior works (Soares-Frazão et al., 2007), to precisely catch the morphological evolution of the breach in time and therefore to provide valuable data for numerical model validation. In addition to the high quality of the measured data, all the parameters required by modelers are provided. Another interesting aspect of the experimental results is the comparison between the behaviours of coarse and fine sand. The results show that the cohesive behaviour of fine sand, probably related to suction and saturation degree, leads to a higher peak discharge following lateral block failure. The described processes show interesting concordances with the Coleman et al. (2002) and Visser (1998) observations, which allow to validate the dataset.

Secondly, we compare this benchmark to one-dimensional and two-dimensional finite volume models based on the shallow-water-Exner equations augmented with a bank-failure operator. We show that the one-dimensional simulation based on the model of Franzini and Soares-Frazao (2018), although less accurate and physically less appropriate, provides acceptable results while using significantly less simulation time, and is thus a good quick first estimation. The two-dimensional model used in this paper also solves the shallow-water and Exner equations and is enhanced with a feature first presented by Swartenbroekx et al. (2010) as a bank-failure operator. This feature allows to consider a maximal slope angle for non-cohesive sand and therefore to represent the local mass failures by locally adjusting the bed level where the slope exceeds this angle. In fact, it also attempts to account for cohesive effects linked to suction by considering higher friction angles for zones that are not

submerged.

The current chapter is divided in five sections. Section 2.2 describes the experimental setup for the small-scale dike breaching. Section 2.3 describes the measurement techniques to capture the bed level evolution and the water evolution in time. Section 2.4 comments the experimental results concerning the breaching process and the evolution of the captured bed level at the different sections of measure. As this chapter tackles both experimental and numerical modelling, Section 2.5 describes the numerical one-dimensional and two-dimensional models, whose results will be compared with the experimental results in Section 2.6. Section 2.7 is dedicated to the conclusions.

2.2 Experimental setup

The breaching experiments were carried out at the Hydraulics Laboratory of the Institute of Mechanics, Materials and Civil Engineering (iMMC) of UCLouvain (Belgium). The set-up is illustrated in Figure 2.3 and consists of a full-scale dike constructed with an initial pilot breach. The flume is 12m long, 1.2m wide and 0.32m high. A pump supplies water to a 2-m long, upstream reservoir. The dike is built 2.88m downstream from the reservoir.

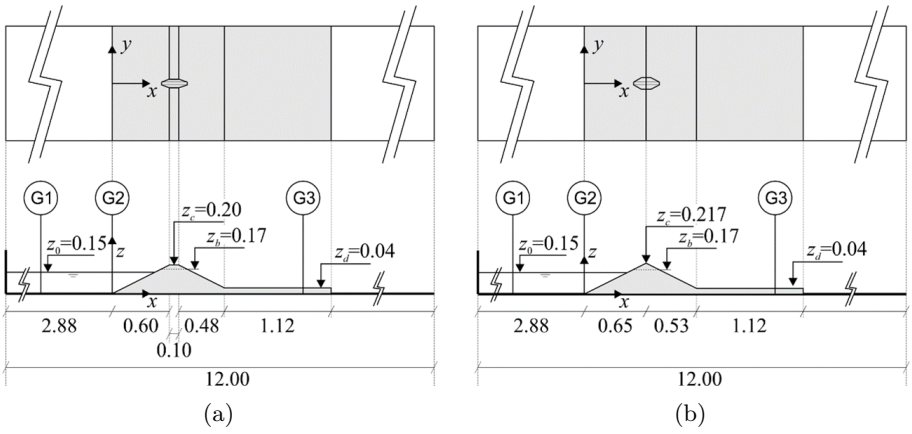


Figure 2.3: Experimental setup and dimensions of the dike made of (a) coarse sand and (b) fine sand. The only difference relies on the top of the dike. Distances are in metres.

Two dikes were built: one with coarse sand and one with fine sand Coarse sand has median diameter d_{50} = 1.7 mm, and bed porosity ϵ_0 = 45% after compaction. Fine sand has median diameter d50 = 0.71 mm, and bed porosity ϵ_0 = 44% after compaction. Both sands have a specific gravity s = 2.615. According to widely used formulas, the Manning friction coefficient should range from 0.014 $s.m^{-1/3}$ to 0.0167 $s.m^{-1/3}$. Finally, the friction coefficient n = 0.0167 $s.m^{-1/3}$, was determined from uniform flow experiments and chosen for both sands.

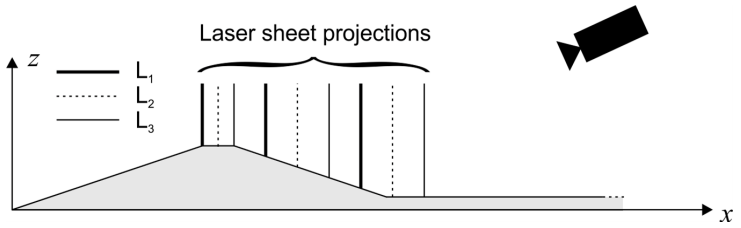
A friction angle of 30° is considered for submerged conditions while a friction angle of 85° is used for non-submerged conditions following Swartenbroekx et al. (2010). Note that the value of 85° is very high for sand and can be considered as a fitting parameter to account for the cohesive effects due to suction in the unsaturated zone.

Geometrically, the dikes are 1.3 m long and use the whole flume width (1.2 m) with 1:3 slopes, upstream and downstream. An initial trapezoidal breach is dug in each dike to initiate the failure process. The breach has a base width of 0.03 m with a 1:1 slope, and a sand level of 0.17 m at its centre. A sand layer of 1 m long and 0.04 m height is set at the downstream toe of the dike to avoid piping effects. The upstream part of the dike is initially filled with 0.15 m of water. When the experiment starts, the pump is activated to provide a constant discharge of 4 l/s. This discharge is kept constant during the whole experiment.

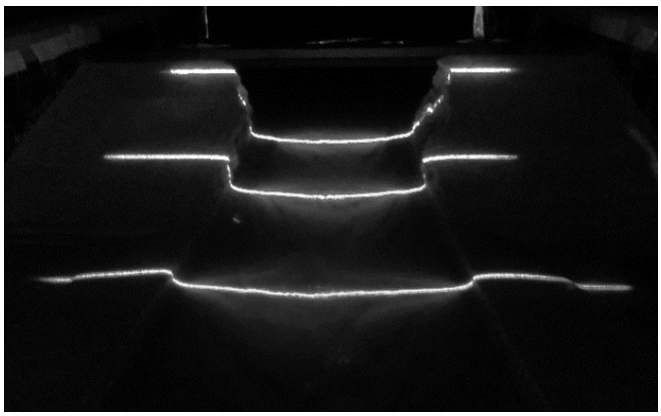
2.3 Measurement techniques

The monitored parameters in the experiments are the water and bed level evolution. These are captured using two types of measurement techniques: ultrasonic probes and laser-sheet. These two techniques have the advantage of being non-intrusive. This prevents any local influence of the measurement on the experiment. Three ultrasonic probes are used to determine the water level evolution at three locations as illustrated in Figure 2.3: just downstream of the reservoir ($x = -0.75m$), at the upstream toe of the dike (x = 0m) and on the downstream sand layer (x = 2.05 m). The bed level evolution is captured at nine different positions thanks to three laser-sheets (Soares-Frazão et al., 2007), as represented in Figure 2.4.

The experiments are run in a completely dark environment: the bed



(a)



(b)

Figure 2.4: Laser-sheet and camera measurements: (a) indication of the three series of measurements per test (see Table 1 for the exact positions), (b) a view from the camera for one series of measurements: the laser appears as a white line. Post-processing requires the shape of the breach to be extracted from these three lines.

level is then lit by the laser-sheets, which creates a thin visible red line. The red lines are captured by a camera, as illustrated in Figure 2.4. We assume that the impact of refraction is negligible given that the camera is placed in front of the dike (Soares-Frazão et al., 2007). This effect is further limited as the water depth over the dike is very small.

The bed profiles are extracted from the pictures using Matlab pre-processing. First, the pictures are orthorectified to remove deformations due to the camera lenses and position. Two deformations can occur (see Figure 2.5 for a clear example on a chessboard): barrel distortion (b) and perspective distortion (c).

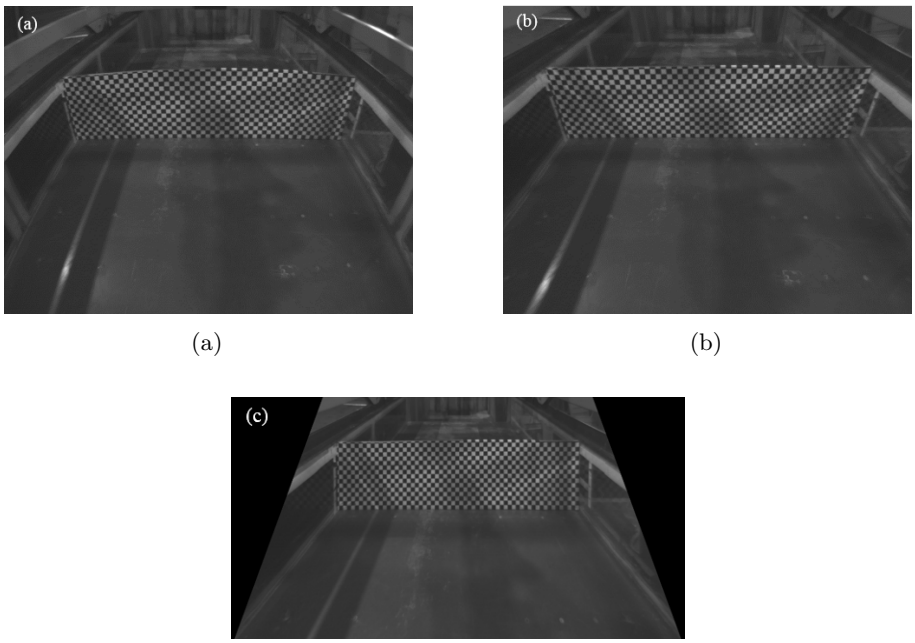


Figure 2.5: The initial acquired image (a) is subject to distortion. It is important to post-process the image. The figure shows the image after correction of the barrel effect (b) and the perspective distortion (c).

Secondly, the bedlevel lines are isolated, selecting the pixels with the highest contrast. Finally, the results are scaled using the ratio pixel/cm. To avoid noise effects due to the proximity of two consecutive lasers, we decided to acquire the bed level at only three positions by trial. The lasers are shifted after each trial in order to multiply the measurements: three trials are hence needed in order to obtain the nine measurements (see Table 2.1 for the nine positions and their associated trial).

Therefore, the repeatability of the data acquisition protocol is crucial to assess the validity of the measurements of the bed level evolution from one trial to another. Here, the validity has been assessed by performing three experiments where the dike was flush by water. During each experiment, we measured the bed level at three different locations. We then compared the results in Figure 2.6. The experiments were performed with fine sand and coarse sand (for a total of six trials). The results show

Table 2.1: Cross-sections measurements starting from the upstream foot of the dike

Cross-section	**Location (m)**	**Trial**
C1	0.60	A
C2	0.65	B
C3	0.70	C
C4	0.80	A
C5	0.90	B
C6	1.00	C
C7	1.10	A
C8	1.20	B
C9	1.30	C

visually strong similarities and enhance the confidence in the repeatability of the protocol. The RMSEs are computed for each gauge position and sand type. For coarse sand, the RMSEs are 0.57 mm (G1), 3 mm (G2) and 1.7 mm (G3). For fine sand, the RMSEs are 3 mm, 2.14 mm and 2.03 mm, respectively.

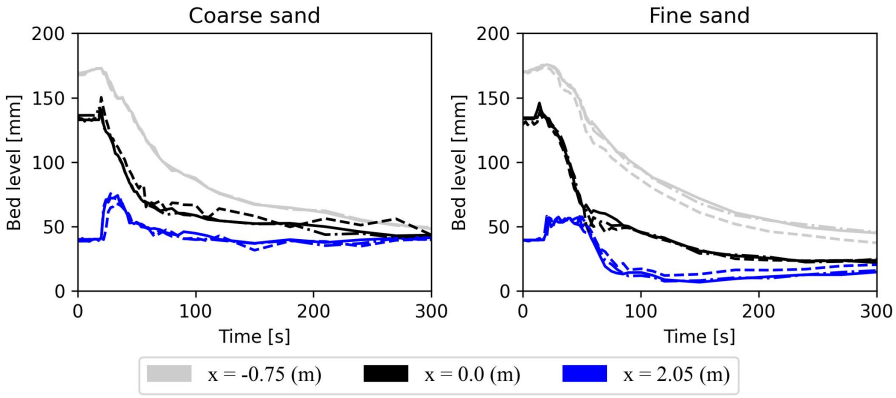


Figure 2.6: The repeatability of the protocol is assessed. The bed level evolution is compared for three different trials (solid, dashed, dash-dotted) at three different gauges positions (G1-grey, G2-black and G3-blue) for both coarse and fine sand.

2.4 Experimental results

This section presents the results from the experiments. It is divided in three parts. First, the general process of failure is presented. Second, the breach evolution is studied more closely. Third, the breach discharge is estimated using data on geometry and water level evolution. It is shown, in this section, that the data recorded during this experiment respects the expectations and follows the well-known models of Visser (1998) and Coleman et al. (2002). Therefore, the dataset can be considered as valid and is shared to the community as a new benchmark to study the breaching and the failure of sand dikes.

2.4.1 Breaching process

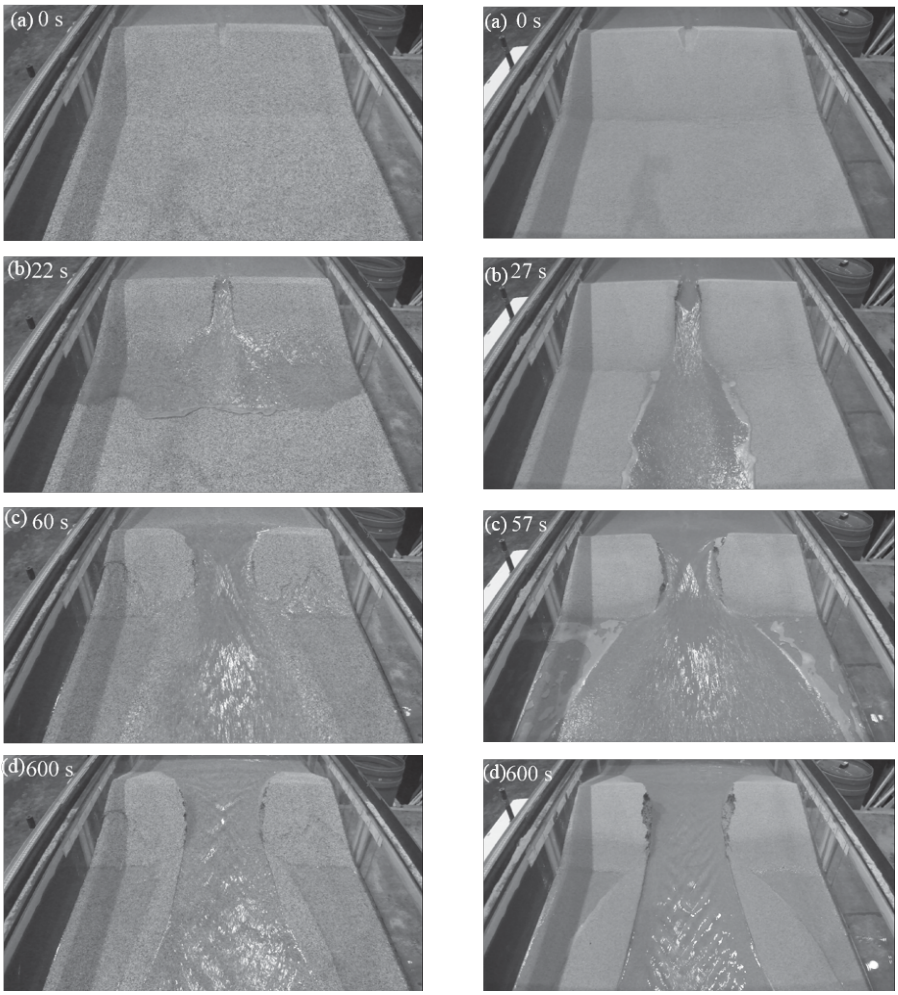
The failure mechanism observed for both types of sand confirms the three first stages of dike erosion observed by Visser (1998) and previously depicted at Figure 2.1. Figure 2.7 shows pictures of those stages appearing in the present experiments.

In stage I, we observe a steepening of the breach slopes until a critical angle is reached at t = t_1. This critical angle is reached at t_1 = 22 s for coarse sand and t_1 = 27s for fine sand. This might be explained by the additional cohesion generated by the finer sand matrix.

In stage II, the breach widens by erosion and the width of the crest decreases until it vanished at t = t_2. Stage II occurs at t_2 = 60 s for coarse sand and t_2 = 57 s for fine sand. The inflow grows.

In stage III, the deepening and widening continues until the dike in the breach is washed out down to the base of the dike. Stage III appears to be a steady state in our experiment. It occurs at time t = t_3 = 600 s for both grain sizes.

One important difference between the two grain sizes is the impact of seepage. As observed in Figure 2.7, at the toe of the coarse sand dike, a flow is observed. This flow is due to the seepage through the dike and is not present in the fine sand dike (Figure 2.7). However, the main failure mechanism is still the overtopping over the dike through the breach. We will see in the next section that both sand types result in the same breach evolution process.



(a) Coarse sand (b) Fine sand

Figure 2.7: Stages of breach evolution for (a) coarse sand and (b) fine sand.

2.4.2 Evolution of the breach geometry

Figure 2.8 (a) and (b) show the evolution of the dike along its centreline, in the direction of the flow. The process clearly shows similarities with the observations presented by Coleman et al. (2002) (p. 833, figure 6) as a pivot point clearly appears at the downstream toe in both cases. Coleman characterizes this particular juncture as a pivot due to the continuous erosion that causes the breach bottom to revolve around it over time. Unlike Coleman's observations, the pivot's position in both scenarios is consistently located beyond the initial construction of the dike toe.

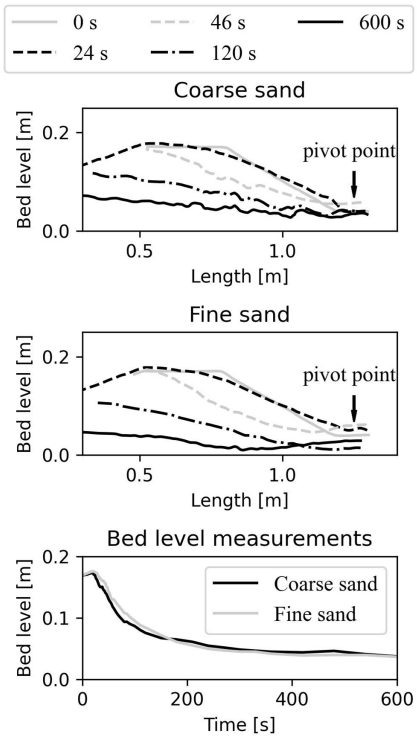


Figure 2.8: Validation of the theory of Coleman et al. (2002). Top: evolution of the bed level along the centreline of the flume: (a) coarse sand, (b) fine sand. Bottom: breach level evolution at the crest.

This occurrence is likely attributed to the presence of sand at the

downstream toe of the dike, as previously described. The presence of an erodible sand layer downstream of the dike is however more representative of field situations. A final slope is obtained in both cases at around 600 s, corresponding to a steady state. The fine sand erosion ends up with an adverse slope but also with a steeper slope than the coarse sand dike. Figure 2.8 (c) shows the dike level evolution for the cross-section located at the dike crest (x = 0.65 m) but similar conclusions can be drawn when studying other cross-sections of the dike.

For the first 15 s, the bed level increases. One hypothesis to explain this increase is that a mixture of water and sediment is flowing rather than clear water, and the exact bed elevation cannot be seen by the laser. This hypothesis is illustrated in Figure 2.9 where the mixture of sand and water is observed to flow downstream after 14 s of overtopping. Another hypothesis, although less probable, could be the influence of optical distortion due to the free surface, whose depth is more important in the first steps of overtopping. After 15 s, the dike is eroded with a

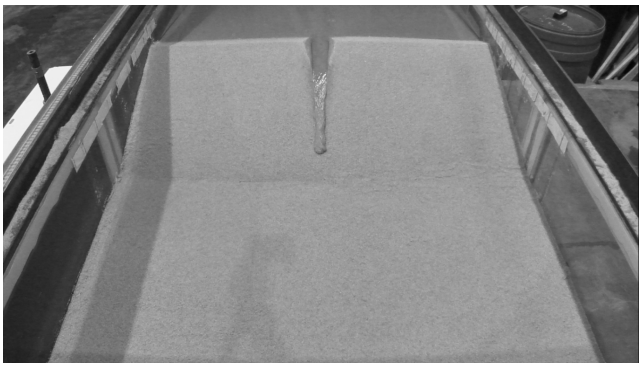


Figure 2.9: Mixture of fine sand and water flowing downstream after 14 s of flow.

decreasing erosion rate. The coarse sand dike is initially eroded faster than the fine one. However, the fine sand dike then catches up this delay and they both stabilize at the same level. Both dikes present similar behaviour to Visser (1998) observations when considering the widening of the breach, for different cross-sections (Figure 2.10). During stage I, the channel width at the crest does not change much, however a narrow channel is dug on the downstream slope. This channel widens slower in the case of the fine sand dike, due to a more cohesive behaviour than

the coarse sand one. Conversely, the vertical digging speed seems similar for both cases. Subsequently, in stage II and up to 120s, the breach and the downstream channel undergo progressive widening and deepening, until the eroded width of the breach aligns with that of the downstream channel.

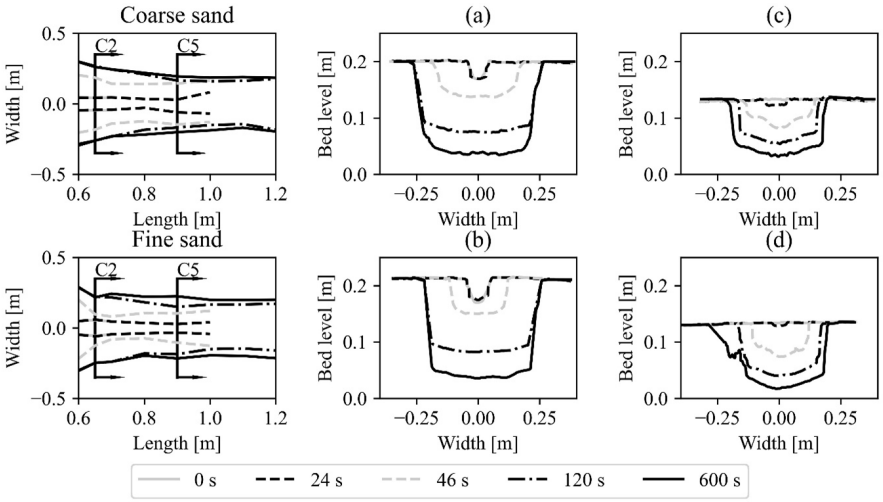


Figure 2.10: Evolution of the width of the breach (left) along time (experiments) and of two cross-sections: at the crest (x = 0.65 m, laser-sheet C2) with coarse sand (a) and with fine sand (b); and in the slope (x = 0.9m, laser-sheet C5) with coarse sand (c) and fine sand (d).

Finally, between 120 s and 600 s, corresponding to stage III, the geometry changes much more slowly before reaching an equilibrium or steady state. It is interesting to notice that, except for the section in the downstream slope at 600 s for the fine sand, all cross-sections are symmetrical, which attests the good conditions and the repeatability of the experiments. Globally, the coarse sand dike presents a smoother evolution than the fine sand dike. This can be explained by an apparent cohesion in the fine sand that creates a burst behaviour: small blocks of fine sand sliding together.

2.4.3 Evolution of the water level and discharge

As mentioned in the introduction, it is of core interest to predict the measured discharge across the breach. The discharge is directly related to the collapse of the dike. It can be deduced from the input discharge ($Q_{in} = 4ls^{-1}$) combined with the evolution of the water level in the reservoir. Indeed, the discharge Q through the breach corresponds to the evolution of the water level z_w in the reservoir multiplied by the horizontal surface A_r of the reservoir, i.e. $Q = Q_{in} - A_r \frac{dz_w}{dt}$. This estimation does not consider the seepage that was observed in the coarse case, that is assumed to be negligible compared to the ongoing overtopping process. Figure 2.11 illustrates the temporal evolution of (i) the water level captured by the ultrasonic probe G1 (Figure 1), and (ii) the temporal evolution of the discharge in the breach deduced from the measurements of the ultrasonic probe G1. The water level in the reservoir is expected to grow until the collapse occurs. The peak of water level occurs around 41 s (coarse sand) and 46.5 s (fine sand) with a maximum level measured at.0.199m (coarse sand) and 0.203m(fine sand). The difference between the two sands can be explained by seepage through the dike for the coarse sand, and by an easier initial erosion due to a lower apparent cohesion. Conversely, the final water level ends up being higher for coarse sand than for fine sand: the final slope of the collapsed dike is steeper for fine sand (as shown in the profiles at Figure 2.8), which explains that the final water level will be lower. This also reflects the fact that coarse sand requires higher shear stresses to be eroded, when cohesion effects do not play any strengthening effect any more, as it is the case at the end of

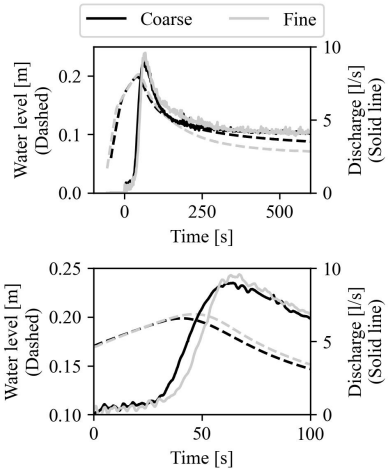


Figure 2.11: Evolution of the reservoir water level (from gauge G1, dashed line) and of the water discharge (solid line). The figure below is a zoom between 0 s and 100 s of the figure above.

the experiment. Accordingly, the water discharge is expected to evolve similarly to the water level. Indeed, the peak of water discharge is also delayed between coarse and fine sand. It occurs earlier for coarse sand (64 s) than for fine sand (67 s); their respective peak value is similar to the water level peak: less discharge for the coarse sand ($0.009\,\mathrm{m^3\,s^{-1}}$) than for the fine sand ($0.0096\,\mathrm{m^3\,s^{-1}}$). The delay between the highest water level and the highest discharge is approximately the same for both sand size, though (respectively 20.5 s and 23 s). After the peak, the slopes are very similar.

2.5 Numerical models

This section presents two numerical models: a simple unidimensional finite-volume model and a (more complex) bidimensional finite-volume model. Both models are based on the shallow water equations (describing water mass and momentum conservation) augmented with the Exner equations (for sediment mass conservation). The equations are solved using an explicit finite-volume numerical scheme $U_i^{n+1} = f(U_i^n, F^*)$, where the time is represented by the superscript n and the exchanges between volumes at the interfaces are represented by the fluxes F^*. After each temporal update, the bank stability conditions of the dike are verified. If the conditions are no more satisfied, a bank-failure operator is called to solve the collapse (Swartenbroekx et al., 2010). Then, a new time step can be run on a stabilized dike. The conserved values, the numerical schemes for fluxes estimation and the bank-failure operator will be explicitly defined for each model in the next subsections. Then, the models will be compared and validated against experimental data in Section 2.6.

2.5.1 One-Dimensional model

The one-dimensional model considered here was developed by Franzini and Soares-Frazao (2018), based on the two-dimensional model of Murillo and García-Navarro (2010) and including a concept of "energy balance" as defined in Murillo and Garcia-Navarro (2014) or in Franzini and Soares-Frazão (2016). In this model, the one-dimensional channel is divided into sections of small width. The flow is reduced to moving in only one

direction (the axis of the flume) and the values of interest are described as averaged values over the considered cross-section (Figure 2.12).

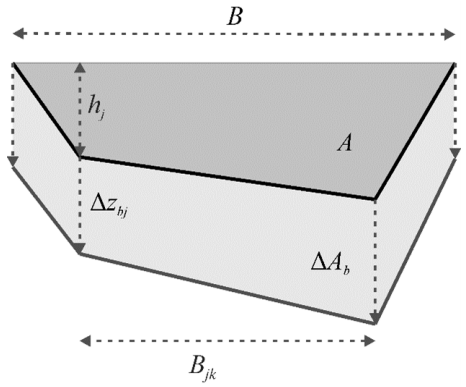


Figure 2.12: Discretization of channel as a one-dimensional cell. The dark grey area represents water, while the light grey area represents the eroded sediment.

These values of interest are the mass of water represented by the area of water A, the discharge Q, and the mass of sediments represented by the area A_b in the cross-section. These areas can evolve with time not only in depth but also in width, which permits the erosion of the dike to be captured. More specifically, the water mass evolution only depends on the mass exchange at the cell boundaries, just like the sediment transport. The closure equation required for the latter is the Meyer-Peter and Müller (1948) formula, for which the range of application is mostly the non-cohesive particles moving with not much of suspension. The sediments discharge Q_s is hence:

$$Q_s = 8B\sqrt{g(s-1)d_{50}^3}\left(\frac{RS_f}{(s-1)d_{50}} - \theta_{cr}\right)^{1.5} \tag{2.1}$$

where s is the specific gravity of the sediments, d_{50} is the bed sediment median diameter, R is the hydraulic radius (defined as $R = A/P$), and θ_{cr} is the shear stress for initial sediment motion (here the value is set at 0.047). The evolution of the discharge depends on hydrostatic pressure, the area of sediment evolution, the longitudinal component of lateral pressure (in case of expansion or constriction of the flume), and the friction slope. Together they define the exchange of momentum between adjacent cells that conduct the discharge evolution. Applying these

constraints to the shallow-water equations, the temporal dynamics of the conserved variables $U = [A, Q, A_b]^T$ can be simplified under the following equation in vector form:

$$\frac{\partial U}{\partial t} + \mathrm{H}\frac{\partial F}{\partial x} + \mathrm{H}\frac{\partial U}{\partial x} = S \tag{2.2}$$

where F groups the momentum fluxes and hydrostatic pressure contributions:

$$F = \begin{bmatrix} Q \\ \frac{Q^2}{A} + gI_1 \\ \frac{Q_s}{1-\varepsilon_0} \end{bmatrix} \tag{2.3}$$

where Q is the discharge, A is the area of water, gI_1 is the hydrostatic pressure, Q_s the sediment discharge and ϵ_0 the sediment's porosity. $\mathbf{H}\frac{\partial U}{\partial x}$ captures the impact of the morphological variation on the momentum, where $\mathbf{H}$ is the following matrix:

$$\mathrm{H} = \begin{bmatrix} 0 & 0 & 0 \\ 0 & 0 & \frac{gA}{B_s} \\ 0 & 0 & 0 \end{bmatrix} \tag{2.4}$$

B_s value is an equivalent average sediment width that links changes in bed level to changes in sediment area $\Delta z_b = \Delta A_b / B_s$. S are the source terms (lateral pressure and friction):

$$S = \begin{bmatrix} 0 \\ gI_2 - gAS_f \\ 0 \end{bmatrix} \tag{2.5}$$

For a rigorous definition of the matrices U, F, H and S, as well as a more complete explanation of the model, we refer the reader to Franzini and Soares-Frazao (2018). Equation 2.2 is numerically solved via a finite volume scheme applied to this 1D formulation over computational cells of length dx centred on each cross-section. Then the (temporal) explicit resolution scheme is given by:

$$U_i^{n+1} = U_i^n - \frac{\Delta t}{\Delta x}\left(F_{i+1/2}^{*L} - F_{i-1/2}^{*R}\right) \tag{2.6}$$

where the fluxes $F_{i+1/2}^{*L}$ and $F_{i-1/2}^{*R}$ are the lateralized contributions, respectively from the upstream and downstream sections calculated using

the augmented Roe scheme with energy balance (Franzini and Soares-Frazao, 2018). The source terms (topography and friction) are directly integrated to the fluxes yielding lateralized values (i.e. values that are different for the left and right cells, the difference being the result of the source term).

The area of erosion/deposition, A_b, is distributed along the section proportionally to the local water depth resulting in a non-uniform erosion of the cross-section. No erosion occurs if the water depth is equal to zero. The classical sediment transport theory links the shear stress at the bottom of the flow to the water depth. Therefore, linking the sediment transport to the water depth distribution along the section seems to be a reasonable assumption. Last but not least, a tilting bank failure operator is also included.

It is activated after each time step if the stability conditions are not satisfied anymore (with respect to the dry and wet critical friction angles given in Section 2.2). The general operation of the process is illustrated on Figure 2.13: section BC is initially steeper than the friction angle, therefore it is unstable and is tilted to its stability angle. Segment B'C'

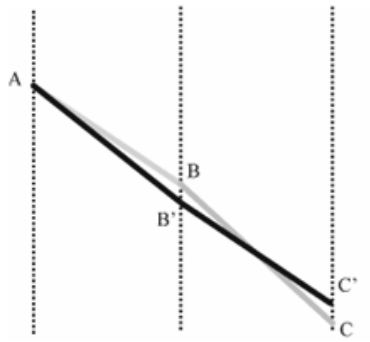


Figure 2.13: Bank failure operator (Franzini and Soares-Frazao, 2018). The segment BC is initially unstable. The level of point B is tilted down to B' so that the slope becomes stable. Stability of segment AB' is checked in the next operation.

is now stable, but segment AB' is now unstable and will be tilted in the next operation. Unlike in Franzini and Soares-Frazao (2018), the failure operator is here used both transversally and longitudinally to improve the capture of sediment mass failures that occur in both directions.

2.5.2 Two-Dimensional model

The 2D finite-volume model solves the shallow water and Exner equations on unstructured triangular meshes. The flow is now free to move in two directions (x-y) and the fluxes are evaluated using a modified LHLLC scheme (Soares-Frazão and Zech, 2011). Like in the unidimensional model, the sediment transports are also computed using the Meyer-Peter and Müller (1948) formula (Eq. 2.1). The conserved variables are now the water depth h, the discharge q_x in the direction of the flow and q_y in the flat perpendicular direction, and the sediments level z_b, i.e $\boldsymbol{U} = [h, q_x, q_y, z_b]^{\mathrm{T}}$. The temporal dynamics can be described in vector form as:

$$\frac{\partial \boldsymbol{U}}{\partial t} + \frac{\partial \boldsymbol{F}}{\partial x} + \frac{\partial \boldsymbol{G}}{\partial y} = \boldsymbol{S} \tag{2.7}$$

$$F = \begin{bmatrix} uh \\ u^2h + gh^2/2 \\ uvh \\ q_{sx}/\left(1 - e_0\right) \end{bmatrix} \tag{2.8}$$

$$G = \begin{bmatrix} vh \\ uvh \\ v^2h + gh^2/2 \\ q_{sy}/\left(1 - \varepsilon_0\right) \end{bmatrix} \tag{2.9}$$

$$S = \begin{bmatrix} 0 \\ gh\left(-\frac{\partial z_b}{\partial x} - S_{fx}\right) \\ gh\left(-\frac{\partial z_b}{\partial y} - S_{fy}\right) \\ 0 \end{bmatrix} \tag{2.10}$$

where vectors **F** and **G** group the momentum fluxes and hydrostatic pressure contributions and variation in the x-axis and y-axis directions respectively, also considering transverse fluxes; **S** are the source terms considering slope and friction effects; u is the velocity component along the x-axis; v the velocity component along the y-axis; z_b the bed level; q_{sx} the sediment transport along the x-axis; q_{sy} the sediment transport along the y-axis; S_{fx} and S_{fy} the friction slope along the x-axis and the y-axis, respectively. The finite-volume scheme to numerically solve is as

follows:

$$U_i^{n+1} = U_i^n - \frac{\Delta t}{\Omega_i} \sum_{j=1}^{3} \mathrm{R}_j^{-1} \overline{F^*} L_j + S_i \Delta t \tag{2.11}$$

where Ω_i is the cell area and L_j is the interface length; the fluxes at the interfaces $\overline{F^*}$ are represented considering normal and tangential directions obtained through the rotation matrix $\mathbf{R}$ to be expressed in a local coordinates system attached to the interface, and whose components are computed from the neighbouring cells using the LHLLC scheme (Soares-Frazão and Zech, 2011). When the local slope of a cell increases excessively, the failure of the bank is simulated by a bank-failure operator (Swartenbroekx et al., 2010) activated under the same conditions as in the unidimensional model and that ensures mass conservation. As the slope of a cell exceeds the considered angle of repose, the algorithm is used to distribute the slope of adjacent cells and check their proper balance. Execution of the Shallow-Water-Exner solver then resumes on the stabilized mesh, and the bank failure algorithm potentially restarts following detected instabilities. The time step is computed using the CFL condition, with the CFL number sets usually to 0.9. A minimum water depth is considered to avoid numerical instabilities in case of wet-dry transitions, and is set to 10^{-4} m.

2.6 Discussion of the numerical simulations and the experiments

In this section, the aforementioned models will be compared to experimental data. The 1D-mesh is composed of 363 cells, evenly distributed along the channel. The 2D-mesh is composed of approximately 200,000 elements with the smallest ones located at the crest of the dike with an average edge length of 2.5 mm. Such a refined mesh is needed to capture the widening of the breach better as it has a tremendous impact on the bank failure operator. The codes are developed in C++ and the 2D code is parallelized with OpenMP.

A substantial difference between the two models lies in the computational time and the computational resources needed to obtain a prediction. It is clear that running a 1D-model on hundreds of cells is faster and less time and energy consuming than running a 2D-model

on hundreds of thousands of cells. While the 1D model took less than an hour to simulate the failure, the 2D models took several days. This difference of computation time is balanced by the amount of data that we can retrieve from each model. While the 1D model is only able to provide information regarding the discharge and the area at a particular x-position, the 2D model can provide precise information regarding the (e.g.) velocities at very local scale, in the x-y directions.

Even if the erosion process is mostly active in the flow direction, taking the y-direction processes into account is an asset for the 2D model when evaluating the breach lateral evolution. The precise knowledge of the water depth, directly linked to the shear stress, in the full area is also of utmost importance when looking for an optimal design for a given dike. Considering these points, we expect the 2D model to perform better than the 1D model for predicting the dike breaching process. The state of the flow is captured at $t_0 = 0$ s, $t_1 = 46$ s, and $t_2 = 120$ s.

2.6.1 Comparison with the one-dimensional model

Figures 2.14- 2.15- 2.16 show the results obtained using the unidimensional model to simulate the dike breaching with fine and coarse sand. Figures are presented in similar way to Section 2.4 to ease the comparison by the reader: results in Figures 2.14 and 2.16 can confirm the theory of Visser (1998) and Coleman et al. (2002). For comparison purposes, Figure 2.16 illustrates the water level and discharge evolution over time. Once again, one can observe that the failure process can be divided into three parts: (i) the first 50 s (illustrated here by the results at 46 s), (ii) between 50 and 120 s (illustrated here by the results at 120 s), and (iii) between 120 s and 600 s. The 1D model is able to capture the widening and deepening of the breach during the first phase as observed in Figure 2.15 (the solid lines represent the results at 46 s). This phase ends approximately at the peak of the measured outflow discharge, that occurs after the peak water-level in the reservoir (Figure 2.16). During the second phase, after the maximum water level has been reached in the reservoir, erosion accelerates, resulting in an increase of the breached section and consequently a decrease in the water level in the reservoir as the inflow discharge is not sufficient any more to maintain the level constant (Figures 2.14 and 2.16). The erosion process computed in the 1D model is overestimated, leading to

an overestimation of the peak discharge and a lower water level in the reservoir. The computed erosion is such that it ends up reaching the fixed bottom of the channel. Consequently, the computed peak discharge at the breach is much higher than the experimental one because of the faster erosion of the breach, but ends up at almost the same rate. In contrast, the widening is well estimated even if the breach banks are steeper than the real ones. It can also be observed that the cross-sections present a triangular shape in the simulation but not in the experiment. This difference in shape is created by the bank failure operator: the tilting of the bank is so important that both banks meet in the middle of the breach. Later, the non-uniform erosion increases this triangular shape, as the erosion is higher in deeper water. To sum up, the unidimensional model fails at predicting the erosion of the dike in that it overestimates the peak outflow discharge and the erosion depth. However, the prediction of the widening of the breach is satisfying. We can therefore consider that one-dimensional model is useful when being used as first approach for the design of breach-induced floods.

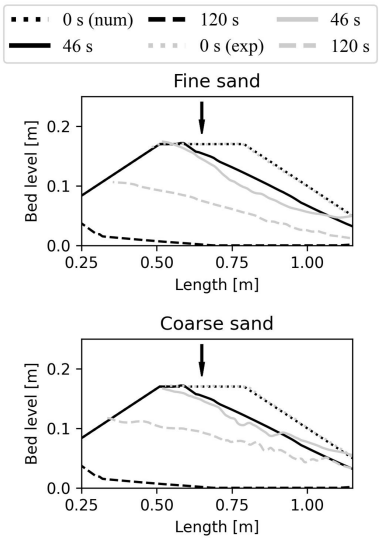


Figure 2.14: Evolution of the bed level along the centreline of the flume (1D model) for fine sand (above) and coarse sand (below). Over time, numerical results (black) differ more and more from experiments (grey) because the 1D model fails at predicting the digging of the flow.

2.6.2 Comparison with the two-dimensional model

Figures 2.17-2.18-2.19a show the results obtained using the two-dimensional simulation. Similarly to the one-dimensional case, the failure process can be divided into three parts corresponding to the stages previously described: (i) the first 50 s (illustrated here by the results at 46 s), (ii) between 50 and 120 s (illustrated here by the results at 120 s), and (iii)

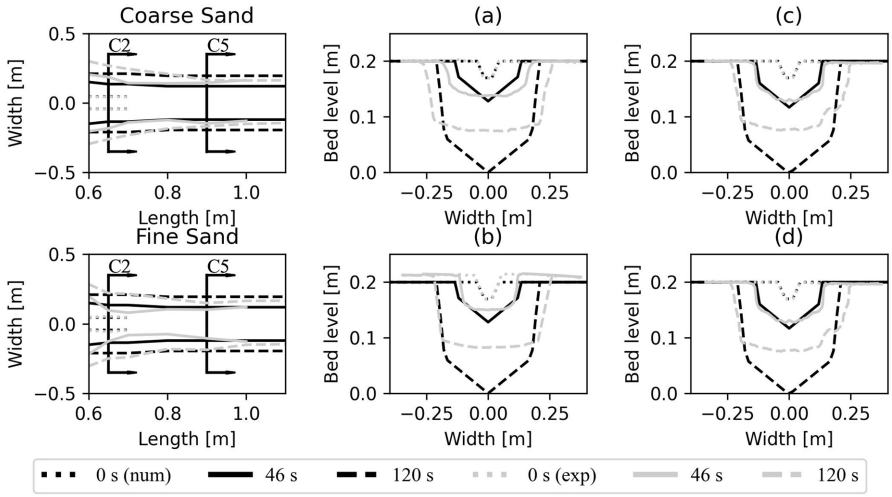


Figure 2.15: Evolution of the width of the breach (left) along time (1D model) and of two cross-sections: at the crest (x = 0.65 m, laser-sheet C2) with coarse sand (a) and with fine sand (b); and in the slope (x = 0.9m, laser-sheet C5) with coarse sand (c) and fine sand (d). The 1D predictive model (black) captures well the widening of the breach but fails at estimating its depth. Experimental results are presented in grey.

between 120 s and 600 s. This model gives a good prediction of the overall evolution of the breach. The evolution of the bottom profile is relatively close to what has been observed during the experiment.

In general, Visser (1998) prediction is well reproduced: during the first phase, the model estimates correctly the widening of the breach although the model yields less symmetrical results than the observed ones (Figure 2.17). This could be attributed to the bank failure operator that is activated every 50 time steps. Indeed, it was shown in Swartenbroekx et al. (2010) that a converged solution can be obtained with the bank failure operator, but at higher computational costs.
Therefore, the authors recommended to apply it for a limited number of iterations within each time step, yielding satisfactory but slightly less accurate results.
During the second phase, the breach widens more than in reality. However, the breach level evolution is correctly captured (Figure 2.18), as theorised by Coleman et al. (2002), and the model is able to predict the breach

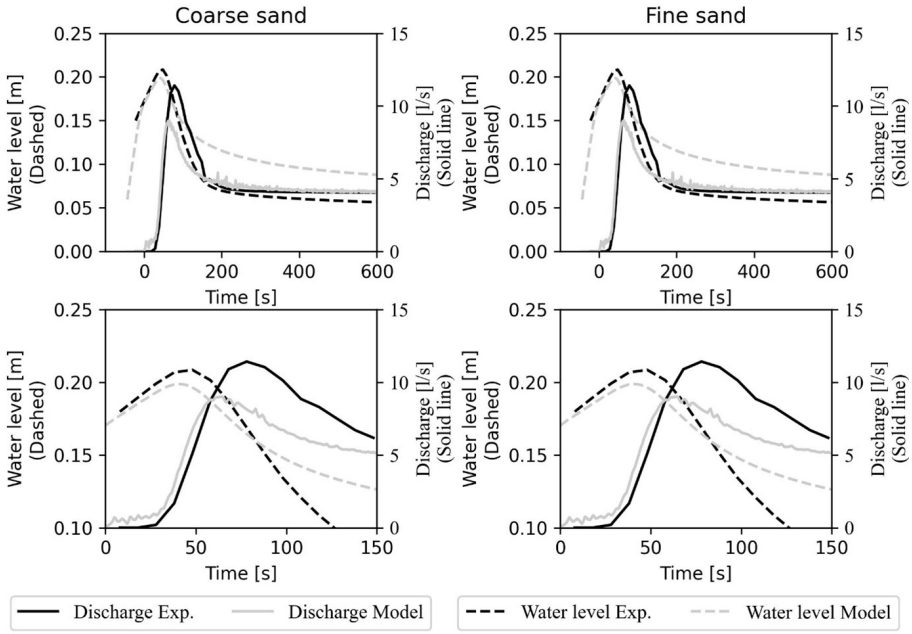


Figure 2.16: Evolution (1D model) of the water level in the reservoir (dashed lines) and discharge in the breach (solid lines) for coarse sand (left) and fine sand (right). The model (black) detects the peak correctly but fails at estimating its actual value (grey). The graphs below are a zoom of the graphs above.

shape with the local constriction. The discharge and reservoir water level are also well predicted (Figure 2.19a) despite a slight overestimation of the peak of discharge. This overestimation explains that the model widens the breach too fast.

Finally, Figure 2.19b compares the results obtained with 1D and 2D models. It can be observed that the 1D model is not able to capture the breach constriction. This is not surprising since no lateral forces are really applied on the banks, in the 1D model. This confirms the importance of the y-direction flow in the erosive process, as explained previously. However, the width at the crest (after 0.6m) is well predicted in both cases.

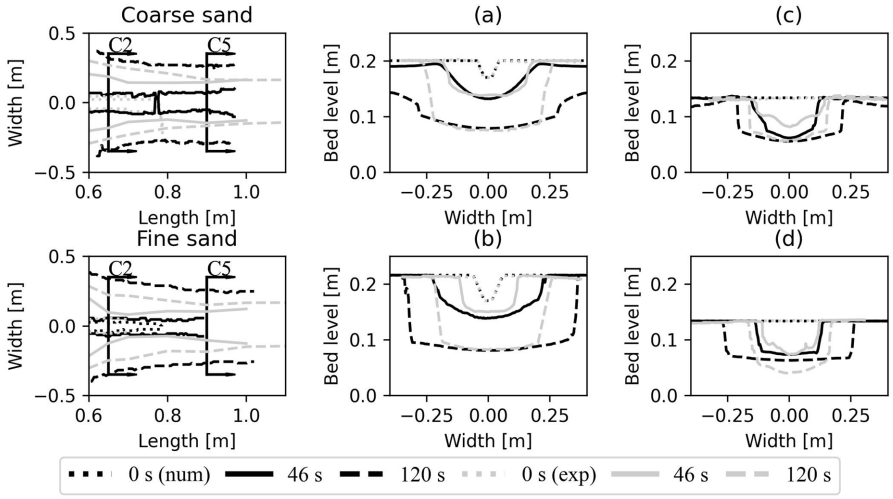


Figure 2.17: Evolution of the width of the breach (left) along time (2D model) and of two cross-section: at the crest (x = 0.65 m, lasersheet C2) with coarse sand (a) and with fine sand (b); and in the slope (x = 0.9m, laser-sheet C5) with coarse sand (c) and fine sand (d). The 2D predictive model (black) captures well the depth of the breach but fails at estimating its width, which is the opposite than the 1D model (Figure 2.15). Experimental results are presented in grey.

2.7 Conclusion

Small-scale experiments of dike breaching have been performed using fine and coarse grain sizes. The overall process demonstrated strong consistency with traditional observations found in the literature regarding the widening and deepening of breach in non-cohesive fill dikes (Coleman et al., 2002; Visser, 1998).

First, the fine sand showed an apparent cohesion leading to steep slopes, block mass failure and therefore irregular widening of the breach. Conversely, the width variation was much smoother for the coarse sand dike. Second, the fine sand dike failure exhibits a higher and later peak for both the water level in the upstream reservoir and the breach discharge.

It was also observed that the delay between the reservoir level peak and the peak discharge were similar for both sand sizes. Then, the experimental results have been compared to numerical simulations us-

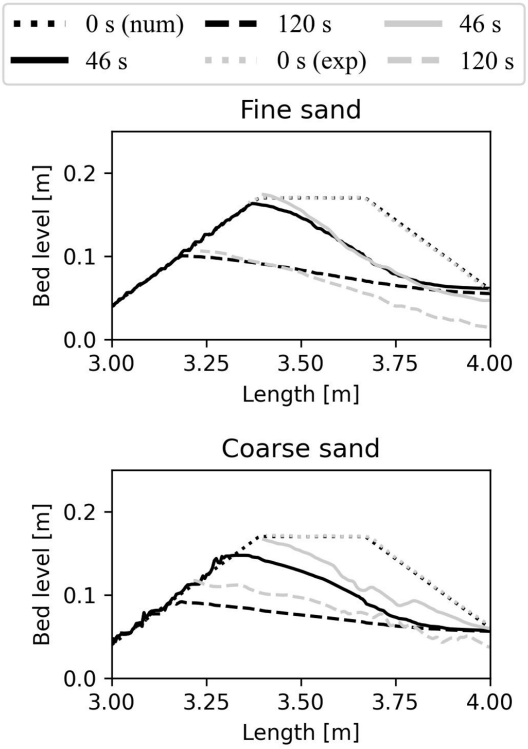
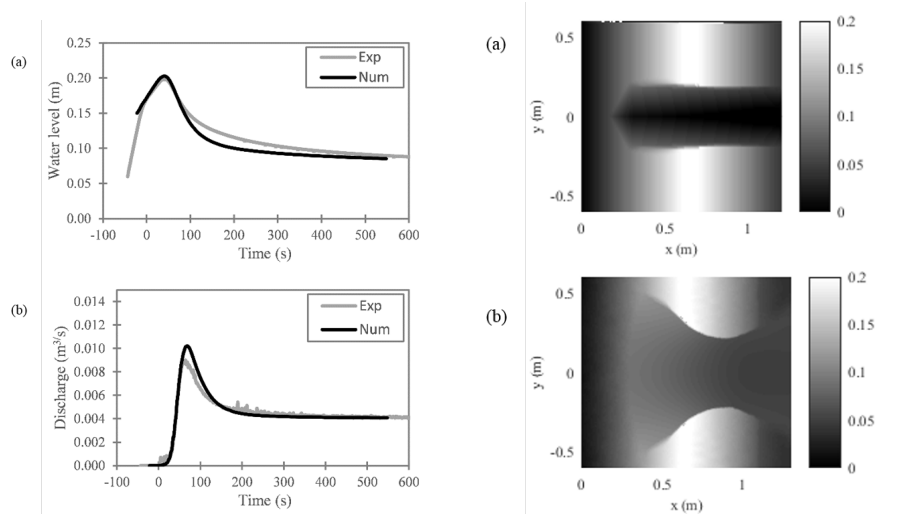


Figure 2.18: Evolution of the bed level along the centreline of the flume (2D model) for coarse sand (above) and fine sand (below). Compared to Figure 12, the numerical results (black) capture better the deepening of the sand level measured by experiments (grey).

ing 2D and 1D models. Despite its simplicity, the simple 1D model showed good results for the initial stage of the dike failure for all the monitored parameters even though the width evolution along the breach was straighter than the experiment. However, the results after the peak discharge were not as good, as the 1D model tends to overestimate the erosion rate.

Nevertheless, the width evolution along the breach was correctly estimated even if presenting bank slopes that were too straight. However, the model was not able to fully evaluate the evolution of the dike in all directions. The fact that the 1D model needs less computational cost and



(a) Evolution of (a) the water level in the reservoir and (b) the discharge in the breach for coarse sand as calculated using the 2D model.

(b) Comparison of the breach geometry after 120 s. The colour bar represents the bed level, for (a) the 1D model and (b) the 2D model.

Figure 2.19: (a) Evolution of the water level in the reservoir and discharge in the breach for coarse sand (2D model). (b) Comparison of the breach geometry after 120 s for the 1D and 2D models.

still provides interesting results for the breach width makes it very useful to determine a first order of magnitude for failure time and discharge in initial stages of design. For further work, it would be interesting to study other ways to distribute the erosion across a transversal section, see for instance Martínez-Aranda et al. (2019).

The 2D model showed good results in predicting the overall evolution of the bottom of the dike breach. Nevertheless, the widening of the breach, estimated with the bank failure operator, was overestimated. The model was more accurate than the 1D model in predicting the peak discharge and water level peak, which are ultimately the quantities of interest. The results presented here show the ability of the models to complement each other to get closer to reality. However, it should be kept in mind that these models, as well as most of the models in the literature, are limited to the evaluation of breaches in dikes made of non-cohesive materials.

In the future, efforts must be undertaken to develop numerical models capable of reproducing cohesive effects, due to water content or to the nature of the materials themselves, through a more sophisticated consideration of mechanics. The aim is to be able to assess the resistance to overtopping flows of real dikes, more often made of cohesive materials. The next chapter will therefore focus on the tracking of the suction evolution inside the dike during overtopping.

Key takeaways from this chapter

→ Small-scale experiment of non cohesive dike breaching are presented.

→ The experimental results are consistent with the literature.

→ 1D and 2D numerical models solving the shallow-water-Exner equations are presented.

→ Both numerical models are equipped with a bank failure operator intending to capture the instabilities of the dike's banks.

→ The 2D model performs better in reproducing the experiments than the 1D model but at a much higher computational cost.

→ The 2D model captures the evolution of the breach depth but struggles to estimate its widening.

→ The strength of the sediment-based approach is to provide straightforwardly the outflow hydrograph.

→ The model is limited to non-cohesive materials and does not account for the effects of suction on the mechanical strength.

CHAPTER 3

Coupled surface-subsurface flow modelling in earth dikes

This chapter is based on a paper published in the Journal of Hydraulic Research (Delpierre et al., 2023). As mentioned in the previous chapter, suction and the degree of saturation may explain some of the behaviours observed during the overtopping experiments, such as the apparent cohesion holding the breach sides steep. Tracking the evolution of the saturation degree and suction head *in the dike* appears to be a physical way to take suction into account in a comprehensive model. The suction head in the dike can vary significantly in space and time, following various weather conditions such as droughts and intense rainfall events. The resulting subsurface flow can affect the free-surface flow in case of overtopping. Conversely, the free-surface flow can modify the pore water content, which controls erosion and slope instabilities. A combined approach to such situations is presented, in which the degree of saturation and the flow through the embankment are simulated by solving the two-dimensional Richards equation on an unstructured mesh with an implicit finite volume scheme that is coupled to the system of shallow-water equations solved in one dimension using an explicit finite-volume scheme. The coupled model is validated on several situations of flows through

and over earthen embankments with different constitutive materials.

Contents

3.1 Context **64**
3.2 The Richards equation and flow in unsaturated porous media **66**
3.2.1 Experimental measurement of the soil water retention curve 70
3.3 Finite-volume resolution of the Richards equations **74**
3.3.1 Validation 76
3.4 Coupling between Richards and shallow water equations **79**
3.4.1 Spatial and temporal coupling 79
3.4.2 Source terms 81
3.5 Model validation **82**
3.5.1 Flow through an embankment 82
3.5.2 Flow through and over embankment: influence of initial water saturation level 84
3.5.3 Flow through and over embankment: influence of saturated hydraulic conductivity . . 86
3.6 Conclusion **87**

Symbol	Description	Units
S_e	degree of saturation (effective saturation)	–
θ	volumetric water content	– (m^3/m^3)
θ_s	saturated volumetric water content	–
θ_r	residual volumetric water content	–
h	pressure head (suction head)	m
K	hydraulic conductivity (unsaturated)	$m\,s^{-1}$
K_s	saturated hydraulic conductivity	$m\,s^{-1}$
C	hydraulic capacity ($\partial\theta/\partial h$)	m^{-1}
D	hydraulic diffusivity	$m^2\,s^{-1}$
α	Mualem-van Genuchten parameter	m^{-1}
η	Mualem-van Genuchten parameter	–
μ	Mualem-van Genuchten parameter	–
L	Mualem-van Genuchten parameter	–
h_e	air-entry pressure	m
z	vertical coordinate (positive upward)	m
H	total hydraulic head ($H = h + z$)	m
t	time	s
Ω_i	computational cell area	m^2
$L_{i,j}$	interface (edge) length between cell i and j	m
$d_{i,j}$	distance between centres of adjacent cells i, j	m

A note on the terminology and sign convention:
In this chapter, the soil science terminology is used to describe the flow through unsaturated soils. This means that 'suction head' and 'pressure head' (denoted h) are used, with the units in metres (m). This is different to the geomechanics terminology, where suction is expressed in Pa and is positive for unsaturated soils. The sign convention is that a negative suction head corresponds to a positive suction (i.e. the soil is unsaturated), while a positive suction head corresponds to a negative suction (i.e. the soil is saturated).

3.1 Context

Flow through the dike can lead to internal erosion, but also modifies the water saturation level inside the embankment, affecting the breaching initiation and the pace towards complete failure during overtopping. This internal flow is highly dependent on the initial saturation of the dike material, whose effects on the failure have been largely overlooked so far. However, at full saturation, cohesion of the dike material is expected to greatly reduce, and thus the dike strength. To avoid such situations, drains are often placed in the dike at its downstream part to control the saturation profile by lowering the level of the water table in the dike and therefore increasing the time required for the full saturation. A better understanding of the combination of the initial dike saturation with the overtopping flow and the internal flow will fill a knowledge gap with the ambition to provide a physically based model that can be used to reduce the risks associated with these phenomena.

Many numerical models have been developed to design or assess the risk of failure of existing embankments when they are subject to overtopping or internal flows. Most of these models allow to consider only the overtopping flow, by solving the shallow water equations (Shao et al., 2006; Shiach et al., 2004; Van Emelen et al., 2016), as presented in the past chapter, or the internal flow inside the pores of the embankment by solving the Richards equation (Tsai et al., 2008; Chávez-Negrete et al., 2018).

For the Richards equation, in most cases, the numerical resolution is performed either by finite elements, finite volumes or finite differences, implying different types of spatial discretization (Farthing and Ogden, 2017), using generally structured meshes. From the temporal point of view, most models use an implicit time discretization (Farthing and Ogden, 2017), because of the inability of the explicit formulations to solve the problem when the soil is saturated (Caviedes-Voullième et al., 2013). Coupled models considering the interaction between subsurface and surface water flows exist in the literature but they are mostly used to understand the processes of irrigation or watershed replenishment (Furman, 2008; Weill et al., 2009).

Moreover, these models often overlook how suction affects geomechanical stability. While they focus on variables such as water content

and suction head, they typically neglect the implications of suction for apparent cohesion and stress state which are essential to embankment stability assessment. These effects will be explored in depth in the next chapter.

Therefore, coupled models are still not widespread in the engineering community for solving practical field cases, and decoupled models are often preferred where the focus is set on one of the models, i.e. overtopping flow or infiltration, while the second one is solved with empirical parameters or functions (Furman, 2008). Solving the coupled problem accurately in a comprehensive way poses several challenges, including changing boundary conditions as the soil can be submerged or not and these conditions may change over time, resulting in possible mass conservation errors linked to the numerical schemes used. Different numerical methods have been proposed to address these challenges and simulate hydrostatic surface-subsurface flows.

Casulli (2017) presented a method that uses a vertically integrated continuity equation, which is based on the principles of the Richards and Navier-Stokes equations on an orthogonal unstructured grid. An algorithm based on the Darcy law was used to solve flow in the saturated case considering purely hydrostatic flow. Similarly, De Maet and Hanert (2011) proposed an explicit solver for the Richards equation in the unsaturated zone, but used a method called the "false transient method" to handle the case when soil becomes saturated because of the explicit solver being unable to handle the saturated case. Additionally, Caviedes-Voullième et al. (2012) presented an algorithm that employs a non-iterative external coupling algorithm, using the 2D shallow-water equation for surface flows and the 3D Richards equation for subsurface flows on structured meshes. Finally, Mizutani et al. (2013) proposed a coupled solver that was used to study the influence of soil saturation on a dike's overtopping flow using a bi-dimensional structured mesh.

The aim of this chapter is to present a coupled finite-volume numerical model of both flows over and through earthen dikes using bi-dimensional unstructured meshes for the subsurface flow and ensuring mass conservation, featuring a robust coupling between the two types of flows. By using unstructured meshes, the model provides a flexible and adaptable framework for analysing complex geometries of earthen dikes.

The model's emphasis on pore analysis is of particular significance in

the context of dikes. Pore pressure, which refers to the pressure exerted by water within the void spaces of soil, plays a critical role in the stability and integrity of earthen dikes. By accurately capturing and analysing pore pressure distribution, the model provides valuable insights into potential weak zones, seepage patterns, and areas prone to failure. This information is essential for designing and maintaining robust dikes that can withstand hydraulic pressures and mitigate the risk of catastrophic failures when subject to extreme weather events as expected to happen in the coming future.

This chapter is structured as follows. First, the Richards equation and flow in unsaturated porous media are presented in Section 3.2. Section 3.3 details the numerical resolution of the Richards equation based on a finite-volume scheme on unstructured meshes. Section 3.4 describes the coupling between the subsurface flow, solved with the Richards equation, and the surface flow, evaluated with the shallow-water equations. Finally, Section 3.5 presents the validation of the coupled model and its application to dikes (considering a 2D cross-section) to highlight possible outcomes obtained with the presented scheme.

3.2 The Richards equation and flow in unsaturated porous media

The Richards equation (Richards, 1931) is a nonlinear partial differential equation describing the transfer of water in unsaturated soils under non-permanent conditions [1]. This equation is a simplified representation of a two-phase flow problem. Indeed, both water and air circulate into the porous matrix. Although it is possible to derive the Richards equation from the Navier-Stokes equations, the complexity of the granular matrix led Richards to simplify the problem by adopting a more macroscopic point of view based on experiments.

It is based on the combination of the continuity equation and the Darcy equation. Let Ω be the bidimensional domain, $\partial\Omega$ its boundary and $\mathbf{n}$ the normal vector at the boundary pointing outwards.

[1] Unfortunately for him, Richardson (1922) was in fact the first to present this equation but the name of Richards remains for posterity.

The Richards's equation can be written, in its mixed form, as:

$$\frac{\partial \theta}{\partial t} - \nabla \cdot [K(h)\nabla(h+z)] = 0 \quad \text{in } \Omega \times (0,T) \tag{3.1}$$

subject to the boundary conditions:

$$h = h_D \qquad \text{on } \partial\Omega_D \times (0,T) \tag{3.2}$$

$$-K(h)\nabla(h+z)\cdot \mathbf{n} = q_N \qquad \text{on } \partial\Omega_N \times (0,T) \tag{3.3}$$

where $\partial\Omega_D \cup \partial\Omega_N = \partial\Omega$ and $\partial\Omega_D \cap \partial\Omega_N = \emptyset$, with initial condition:

$$h(x,0) = h_0(x) \quad \text{in } \Omega \tag{3.4}$$

where θ is the volumetric water content which is a function of $h(\mathbf{x},t)$, the pressure head, and $K(h)$ the hydraulic conductivity.

One of the main difficulties of the Richards equation lies in its nonlinearity caused by the relationships between the volumetric water content, the pressure head and the hydraulic conductivity. Multiple models exist in order to describe the relations between those variables, the most frequent one is the Mualem-van Genuchten model (Mualem, 1976; van Genuchten, 1980), used in this work. It was developed in order to facilitate the representation of the so-called soil water retention curve (SWRC) that links volumetric water content and pressure head.

The development of this model follows the difficulty of determining the hydraulic conductivity in the case of unsaturated soils. While the experimental determination of the hydraulic conductivity is relatively simple in the case of a saturated soil, the hydraulic conductivity in an unsaturated soil is more difficult to determine because of its dependency on many factors. Moreover, its extensive measurement is expensive and time consuming as it usually requires the use of different methodologies to determine its evolution for various ranges of pressure.

The various formulations of the Richards equation

In this work, the Richards equation is expressed in its mixed form (Equation 3.1), where the unknown is the pressure head h. Nevertheless, the Richards equation can be expressed in several forms, which are worth mentioning:

1. **Mixed form** (unknown: pressure head h):

$$\frac{\partial \theta}{\partial t} - \nabla \cdot [K(h)\nabla(h+z)] = 0 \tag{3.5}$$

2. **Head-based form** (unknown: pressure head h):

$$C(h)\frac{\partial h}{\partial t} = \nabla \cdot [K(h)\nabla(h+z)] \tag{3.6}$$

   where $C(h)$ is called the hydraulic capacity [1/m].

3. **Water content-based form** (unknown: θ): This form, expressed in term of conserved variable, can not be employed in case of fully saturated soils.

$$\frac{\partial \theta}{\partial t} = \nabla \cdot [D(\theta)\nabla\theta] + \nabla \cdot K(\theta) \tag{3.7}$$

   where $D(\theta)$ is the diffusivity $[m^2/s]$:

$$D(\theta) = \frac{K(\theta)}{C(\theta)} \tag{3.8}$$

The Mualem-van Genuchten model used in this work describes the transitioning between the unsaturated and the saturated state of the soil with the following relationships:

$$\theta = \begin{cases} \frac{\theta_s - \theta_r}{(1+(\alpha|h|)^\eta)^\mu} + \theta_r & \text{if } h \leq 0 \\ \theta_s & \text{if } h > 0 \end{cases} \tag{3.9}$$

$$S_e = \frac{\theta - \theta_r}{\theta_s - \theta_r} \tag{3.10}$$

$$K = \begin{cases} K_s S_e^L \left[1 - \left(1 - S_e^{1/\mu}\right)^\mu\right]^2 & \text{if } h \leq 0 \\ K_s & \text{if } h > 0 \end{cases} \tag{3.11}$$

$$C = \begin{cases} -\mu\eta\alpha^\eta \frac{\theta_s - \theta_r}{(1+\alpha^\eta|h|^\eta)^{\mu+1}} |h|^\eta h^{-1} & \text{if } h \leq 0 \\ 0 & \text{if } h > 0 \end{cases} \tag{3.12}$$

$$\mu = 1 - \frac{1}{\eta} \tag{3.13}$$

where θ_s is the saturated volumetric water content, θ_r the residual volumetric water content, S_e the equivalent volumetric water content, K_s the saturated hydraulic conductivity and C the hydraulic capacity which represents the volumetric water content variation due to a head pressure variation ($\partial\theta/\partial h$). The other parameters in these equations need to be calibrated using laboratory measurements.

Still, some of those have a physical meaning and can be obtained using closure relations. For example, η is linked to the pore size distribution and describes the slope of the SWRC (Mualem, 1976). Some authors (e.g. Caviedes-Voullième et al. (2013); Soltani et al. (2021)) suggest that the α parameter is related to the air-entry pressure h_e. This pressure is defined by Brooks and Corey (1964) as the pressure state where the entry of air (and thus the evacuation of water) into the largest pore becomes possible during the desaturation process of a saturated soil (Figure 3.1). This pressure can be found graphically by crossing the horizontal asymptote at $\theta = \theta_s$ with the tangent to the SWRC in the transient part (Benson et al.). Soltani et al. (2021) highlight the fact that an incorrect evaluation of this parameter leads to a very poor evaluation of assessment of the water content, which is directly related to the relative permeability of the soil but also to its weight and shear

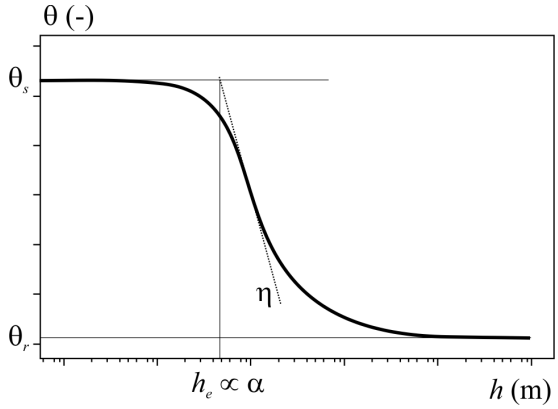


Figure 3.1: Schematic representation of the soil water retention curve.

strength. Following Mualem (1976), the parameter L is often considered as a tuning parameter, equal to 0.5, and this assumption is made in this work. The validity of this assumption is discussed by Shinomiya et al. (2001), where significant experimental evidence are presented, showing that this parameter should be fitted for each soil type. The physical interpretation of this parameter is related to the tortuosity and the connectivity of the pore network (Weynants et al., 2009; Dettmann et al., 2014). Figure 3.2 shows the effect of this parameter on the unsaturated hydraulic conductivity. It shows that, at constant suction head, a higher value of L leads to a lower hydraulic conductivity.

It is worth noting that soil hydraulic properties typically exhibit hysteretic behaviour, which is well documented in the literature (Kool and Parker, 1987; Likos et al., 2014). This behaviour is characterized by the existence of two distinct paths in the SWRC: one corresponding to the drying process and another to the wetting process. At the same suction head, the volumetric water content is higher during drying than during wetting. In this work, hysteretic behaviour is neglected, and the drying path of the SWRC is used for both wetting and drying processes.

3.2.1 Experimental measurement of the soil water retention curve

The fitting of the Mualem-van Genuchten model (especially $K(h)$ and $\theta(h)$) with experimental data is essential to obtain realistic numerical

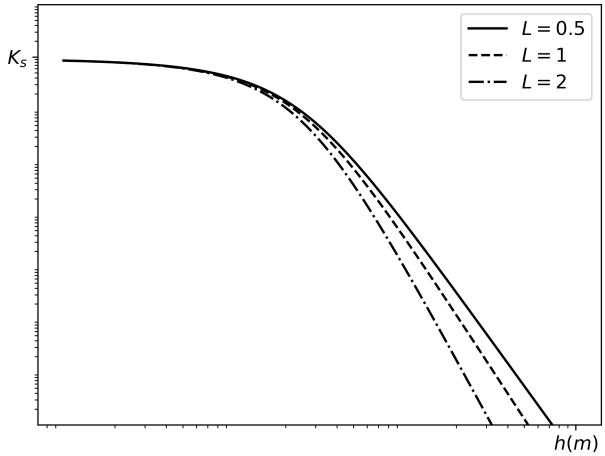


Figure 3.2: Schematic representation of the unsaturated hydraulic conductivity $K(h)$ showing the effect of parameter L.

results. The Earth and Life Institute of UCLouvain possesses an evaporation method apparatus called Hyprop, depicted at Figure 3.3, developed by METER Group. This method employs simple evaporative principles described in Schindler et al. (2010). To perform this test, a 250 cm^3 sample is carefully saturated from the bottom to avoid the formation of air bubbles, which can occur when saturating from the top.

The samples are then installed on the Hyprop measurement apparatus, as depicted at Figure 3.4, which measures the pore pressure changes as a function of the weight losses, directly related to the changes in volumetric water content. Two ceramic pore pressure sensors are used for this measure. The size of both sensors is not the same, allowing to measure the suction at two different depths of the sample. The unsaturated hydraulic conductivity is measured based on the Darcy-Buckingham law (Schindler et al., 2010). The assumption of a steady state is made, whereby the fluxes and hydraulic gradient are considered to be constant between each measurement step. Moreover, water content is assumed to decrease linearly between the two sensors. Schindler et al. (2010) shows that these assumptions provide satisfactory results



Figure 3.3: Exploded view of the Hyprop device retrieved from the METER Group website (Meter Group). The two ceramic pore pressure sensors are visible in the middle.

for sands, silts and clays by comparing the experimental results with inverse modelling. A limitation of the Hyprop method is underlined by Bezerra-Coelho et al. (2018). The authors show that Hyprop fails to estimate the hydraulic conductivity for soils presenting high η parameter values, i.e. soils with a steep slope of the SWRC, which is often the case for coarse medium. In this case, the K_s parameter should be measured independently and fixed in the fitting procedure. The measured values are then fed directly into the Hyprop-Fit software, which provides the least squares estimate of the soil water retention curve and unsaturated hydraulic conductivity parameters based on the Mualem-van Genuchten model. The suction measurement of the Hyprop device ranges between 0 and 100 kPa of suction. While this range of value can be sufficient for sand or coarse silt, it is not enough to fully caracterize the SWRC of finer soils such as clays.

To complement this measure, the WP4C device from METER Group can be employed to measure the suction up to 300 MPa. The measure obtained with this device is obtained on a very small sample of maximum 7 ml. The WP4C measures water potential by cooling a mirror until dew



Figure 3.4: A view of a Hyprop measurement in progress in the laboratory of the Earth and Life Institute of UCLouvain.

forms, then using the dew point and sample temperatures to calculate the moisture level in the sample. Combining the results from both devices, the complete SWRC is obtained.

An additional measurement of the saturated hydraulic conductivity allows to improve the accuracy of the hydraulic conductivity curve. The KSat apparatus also produced by METER group can be used for this purpose. It measures automatically the saturated hydraulic conductivity of the soil using a falling head method.

Based on the measurement of these three devices, a complete characterization of the soil hydraulic properties can be obtained. Hyprop is used to determine θ_s, α, η and L; WP4C to confirm the value of θ_r at high suction, and KSat to measure K_s.

3.3 Finite-volume resolution of the Richards equations

An implicit Eulerian solver is employed in this work. The primary reason behind employing implicit time integration solvers is that the Richards equation, as explained in Caviedes-Voullième et al. (2013), cannot be effectively solved using an explicit scheme in the saturated zone. The development of a solver with an explicit scheme necessitates the value of the suction head to be estimated knowing the volumetric water content using the Mualem-van Genuchten relationship. However, it becomes inherently impossible to differentiate between two suction heads solely based on the information that the soil is saturated.

By using an implicit time integration scheme, it becomes possible to directly express the scheme in terms of suction head. This allows differentiation between two suction heads for a saturated soil. Therefore, a system of equations is solved until convergence for each time step:

$$\mathbf{A_{i,j}} h_j^{n+1,m+1} = c_i \tag{3.14}$$

where $\mathbf{A}$ is a square matrix of N by N mesh elements containing terms calculated with the spatial and temporal integrations at time $n+1$, but at iteration step m; $\boldsymbol{h}$ is the vector of unknowns suction heads at time $n+1$ and iteration $m+1$, and $\boldsymbol{c}$ the vector of external source terms.

The terms detailed in Eqs 3.15 are obtained by applying the divergence theorem, consisting of applying the local mass conservation property to Eq. 3.1 (Mathematical approach and discussion of such schemes can be found in Bertolazzi and Manzini (2007)) and by linearizing the conductivity $K(h)$ and the capacity $C(h)$ using Picard iteration. This means that these terms are evaluated at time step $n+1$ but at iteration step m. The convergence of the system is achieved as soon as the maximum variation of suction head between two successive iterations is below a given threshold: $h^{n+1,m+1} - h^{n+1,m} < \epsilon$. The use of Picard iterations instead of Newton is a common discussion when numerically studying the Richards equation. Picard scheme is often presented as robust, with a simple and straightforward implementation ensuring a linear convergence, while Newton scheme is more complex but converges quadratically (Paniconi and Putti, 1994; Caviedes-Voullième et al., 2013).

$$\begin{aligned}
\mathbf{A}_{i,\mathrm{i}} &= \frac{C_i^{n+1,m}}{\Delta t}\Omega_i + \sum_k K_{i,k}^{n+1,m} L_{i,k} d_{i,k}^{-1} \\
\mathbf{A}_{i,\mathrm{j}} &= -K_{i,j}^{n+1,m} L_{i,j} d_{i,j}^{-1} \\
\mathbf{c}_i &= \sum_k K_{i,k}^{n+1,m} L_{i,k} \left(n_z\right)_{i,k} + \frac{\Omega_i}{\Delta t}\left(\theta_i^{n,m} - \theta_i^{n+1,m} + C_i^{n+1,m} h_i^{n+1,m}\right)
\end{aligned} \tag{3.15}$$

Other terms than those presented previously include: Δt the time step, Ω_i the area of the computational cell, $K_{i,j}$ the hydraulic conductivity at the interface between two cells computed as an arithmetic mean, $L_{i,j}$ the length of the edge and $d_{i,j}$ the distance between the centres of the two adjacent cells, $(n_z)_{i,j}$ the outgoing z-axis pointing normal to the interface between two computational cells (Figure 3.5).

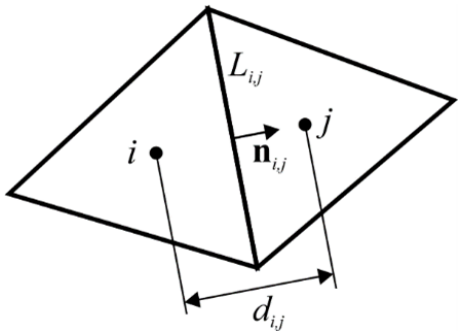


Figure 3.5: Finite volume discretisation of the Richards equation.

The numerical resolution of the Richards equation poses several challenges. Farthing and Ogden (2017) report the current state-of the art of the numerical methods used to solve the Richards equation and the challenges associated with it. Difficulties in achieving convergence are often caused by nonlinear constitutive relationships or very sharp wetting fronts, especially in dry soils, resulting in steep local gradients.

The mixed formulation of the Richards equation is often preferred to avoid mass balance issues inherent to the pure head-based formulation (Celia et al., 1990; Farthing and Ogden, 2017). In finite volume methods, conservation can be enforced in an integral sense using test functions that are constant over a control volume (Farthing and Ogden, 2017).

The time step is also critical. Using a large time step for a fast varying situation can lead to convergence issues. Caviedes-Voullième et al. (2013) report that no cases of instability were found when using their implicit solver to solve the mixed form of the Richards equation. Yet they underline that high non-linearity of the conductivity function can reduce the efficiency of the solver.

3.3.1 Validation

Two classical benchmarks are used for the validation of the Richards equation solver, consisting in flows through a column of unsaturated soil: first the drainage of a soil column, and then the propagation of a sharp infiltration front. The soil characteristics used for both tests are presented in Table 3.1. These benchmarks are chosen because of their wide use in the literature.

Analytical solutions might also be employed for the validation of Richards solvers. These soil data were presented first in a work by Celia et al. (1990) and the soil samples were collected in New Mexico. Since then, these soil data have been used in several studies to validate various Richards solvers (Caviedes-Voullième et al., 2013; Kavetski et al., 2001; Su et al., 2022).

Parameter	Value	Unit	Parameter	Value	Unit
K_s	0.00922	$\mathrm{cm\,s^{-1}}$	α	0.0335	$\mathrm{cm^{-1}}$
θ_r	0.102	–	η	2	–
θ_s	0.368	–	L	0.5	–

Table 3.1: Soil parameters used for the validation benchmarks.

Drainage of soil column

Caviedes-Voullième et al. (2013) proposed an idealized academic test case for their one-dimensional solver. It consists of a nearly saturated 1m high soil column with the parameters presented in Table 3.1.

The initial suction head is $h = -20$cm, meaning that the initial volumetric water content is $\theta = 0.323$. As the solver is bi-dimensional, the calculation was made on a 1m depth and 0.5m width plane. The average size for the mesh triangles was 1cm length edges, the integration

time step is set at 10s, while a constant numerical threshold of 0.001cm is employed for convergence.

The objective is to validate the solver by checking the mass conservation as well as the ability of the solver to converge to a hydrostatic equilibrium. The waterflow is simply driven by gravity and the boundaries are waterproof, meaning that no water can flow out of the system. The present solver provides convincing results as shown in Figure 3.6, no water enters or flows out of the system and a perfect hydrostatic equilibrium is obtained.

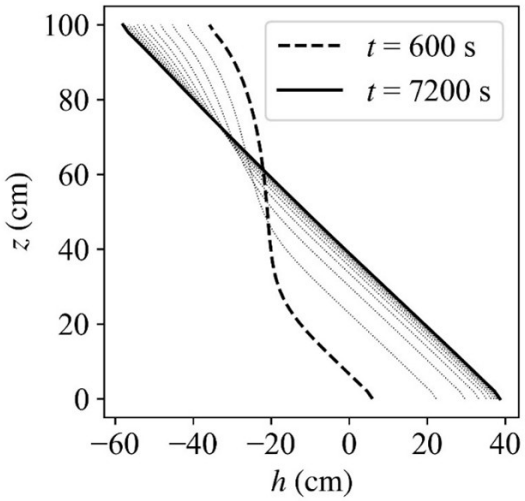


Figure 3.6: Suction head evolution in the drainage column test case. The final state is a hydrostatic equilibrium.

A sharp infiltration front

In this test case, a sharp infiltration front is generated in a soil column by both the initial and the boundary conditions. The initial conditions are described by the following function, where values are expressed in cm:

$$h(x,y,z,t=0) = \begin{cases} -1000 & \text{if } z > 0.6 \\ -75 - \frac{925}{0.6} z & \text{if } \quad 0 \leq z \leq 0.6 \end{cases} \tag{3.16}$$

where the z axis is pointing towards the bottom of the column. At the top of the column ($z = 0$cm), $h = -75$cm, as at the bottom of the column ($z = 60$cm) a constant suction head of $h = 1000$cm is imposed. These results have been used and compared as a benchmark in several articles (Horgue et al., 2015; Kavetski et al., 2001; Su et al., 2022). Results obtained by Horgue et al. (2015) are used as a reference solution and plotted in dashed lines to compare with the proposed solver. The results obtained with the present method match satisfactorily the reference ones (Figure 3.7). In this case, the calculation was made on a 0.6m depth

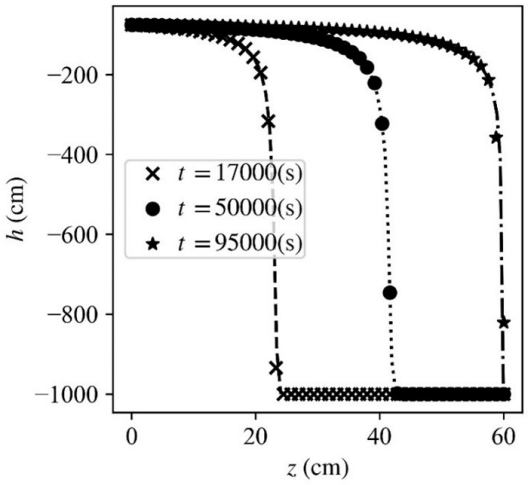


Figure 3.7: Results of test case 2: sharp infiltration front. Dashed lines represent the results by Horgue et al. (2015)

and 0.25m width plane. To accurately capture the gradient, triangular elements with edges measuring 0.2cm in length were used at the top of the soil column, while triangular elements with edges measuring 1cm in length were employed at the bottom. The integration time step was set at 60s, and a constant numerical threshold of 0.001cm was applied to ensure convergence.

3.4 Coupling between Richards and shallow water equations

3.4.1 Spatial and temporal coupling

The description of the surface flow is performed using the shallow water equations. Contrarywise to the previous chapter, the sediment transport is not accounted for here. Considering a unit-width system, the equations can be written as:

$$\begin{aligned} \frac{\partial h}{\partial t} + \frac{\partial q}{\partial x} &= q_{in} \\ \frac{\partial q}{\partial t} + \frac{\partial}{\partial x}\left(\frac{q^2}{h} + \frac{1}{2}gh^2\right) &= gh(S_0 - S_f) \end{aligned} \tag{3.17}$$

where h is the water depth, $q = uh$ the unit discharge with u the depth-averaged velocity, S_0 the bed slope and S_f the friction slope calculated using Manning's friction formulation.

Equations 3.17 are solved using an explicit finite volume scheme with the fluxes at the interfaces evaluated using Roe's scheme (Soares-Frazão and Zech, 2002).

Spatial coupling between the Richards and shallow-water equations is achieved at the interface between the two systems, i.e. the embankment surface, using appropriate boundary conditions.

Although on site the interface between the subsurface environment and the surface flow domain is not so well defined (silt, sediments, etc.), it is generally considered that this interface is sharp to facilitate the mathematical approach (Furman, 2008). In the present model, as illustrated in Figure 3.8, the subsurface and the surface cells are perfectly aligned. In this way no interpolation or remapping is required to obtain the boundary information, which avoids error propagation. Depending on the problem to be solved, different choices can be made. For example, a finer mesh can be used for the Richards equation to solve a sharp infiltration front (e.g. in the case of dry soil subjected to flooding), with a coarser mesh used for the shallow-water equations. In this case, careful design of interpolation techniques would be required to avoid propagating error.

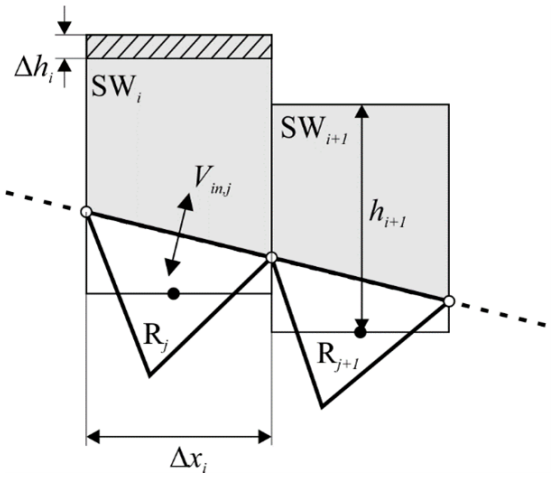


Figure 3.8: Schematic representation of the mass exchanged between the shallow-water equation cells (SW) and the Richards equation cells (R).

The algorithm consists in using the water depth of the surface flow as the boundary condition for the Richards' equation and using the calculated internal flows as source terms q_{in} in the mass conservation in Equation 3.17.

From a temporal point of view, the resolution method is staggered in the sense that the resolution of the shallow-water equations requires small time steps due to the explicit nature of the resolution scheme, whereas the implicit resolution of the Richards' equation allows the use of large time steps and still converge to a solution.

Let us define t_1 as the most recent time at which the Richards' equation was solved, $\Delta t_{\text{Richards}}$ as the Richards' equation time step, and Δt_{SW} as the shallow-water equations time step. The global simulation time, denoted as t, is updated by adding Δt_{SW} until it reaches $t = t_1 + \Delta t_{\text{Richards}}$.

At this juncture, the Richards' equation is solved, the source terms are evaluated, and the same process resumes until the final simulation time is reached. Therefore, a careful selection of the Richards' equation time step must be made. The selection of this time step is related to the nature of the soil and of the modelled conditions. For example, large time steps are usually more acceptable for low-conductivity soils. Opting for an excessively large time step may lead to inaccurate evaluation of

information corresponding to surface flow and source terms. Selecting an overly small time step significantly extends the computational time required.

Generally speaking, the selection of the appropriate time step is highly problem-dependent. In cases involving soils with high hydraulic conductivities, it is advisable to use smaller time steps due to the rapid occurrence of significant changes.

Conversely, situations involving soils with low conductivities can be solved with larger time steps, as transfers of water take place at a slower pace. In addition, since the flow through the soil is much slower than the free-surface flow, no information is lost with this decoupling.

3.4.2 Source terms

Considering an unit-width dike, the mass-balance over the discretized system of Figure 3.8 is formally established as follows for the source term representing the volume of water infiltrating in the dike $V_{in,i}$:

$$V_{in,i} = \sum_j v_{i,j} L_{i,j} \Delta t + \left(\theta_i^{n+1} - \theta_i^n\right) \Omega_i \tag{3.18}$$

where v_i denotes the flow velocity between the boundary cell and its adjacent cells evaluated using Darcy's law and L_i is the length of the corresponding interface. The second part of Equation 3.18 takes into account the part of water absorbed by the soil of the cell itself. This volume tends very quickly towards 0 because the boundary cell is saturating almost instantaneously. Using the definition (Equation 3.18) of the infiltrated volume, let us define the equivalent infiltrated height extracted from the cell of the shallow water domain:

$$\Delta h_{in,i} = \frac{V_{in,i}}{L_i} = q_{in,i} \Delta t \tag{3.19}$$

This water height must be removed from the cell at the end of each Richards equation time step and is used to calculate the source term q_{in} of Equation 3.17.

3.5 Model validation

3.5.1 Flow through an embankment

Experiments by Ebrahimi et al. (2007) in which they collected an extensive set of data for the study of seepage flows are used to validate the proposed model. The test consists of applying a tidal wave on a sandy embankment (Figure 3.9).

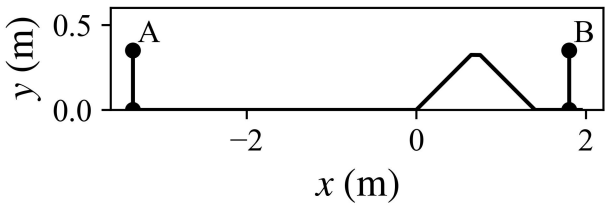


Figure 3.9: Schematic view of the experimental set-up. The two gauges A and B are located at the upstream and downstream sides of the dike, respectively. The tidal wave is applied on the left side of the dike.

On both sides of the embankment an initial 274 mm water level is initially set. The sand is non-cohesive and has a mean diameter of 1 mm and a saturated hydraulic conductivity of 1 cms^{-1}. No other soil parameters are provided by Ebrahimi et al. (2007); therefore, the general features of the test case are reproduced by tuning the parameters of the Mualem-van Genuchten model to typical values for this type of coarse sand ($\alpha = 0.3cm^{-1}$, $\eta = 4$, $\theta_s = 0.5$, $\theta_r = 0.1$). The value of θ_r might seem high for this type of soil, but in the context of this test, the soil remains almost saturated during the whole process, so this parameter is expected to have a negligible influence on the results. A cyclic tidal wave was applied on one side of the embankment and the objective is to observe its influence on the other side.

The tidal wave's equation is the following:

$$z_w(x=0) = 0.214 + 0.06\cos\left(\frac{2\pi t}{355}\right) \tag{3.20}$$

The mean water level of the tidal wave is 0.214m and its amplitude is 0.06m. A 355s period is imposed. The water level variation at up and downstream points of the embankment were monitored during the whole

process. More technical details about the design of this experimental test case are extensively explained in Ebrahimi et al. (2007).

The computed results are illustrated in Figure 3.10. Triangular elements with edges measuring 1cm in length were used to describe the geometry of the dike and information between the two systems was exchanged every 5s, corresponding to the Richards' equation time step. This ensures 71 exchanges during a full tidal cycle of 355s. Again, a 0.001cm numerical threshold was used to ensure the convergence of the Richards' equation solver. Elements describing the shallow-water domain have a width of 1cm, except for the ones located on the dike. On the dike, the elements are precisely aligned with the boundary cells of the Richards' domain, ensuring perfect alignment.

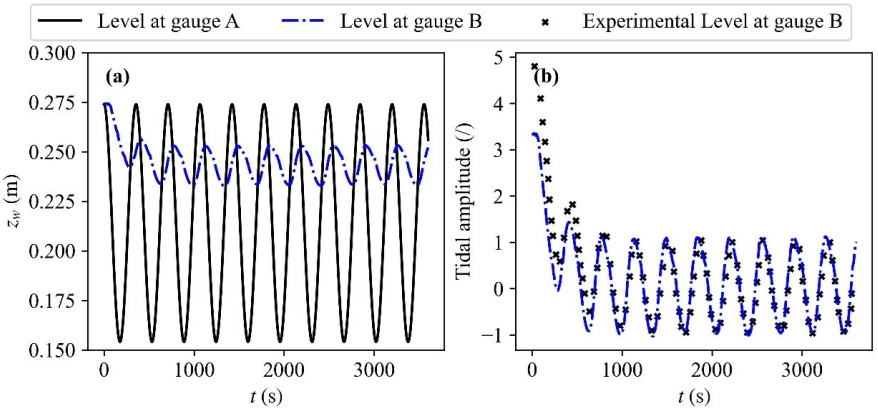


Figure 3.10: Left: numerical evolution of the water level at both sides of the dike. Right: comparison with adimensionalized experimental results

It can be observed that after two oscillations, a steady state takes place at the downstream side of the dike (gauge B, x = 1.8m). The solver successfully replicates the system's steady state characteristics, which include a 90° phase lag between the oscillations of the two water surfaces and a wave amplitude of 0.02m. These results are illustrated in Figure 3.10, showing the amplitude normalized with the steady-state value.

The good agreement in both amplitude and frequency suggests that the saturated hydraulic conductivity, which was the only soil parameter

provided by Ebrahimi et al. (2007), predominantly governs the system's steady state behaviour. To quantify the accuracy of the results, the root mean square error (RMSE) between the experimental and numerical results is computed separately considering that the experiment presents two phases: a transient one and a steady one. The transient state is defined as the initial drop in water level up to the first maximum level reached during the steady state at t = 760 s. The RMSE computed from the adimensionalized tidal amplitude are respectively equal to 0.803 during the transient state and 0.201 during the steady state.

3.5.2 Flow through and over embankment: influence of initial water saturation level

The objective of the current fictive test case is to highlight how initial saturation, as influenced by meteorological conditions, affects the evolution of internal suction head when the dike is subjected to an overtopping flow.

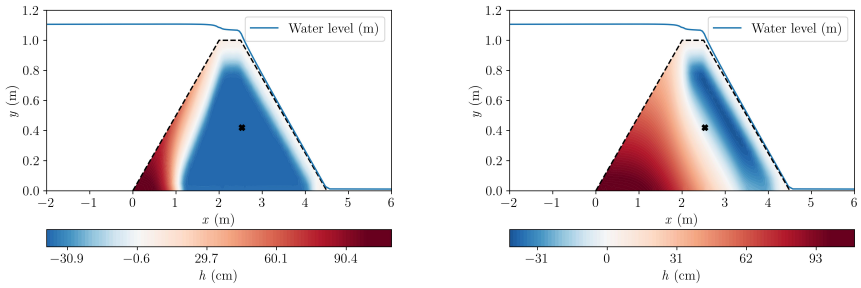
The dike is 4.5m wide and 1m high and its soil has the same parameters as those presented in Table 3.1, excepted for the hydraulic conductivity set to $K_s = 0.05\text{cm}s^{-1}$ and a suction head initialized at $h = -40\text{cm}$. The initial condition for the suction head is uniform in the whole dike. This is a simplification for the purpose of this test case, in reality a hydrostatic suction profile should be expected.

Two cases are presented in which the initial water level at the upstream side is 0.75m. In case (a) a $0.1m^3/s$ flow is directly released on the dike while in case (b) the same flow is released only after 500s.

As a result, it can be observed that during the first 500 s a saturation profile is developed from the upstream part to the downstream seepage face. Due to this profile, the steady state is obtained much faster as the unsaturated soil zone is reduced. In Figure 3.11 we can observe the state of suction head in the soil 20s after the release of the flow for case (a) and case (b). The initial water saturation of case (b) enables the water of the overtopping to penetrate much faster in the soil.

An observation gauge, represented with a black cross inside the dike in Figure 3.11 (x = 2.53m, y = 0.42m) is used to represent the time evolution of the suction head, as illustrated in Figure 3.12.

The comparison of the suction head values at the gauge emphasizes the importance of the initial soil saturation on the full saturation rate.



(a) Suction head distribution for the initially dry dike.

(b) Suction head distribution for the initially wet dike.

Figure 3.11: (a) Unsaturated dike overtopping, (b) saturated dike overtopping. The saturation front is clearly faster in the case of the initially wet dike. The black cross represents the location of the observation gauge.

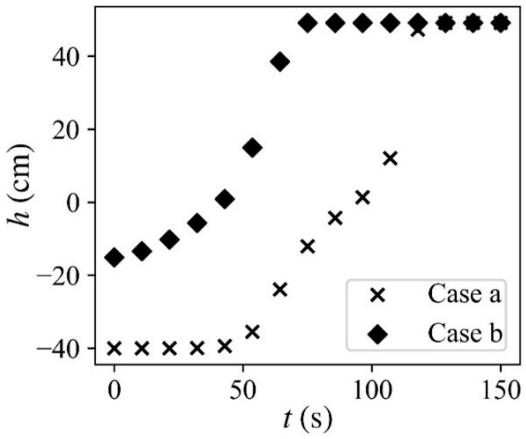


Figure 3.12: Comparison of the suction head evolution from the start of the overtopping at the gauge position.

Indeed, we can observe that the time needed to reach the steady state is two times faster in case of an initially almost saturated dike (Figure 3.11). As the pore pressure is a key factor for the strength of the dike, the time needed to reach full saturation also appears as a key factor.

3.5.3 Flow through and over embankment: influence of saturated hydraulic conductivity

In this section, another test case is presented which examines the impact of different saturated hydraulic conductivities, without changing the other soil parameters, on the subsurface flow and internal suction head of an embankment dike when subjected to overtopping flow.

In Figure 3.13, the influence of the saturated hydraulic conductivity on the unsaturated hydraulic conductivity can clearly be identified. As the saturated conductivity is high ($K_s = 1.cms^{-1}$), the soil is likely to be formed of gravel. Values such as $K_s = 0.1cm.s^{-1}$ or $K_s = 0.01cm.s^{-1}$ can often be associated with sand and lower values ($K_s = 0.001cm.s^{-1}$) represent silt.

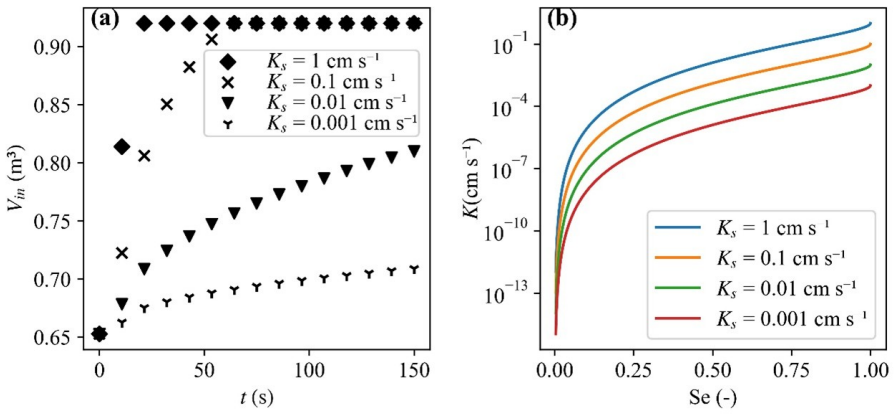


Figure 3.13: (a) Comparison of infiltrated water volume (b) comparison of the unsaturated hydraulic conductivities

The test case is conducted on the same geometry as the previous test case (illustrated in Figure 3.12) and the same overtopping flow is released. The results, as shown in Figure 3.13, clearly demonstrate the significant influence of hydraulic conductivity on the infiltration rate and

internal pore pressure of the dike. The steady state is reached when all available volume in the pores of the soil is filled with water. Given that the dike is fully submerged under water, there is no means for water to escape, making the infiltration rate and internal pore pressure particularly crucial for the stability of the structure. A higher hydraulic conductivity results in faster infiltration and a more significant impact on the internal pore pressure in the short-term. These findings are of great importance for the design and construction of dikes, particularly for clay core and clay surface dikes, as the hydraulic conductivity of the soil must be closely considered to ensure the stability and safety of the structure.

3.6 Conclusion

In this chapter a model that tracks the changes in suction head and saturation degree within an earthen dike subjected to overtopping flows was presented. It consists of a coupled solver for the numerical calculation of sub-surface and the surface flows on unstructured meshes. At first, we developed and validated a finite volume scheme for solving the Richards equation. The model was validated against classical benchmarks, such as the drainage of a soil column or a sharp infiltration front. The simplicity of the formulation but also its ability to solve the equation in the saturated as well as in the unsaturated zone render the solver very interesting for further applications.

The subsurface flow was linked to the surface flow via a source term which allows the mass conservation to be respected. The resulting solver appears to be effective and reveals how the interaction between the surface and subsurface flows and the soil characteristics could affect the internal flow and the evolution of the degree of saturation of the dike, which is a key parameter in dike stability assessment.

We emphasized the importance of the initial saturation degree but also of the saturated hydraulic conductivity on the time needed to reach the steady state. The solver demonstrated its ability to deliver good outcomes across a diverse set of test cases, encompassing complex combinations of flows. Its ability to simultaneously analyse multiple types of soils, focus on pore pressure, and ensure mass conservation through a robust coupling of flows makes it an asset for future numerical

developments.

After this step, the evolution of suction, linked to the apparent cohesion of the soil, can be predicted during an overtopping event. The next chapter focuses on the impact of suction on the shear strength and stress state of soils. In particular, the coupled model developed in this chapter will be used to predict the evolution of suction during overtopping events, which will then be used to assess the stability of the dike.

Key takeaways from this chapter

→ A 2D model is developed to solve for unsaturated flow in porous media, based on the Richards equation.

→ The model simultaneously solves the 2D Richards equation and the 1D shallow-water equations.

→ The coupling of the two systems is validated against experimental data from the literature.

→ It is possible to predict the evolution of suction in dikes subjected to overtopping flows.

→ It is not sufficient to predict the possibility of a failure. The next chapter is dedicated to the impact of suction on the shear strength of soils.

CHAPTER 4

Slope failure initiation in unsaturated earth dikes: shear strength reduction method

The work presented in this chapter is based on two papers (Delpierre et al., 2025; Panzeri et al., 2025) respectively published in Geomechanics for Energy and the Environment and currently under review in Engineering Geology. The first part of this chapter combines the model presented in the previous chapter with the Shear Strength Reduction Method. The proposed approach predicts both the timing and spatial pattern of dike failures during overtopping, including failures along the longitudinal axis and at the breach sidewalls The chapter focuses on the effective stress formulation that is employed to account for the effect of suction on the shear strength of the soil. The second part of the chapter is the result of a collaboration with the group of Prof. Laura Longoni of Politecnico di Milano. It focuses on the modelisation of experimental rainfall-induced shallow landslides. The aim of this part is to show the predictive capability of the model when applied to a different problem than dike breaching.

Contents

4.1 Context **92**
4.2 On stress variables in unsaturated soils mechanics **95**
4.2.1 Effective stress principle in saturated soils . 95
4.2.2 Effective stress principle in unsaturated soils 95
4.2.3 Effective stress formulation used in this work 99
4.2.4 Numerical validation of the effective stress formulation 100
4.3 Model application to dike failures **102**
4.3.1 Longitudinal sliding failure 103
4.3.2 Breach widening 106
4.3.3 An experimental test case: dam overtopping 110
4.4 Rainfall-induced shallow landslide **113**
4.4.1 Experimental setup 115
4.4.2 Experimental test case 117
4.4.3 Numerical simulation of the experimental shallow landslide 118
4.5 Conclusion **121**

Symbol	Description	Units
σ_{ij}	Total stress tensor	Pa
σ'_{ij}	Effective stress tensor	Pa
u_w	Pore water pressure	Pa
u_a	Pore air pressure	Pa
χ	Bishop's parameter	–
h	pressure head (suction head)	m
s	Matric suction ($s = u_a - u_w$)	Pa
q	deviatoric stress invariant	Pa
s_{ij}	deviatoric stress tensor	Pa
p_{net}	net stress	Pa
S_r^m	Microscopic Degree of saturation	–
S_r^M	Macroscopic Degree of saturation	–
S_e	Effective saturation degree	–
τ	Shear strength	Pa
c'	Effective cohesion	Pa
φ	Friction angle	°

A note on the terminology and sign convention:
In the previous chapter, the terms 'suction head' and 'pressure head' (denoted h) were used, which are common in soil science where these quantities are expressed in metres. In this chapter, the geomechanics terminology is used. Here, suction (denoted s) and pore water pressure (denoted u_w) are expressed in Pascals (Pa). The relationship between the two terminologies is as follows:

$$s = u_a - u_w \quad \text{and} \quad u_w = \gamma_w h \tag{4.1}$$

where u_a is the pore air pressure and γ_w is the unit weight of water (in N/m^3). High suction therefore corresponds to a highly negative pressure head. The convention is that compressive stresses are positive.

4.1 Context

Building on the analysis and results of the previous chapters, we can now focus on the role suction plays on the dikes mechanical stability. In their paper, Tingsanchali and Chinnarasri (2001) investigated the competition between the longitudinal sliding failure generated by suction losses and the erosive process using a numerical model and small scale experiments for sandy dikes. Their findings highlighted that the influence of longitudinal slope failure was important to consider when the downstream slopes features a height-to-length ratio above 1:2.5, emphasizing that the erosive process alone was insufficient to fully characterize the underlying physical phenomena. As most river dikes have a downstream slope ratio above 1:2.5, the longitudinal sliding should thus be considered to model accurately their failure.

The dynamics of breach opening plays a major role in the way water rushes into areas that should be protected by dams or dikes. This is why numerical models have been developed with the aim of making better predictions of breach outflows. Nevertheless, most of these models are based on the idea that the breaching is mostly dominated by the erosion process of a non-cohesive material. Therefore, these models consist in solving the shallow-water equations combined with the Exner equation, which is a mass conservation equation (Pontillo et al., 2010; Cantero-Chinchilla et al., 2019; Martínez-Aranda et al., 2023). This approach is the one we presented in Chapter 2. To perform a reliable simulation, specific sediment transport laws are required to catch the general behaviour of the system. The choice of the appropriate law is in general critical for the simulation quality and requires specific calibration, as underlined by Van Emelen et al. (2015). Tingsanchali and Chinnarasri (2001) used such a model combined with a slope stability model based on limit equilibrium, but they did not solve for the water infiltration and did not consider the mechanical behavior of the partially saturated soil but their results show a critical role of an empirical parameter that estimates the pore water pressure inside the dam.

It should be noted that, especially for cohesive materials, the flow through the breach is also influenced to a large extent by the breach widening resulting from lateral block failures (Zhu, 2006), while the erosive process mainly participates to the breach deepening. Some at-

tempts to consider these lateral blocks failures led to the developments of simplified numerical models, such as the bank failure operator, developed by Swartenbroekx et al. (2010), which consists in adjusting the lateral slopes of the breach based only on a given friction angle without considering any cohesion in the material. A high value of friction angle can be used to represent cohesive effects due to suction, but this must be seen as parameter tuning not as a physical representation. The capabilities of this operator were recently assessed in Delpierre et al. (2024) (and recalled in Chapter 2) against small laboratory dike failure experiments involving fine and coarse sand. It was shown that the erosion process was well reproduced by the sediment transport model but that breach widening was over-evaluated by the simplified bank failure model. Recent works by Zhong et al. (2017) or Xue et al. (2021) proposed to account for lateral block failures by using the limit equilibrium method. While a sediment transport law is used for the breach deepening, a planar block collapse is supposed for the breach sides.

These simplified method do not account for soil saturation that also significantly affects the mechanical strength of the dam, which evolves greatly when the dam is exposed to intense rainfalls, droughts and overtopping. Such mechanical strength evolutions are clearly identified as landslides triggering effects and cannot be disregarded (Bogaard and Greco, 2016).

In recent years, extensive research has been conducted to investigate the mechanical behaviour of unsaturated soils, building upon the foundational contributions of Bishop (1954). The exploration of the role of suction and soil saturation on shear strength gave rise to a substantial research effort, leading to the development of new constitutive models using two stress state variables, such as the Barcelona Basic Model (Alonso et al., 1990), or models based on the effective stress principle (Alonso et al., 2010). Arguments against the validity of the effective stress in unsaturated soils state that it cannot explain the volumetric collapse phenomenon upon wetting (Khalili et al., 2022), but as here we are interested only in the shear failure, both approaches lead to similar results. Moreover, the effective stress approach provides a smooth transition from unsaturated to saturated states, which is particularly useful for cases involving fluctuations of the water table like for dikes and dams. Effective stress approaches also requires less model parameters than total

stress approaches and capture well the evolution of the shear strength with suction (Alonso et al., 2010).

In this chapter, the erosion process is overlooked and the focus is set on the geomechanical failures, longitudinal sliding or breach sidewall collapse, that occur during a dike overtopping. The simple bank failure operator's applicability is limited to totally non-cohesive materials and does not extend to cohesive materials or materials exhibiting apparent cohesion due to suction. Moreover, suction tends to evolve during the overtopping event which can not be captured by the simplified bank failure operator. We present an innovative numerical modelling framework for the dynamic assessment of the safety factor of earthen embankments during overtopping. By integrating the coupled surface-subsurface flow solver developped in Delpierre et al. (2023) that was presented in Chapter 3 with an effective stress approach from Alonso et al. (2010), our model provides a robust and physically based method. Using only measurable quantities such as the soil water retention curve and shear strength, the model is able to provide valuable insight into the potential failure of a given embankment during an overtopping event.

The chapter is divided in three main sections. First, in Section 4.2, we will discuss the current state of the art regarding effective or total stress formulations to describe the behavior of unsaturated soils and provide the arguments that both sides present. Second, in Section 4.2.3, we discuss the constitutive model we use to describe the influence of suction on the shear strength of the soil. In Section 4.3, we combine the outcomes of the coupled surface-subsurface flows solver with the effective stress approach. This results in a comprehensive model, able to predict the evolution of the dike's stability under various theoretical situations. The model is successfully compared with experimental data from the literature, accurately predicting the failure onset of an experimental dike subjected to a specific overtopping event. This alignment with experimental results provides additional confidence in our methodology. Section 4.4 extends the model's application to rainfall-induced shallow landslides. Small-scale laboratory experiments conducted at Politecnico di Milano investigated the triggering mechanisms of shallow landslides by rainfall infiltration. The model reproduces the experimental setup, and results demonstrate that it successfully predicts the timing of landslide initiation.

4.2 On stress variables in unsaturated soils mechanics

4.2.1 Effective stress principle in saturated soils

The effective stress principle for saturated soils, formalized by Terzaghi (1936) is a very powerful principle that allows to combine externally applied total stresses, with fluids pressures into an equivalent stress state variable. Let us consider a porous medium filled with one single fluid phase. The effective stress is expressed as follows:

$$\sigma'_{ij} = \sigma_{ij} - u_w \delta_{ij} \tag{4.2}$$

where σ_{ij} is the total stress tensor, u_w is the pore water pressure, defined as $u_w = \gamma h$, and δ_{ij} the Kronecker delta. As recalled by Nuth and Laloui (2008), Terzaghi stated that "all measurable effects of a change of stress of the soil, that is, compression, distortion and change of shearing resistance, are exclusively due to changes in effective stress". Note that the assumption of incompressibility of the fluid phase and of the solid grains is implicitly made here. In classical soil mechanics, the elasto-plastic constitutive models are then supposed to follow this macroscopic perspective of effective stress principle.

This is why Khalili et al. (2004) define the effective stress as the macroscopic effect on the soil skeleton, which means that the effective stress should be seen as the stress responsible for strain.

4.2.2 Effective stress principle in unsaturated soils

While the principle of effective stress is well accepted for saturated soils, its extension to unsaturated soils remains a topic of debate. Most of the time, soils do not remain fully dry or fully saturated, as stated in the Terzaghi's theory. Rather, soils are partially saturated, made of a combination of grains, water and air. This is why Bishop (1954) proposed to extend the effective stress principle to unsaturated soils as follows:

$$\sigma'_{ij} = (\sigma_{ij} - u_a \delta_{ij}) + \chi (u_a - u_w) \delta_{ij} \tag{4.3}$$

where χ is denoted as the Bishop, or effective stress, parameter, and u_a is the air pore pressure. If χ is equal to one, the formulation reduces

to the saturated case, while a value of zero corresponds to a dry soil. In an unsaturated soil, the χ parameter is expected to range between 0 and 1. The term $\chi(u_a - u_w)\delta_{ij}$ thus represents the contribution of suction to the effective stress, and thus to the shear strength of the soil. In a coarse soil, the contribution of the suction to the shear strength is not expected to be high, as water can easily drain. Therefore, χ should rapidly decrease to zero as the soil dries. On the contrary, in a fine soil, suction can have a significant influence on shear strength, which is also related to as apparent cohesion, even for high suction, implying that χ should decrease slower.

To support this formulation, Bishop and Donald (1961) performed triaxial experiments on a cohesionless silt and on a compacted clay. The $(\sigma_3 - u_a)$ and $(u_a - u_w)$ terms were kept constant while varying the cell pressure (σ_3), the pore-water pressure (u_w) and the pore-air pressure (u_a). They observed that the obtained stress-strain curve was unaffected. From this, they deduced that the effective stress principle, formulated as in Equation (4.3), was valid.

And indeed, the formulation is very convenient as it intends to solve a multiphase problem using a single stress variable and is also often written as:

$$\sigma'_{ij} = \sigma_{net,ij} + \chi s \delta_{ij} \tag{4.4}$$

where $\sigma_{net,ij} = \sigma_{ij} - u_a\delta_{ij}$ is the net stress and $s = u_a - u_w = -\gamma_w h$ is the matric suction. It is noteworthy that χ should be equal to one in a saturated soil and zero for a completely dry soil (Khalili et al., 2004).

Intuitively, the χ parameter should then be linked to the saturation degree of the soil, which corresponds to these precited boundaries. While the χ parameter has often been considered equivalent to the saturation degree S_e, as described in the Mualem-van Genuchten model, it was initially intended to be more general.

Nevertheless, this definition, while satisfactory for coarse granular soils, falls short in explaining the behavior of finer-grained soils like clay (Alonso et al., 2010). According to Khalili et al. (2022) there are several experimental evidences against the effectiveness of the saturation degree, S_e, as representation of χ.

The main concern with using the effective saturation degree S_e as representation of χ for clay soil arises from the unrealistic shear strength

reached during a drying process, as the product $S_e s$ tends to extremely large values. As highlighted by Alonso et al. (2010), it is commonly observed that as the saturation degree decreases, the impact of suction on shear strength diminishes. Therefore, a consensus arises that χ should be at least be a function of the saturation degree. Examples of the functions proposed in the literature are provided in Khalili et al. (2022).

A very common criticism against the effective stress principle is that it cannot explain volumetric collapse upon wetting. This critic was formulated quite early in the development of unsaturated soil mechanics in the work of Jennings and Burland (1962). They questionned the conclusions of Bishop and Donald (1961). In particular, they stated that to properly validate the effective stress principle, experiments at constant effective stress should be performed.

Jennings and Burland (1962) presented an experiment that demonstrate the existence of volumetric collapse upon wetting at constant load stress. Following the effective stress principle, a decrease in suction should lead to a decrease in the effective stress and to an increase of volume. But, they observed a volumetric collapse during the wetting of the sample, in contradiction with the effective stress principle.

This criticism is often used to reject the effective stress principle and to support the need of another stress state variable. Nevertheless, Nuth and Laloui (2008) support that this collapse should rather be associated to a plastic mechanism of grains sliding with respect to each other. From this novel interpretation, they argue that the first criticism was not totally correct and maybe based on a misunderstanding.

Indeed, the initial criticisms were formulated within a purely elastic framework. However, if collapse upon wetting is recognized as an elasto-plastic phenomenon, then an appropriate elasto-plastic constitutive law could address the problem, and the effective stress formulation could be adapted accordingly to capture these effects.

To complement the latter argument, Khalili et al. (2004) also noted that even in saturated soils, plastic deformations such as collapse cannot be fully explained by the effective stress principle alone without a proper elasto-plastic formulation.

Supporters of the effective stress principle will finally sustain that the principle is useful since it relies only on a single stress variable and that it treats naturally the transition from unsaturated to saturated

states Khalili et al. (2022).

Two Stress State models

Opponents to the effective stress principle advocate that two independent stress variables are required to solve the issues mentionned before. Fredlund and Morgenstern (1977) proposed that the constitutive behaviour of unsaturated soils should be described by the net stress and the suction, rather than a single effective stress variable. Since then, a variety of constitutive models based on this idea have been developed, such as the Barcelona Basic Model (BBM) by Alonso et al. (1990).

The model adopts two stress state variables driving the mechanical response: the net stress and the suction. This model is an elasto-plastic model, that could be seen as an extension of the Cam-Clay model. Indeed, looking at Figure 4.1 when suction is zero, the model reduces to the classical Cam-Clay model in the plane of the deviatoric stress invariant $q = \sqrt{\frac{3}{2} s_{ij} s_{ij}}$, with $s_{ij} = \sigma_{ij} - \frac{1}{3}\sigma_{kk}\delta_{ij}$ the deviatoric stress, and the net stress $p_{net} = \frac{1}{3}\sigma_{kk} - u_a$.

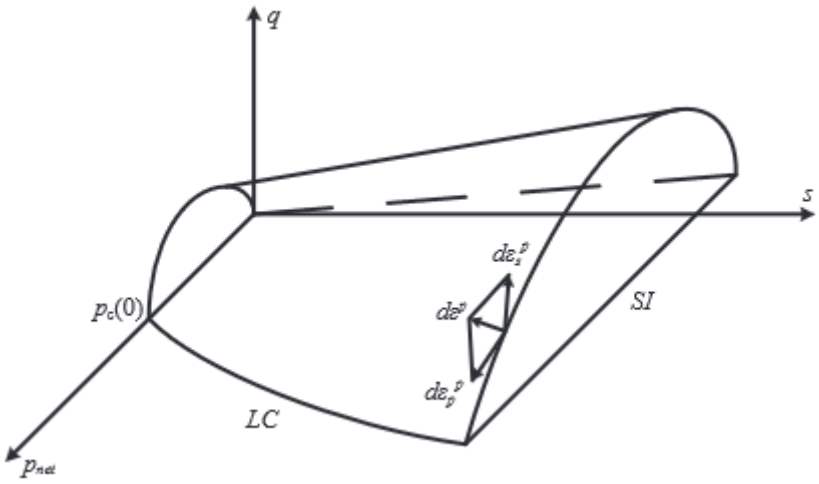


Figure 4.1: Barcelona Basic Model, retrieved from Khalili et al. (2022). SI (suction increase) curve represent the limit of elasticity at high suction. LC (load-collapse) captures the contribution of suction to the plastic behaviour.

The BBM model describes how suction affects the yield surface and

increases it. This surface is essentially bounded by two yield surfaces, depicted in Figure 4.1: the Load-Collapse (LC) curve and the Suction Increase (SI) locus. The load-collapse enables to directly explain the phenomenon of collapse upon wetting which is a key aspect of the model. A soil initially in the admissible stress state zone, can reach the yield surface when suction decreases at constant net stress, leading to plastic deformations and volumetric collapse.

A common argument against the BBM model is that the effect of suction starts directly as suction is applied, without taking into account the air-entry pressure. This is a characteristic of soil water retention curve: a soil can remain saturated with non-zero suction. Other theoretical criticisms of the BBM are formulated and synthetized by Khalili et al. (2022).

4.2.3 Effective stress formulation used in this work

This work uses the effective stress formulation (Equation 4.4) as it conveniently incorporates the effects of suction into the stress state. This formulation is convenient for our purpose where shear failures are predominant. In addition, it mostly relies on measurable quantities, such as the soil water retention curve and shear strength parameters. The main challenge is then to define an appropriate expression for the χ parameter. The common experience is that at high suction and thus low saturation degree, the effect of suction on shear strength tends to diminish. Alonso et al. (2010) proposed a formulation that considers two distinct contributions for the effective saturation degree to model the expected behaviour:

$$S_e = S_r^m + S_r^M \tag{4.5}$$

where S_r^M is the macroscopic degree of saturation and S_r^m stands for the microscopic degree of saturation. There is experimental evidence, presented by Romero et al. (1999) or Romero (2013) of the existence of inter-aggregate porosity (linked to S_r^M) and intra-aggregate porosity (linked to S_r^m). Intra-aggregate porosity contains quasi-immobile water that does not contribute to the soil's mechanical behaviour. In contrast, inter-aggregate porosity is interconnected, facilitating fluid flow and contributing to the soil's mechanical strength.

This formulation solves the issue of unrealistic shear strength increase in fine soils for high suction that occur when $\chi = S_e$ is considered. This particular feature allows to differentiate between granular soil and fine soil with higher clay content. A granular soil presents a high inter-aggregate porosity, leading to a low microscopic degree of saturation S_r^m, which ultimately results in $\chi = S_e$ (the Bishop expression) for $S_r^m = 0$. It is expected that water will totally escape from the pores during a drying process for such soils. On the contrary, as the clay content increases, the microscopic degree of saturation S_r^m should increase accordingly as water can be trapped in the intra-aggregate porosity. In this thesis, sands are often considered and thus $S_r^m = 0$ is assumed unless otherwise specified. The aim of selecting this formulation is to develop a general model able to capture the behaviour of various soil types.

Following all these developments, Alonso et al. (2010) defined an effective degree of saturation such that:

$$S_{\mathrm{r}}^{\mathrm{e}} = \chi = \left\langle \frac{S_{\mathrm{e}} - S_{\mathrm{r}}^{\mathrm{m}}}{1 - S_{\mathrm{r}}^{\mathrm{m}}} \right\rangle \tag{4.6}$$

with $\langle x \rangle = 0.5(x + |x|)$ corresponding to the Macauley brackets, that avoids negative values of χ if $S_{\mathrm{r}}^{\mathrm{m}} \geq S_{\mathrm{e}}$. According to this formulation, χ becomes an expression describing the available water in the macropores, ranging from 0, when water only remains in micropores, to 1, for a fully saturated soil. So Equation 4.4 is employed, considering the specific expression of χ provided above.

Combining Equation 4.4 with the Mohr Coulomb criterion, gives the following theoretical expression for the shear strength:

$$\tau = c' + \sigma \tan(\phi) + \chi s \tan(\phi) \tag{4.7}$$

where c' stands for the cohesion and ϕ is the friction angle. The focus here is on shear failure, but suction also affects the elastic behavior of the soil, which is not accounted for in this study.

4.2.4 Numerical validation of the effective stress formulation

To validate the implementation of the effective stress formulation in our numerical framework, a comparison is conducted between direct shear

test data sourced from the literature and finite element numerical simulations performed using the Moose software (Lindsay et al., 2022). The comparison is based on the direct shear tests conducted by Vanapalli et al. (1996) on glacial till. The soil, characterized by a specific sand/silt/clay distribution of respectively 28%, 42%, and 30%, underwent a drying process over several days.

The measured friction angle was $\phi = 25°$, and an effective cohesion of zero was observed. Multiple tests were carried out with matric suction ranging from 0 to 500 kPa, maintaining a constant normal confining stress of 25 kPa. The experiments were performed using a modified direct shear test apparatus designed by Gan et al. (1988).

Alonso et al. (2010) proposed to fit the soil water retention curve (with the Mualem-van Genuchten model presented in the previous Chapter) using a pore-air entry pressure related parameters $\alpha = 7.2 \cdot 10^{-5} cm^{-1}$, $\eta = 0.59$, $\mu = 0.67$ and a microscopic degree of saturation $S_{\mathrm{r}}^{\mathrm{m}} = 0.64$, which means that a significant intra-aggregate porosity is present.

The Moose Framework is an open-source Finite Element code. It is written in C++ and developed by the Idaho National Laboratory (INL). The code enables the fast development of multi-physics models. The framework is based on the use of kernels that consist of the weak form residuals of any type of PDE. Among the variety of modules available in Moose, we used the Solid Mechanics module to perform the simulation presented here, coupled with the unsaturated porous media flow solver developed in Chapter 3.

The experiments are reproduced numerically considering a unit cubic cell and modelled as a direct simple shear test. The prescribed boundary conditions included a normal confining pressure of 25 kPa and a continuously increasing horizontal displacement applied to the top, periodic conditions are applied on the lateral sides, while the bottom of the cell remains fully fixed. As depicted in Figure 4.2, the numerical results exhibit a strong correlation with the experimental shear strength data. On the contrary, the commonly assumed relationship, where χ is considered equal to the saturation degree (labelled as Bishop shear strength) proves to be unrealistic for the considered glacial till soil, as the shear strength

does not constantly increase with increasing suction.

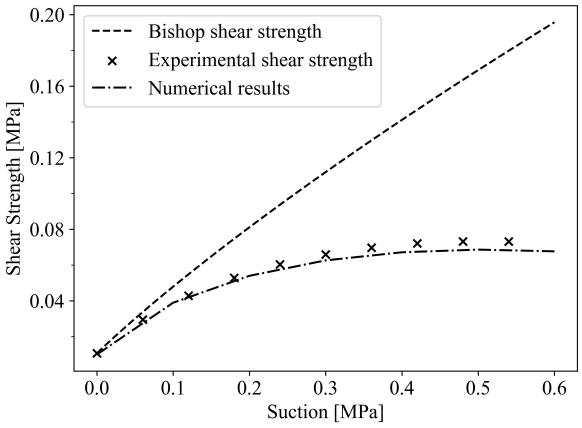


Figure 4.2: Comparison of numerical and experimental direct shear test results. The Bishop shear strength corresponds to the assumption $\chi = S_e$.

The numerical validation shows that integrating the concept of microscopic degree of saturation, $S_{\mathrm{r}}^{\mathrm{m}}$, enhances the accuracy of shear strength evolution with suction. This aspect will be further explored in the subsequent section, which is dedicated to practical applications.

4.3 Model application to dike failures

In this section, we combine the subsurface-surface flow model presented in Chapter 3 with the effective stress model to study realistic, yet fictive, cases. The geomechanical simulations are again performed using the Solid Mechanics module of the Moose software Lindsay et al. (2022).

The safety factor is assessed at various time intervals during a dam overtopping event, employing the shear-strength reduction method (SSRM). This method, first described by Matsui and San (1992), consists in reducing in a linear way the geomechanical properties in the Mohr-Coulomb criteria (see Equation (4.7)), defined by a cohesion and a friction angle, until convergence is no longer achieved in the FEM calculation:

$$c'_{SF} = \frac{c'}{SF}, \quad tan(\phi)_{SF} = \frac{tan(\phi)}{SF} \tag{4.8}$$

where c'_{SF} is the reduced cohesion and $tan(\phi)_{SF}$ is the reduced tangent of the friction angle.

The resulting reduction factor corresponds to the so-called safety factor (SF). Contrariwise to Limit Equilibrium Methods (LEM), there is no need to search for the failure surface through multiple trials, as it is the outcome a unique numerical simulation. In addition, suction, which provides additional strength to the soil, is easily taken into account by remapping the solution of the unsaturated porous media flow to Gauss points constituting the FEM mesh.

Applications of this method are presented in the next sections. First a sensitivity analysis is conducted to investigate the influence of initial conditions and soil water retention curve parameters. The longitudinal sliding failure mechanism is studied in Subsection 4.3.1 whereas Subsection 4.3.2 is dedicated to transversal side failure. These theoretical analysis sections use physical parameters for illustrative purposes only, and these parameters do not correspond to a specific soil type. Then, Subsection 4.3.3 shows a successful validation of the model through a comparison with an experimental example retrieved from the literature.

4.3.1 Longitudinal sliding failure

To enhance comprehension across various cases, the same dam geometry, described in Figure 4.3, is used for both longitudinal failure test cases. It consists in an asymetric dam with a 3:1 upstream slope and a 2:1 downstream slope with a 3 m crest height, a geometry characteristic of river dikes. The initial conditions for the geomechanical calculation consist in the suction distribution within the dam, obtained by solving the subsurface flow. The same mesh with a typical element size of 0.2 m is used for both the flow and geomechanical calculations.

The influence of both fully saturated and unsaturated regions, as well as their temporal changes, in relation to the stability of the dam is highlighted in Subsection 4.3.1.1. The soil hydraulic properties employed in both Section 4.3.1.1 and Section 4.3.1.2 are identical and are described in Table 4.1, with the exception of the parameter α, related to the pore air-entry pressure, whose influence is specifically investigated in Section 4.3.1.2. A cohesion $c' = 5$ kPa and a friction angle $\phi = 25°$ with an associated flow rule are considered for the geomechanical properties.

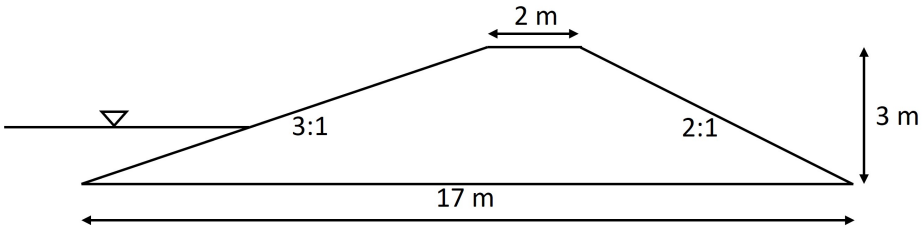


Figure 4.3: Geometry of the asymetric dike used for the theoretical longitudinal sliding failure test case.

Parameter	Value	Unit	Parameter	Value	Units
K_s	0.001	cm s^{-1}	α	0.005	cm^{-1}
θ_r	0.1	-	$\hat{\eta}$	2	-
θ_s	0.4	-	μ	0.5	-

Table 4.1: Soil water retention curve properties.

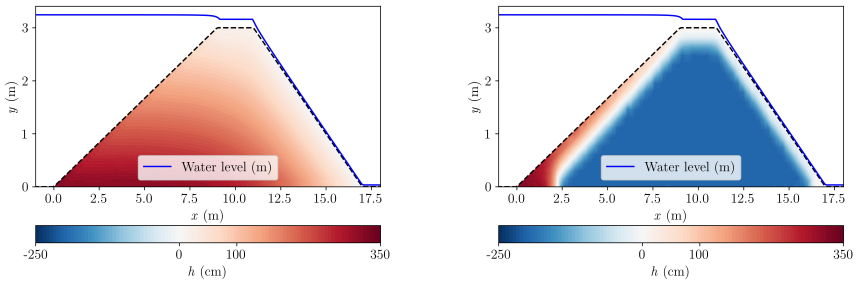
During the overtopping event, generated by a constant upstream flow of 200 $l.s^{-1}$, we expect the failure mechanism to develop at the downstream part of the dam as no load is available to counterbalance the internal pore pressure. The coupling between the shallow-water system and the Richards equation is performed every 10 s.

4.3.1.1 Influence of the initial saturation degree

Throughout a classical exploitation, an earthen dam undergoes various meteorological conditions. Rain and droughts significantly affect the soil's water content and thus its shear strength. In this test case, we compare the evolution of the safety factor during an overtopping event for an initially dry dike, corresponding to a homogeneous initial suction head h = -200 cm, and for an initially wet dike, with an initial suction head h = -20 cm. These initial conditions are selected for the purpose of the theoretical analysis only. A more realistic initial condition could be obtained by simulating a long-term infiltration process considering meteorological data or considering a phreatic level at a given depth and assuming a hydrostatic distribution of the suction head.

Figure 4.4 shows the suction head distribution after a 500 s flow for both initial conditions. The steady state is already reached for the wet

dike, whereas the water struggles to infiltrate the dry dike.



(a) Suction head distribution for the initially wet dike.

(b) Suction head distribution for the initially dry dike.

Figure 4.4: Comparison of the suction head distribution after 500 s of dike overtopping. The dike saturates more rapidly in the case of the initially wet dike.

As observed in Figure 4.5, the safety factor is influenced to a large extent by the initial water content condition. The decrease in safety factor, associated with the evolution of the saturation degree in the dam during the overtopping, is particularly pronounced in the case of the initially wet dam.

The time taken to reach the threshold safety factor of 1.5 (which is a common threshold in geotechnics) is notably faster for the initially wet dam than for the initially dry one. The latter does not even reach the threshold after 1000 s of overtopping event.

The initial presence of water influences greatly the infiltration rate as water tends to circulate in the already filled areas. These results allow to underline the need of maintaining proper saturation degree conditions inside a dam in operation.

4.3.1.2 Influence of pore air entry pressure

Among the parameters of the soil water retention curve, the pore air-entry pressure seems to be the one which influences the most the shear strength. By strongly influencing the value of the α parameter, it also strongly influences the saturated water content plateau (see Figure 3.1).

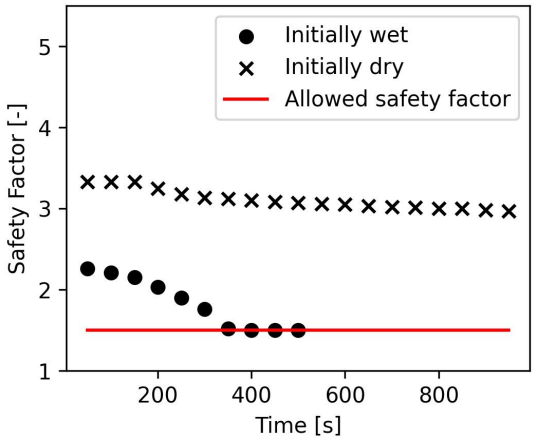


Figure 4.5: The evolution of the safety factor, computed with the shear-strength reduction method, for both an initially dry and an initially wet dike subjected to overtopping.

If the α parameter is low, the soil tends to stay at high volumetric water content values even for high suction. This particular behavior causes the soil to reach full saturation more rapidly, consequently accelerating the reduction in mechanical capacities. This, in turn, results in a faster decline of the safety factor, as illustrated in Figure 4.6.

4.3.2 Breach widening

This test case studies the lateral widening of a breach. The modelled scenario is designed to replicate the behavior of a dike that has been eroded up to its sandy core. The influence of the initial groundwater level, which is a result of the past hydrological conditions, on the potential breach side failure is emphasized. The geometry of the test case is presented in Figure 4.7, where the water table is represented as well as a water depth representing the flow in the normal direction. A 0.05 m typical mesh size is considered along the breach, while a coarser mesh of 0.1 m typical mesh size is used for the rest of the domain.

A 50 cm water depth is considered in the breach and the soil's hydraulic parameters are presented at Table 4.2. The Richards equation time step is set to 10 s. The same soil's geomechanical properties are used

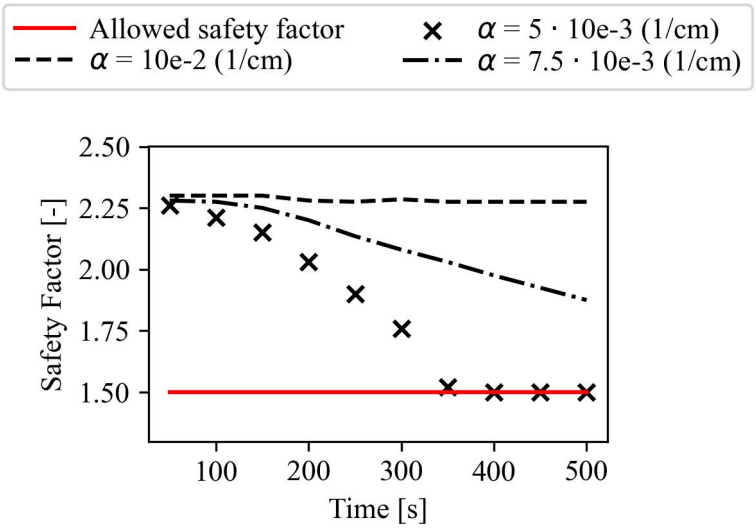


Figure 4.6: Safety factor comparison for different values of the α parameter, related to the air-entry pressure.

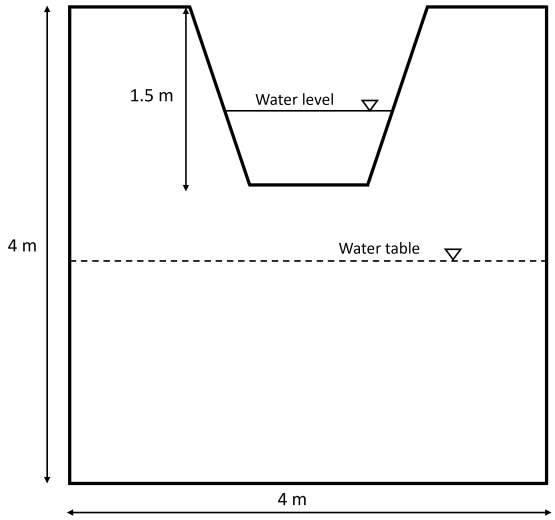
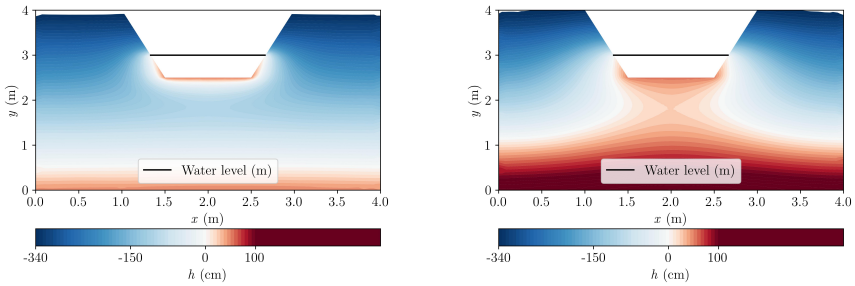


Figure 4.7: Geometry of the test case. The breach is represented as a trapezoidal shape.

Parameter	Value	Unit	Parameter	Value	Units
K_s	0.01	cm s^{-1}	α	10^{-3}	cm^{-1}
θ_r	0.1	-	$\hat{\eta}$	2	-
θ_s	0.4	-	μ	0.5	-

Table 4.2: Soil water retention curve properties selected for the theoretical analysis.

than in the previous section: a 5 kPa cohesion, a 25° friction angle and a dilatancy angle of 15° with a microscopic degree of saturation $S_r^m = 0.1$. The horizontal displacement is restricted on the lateral sides, while the bottom of the domain is fully fixed. Suction head evolves in time and a specific distribution is obtained depending on the initial groundwater level as observed in Figure 4.8.



(a) Suction head distribution at t = 10 s. (b) Suction head distribution at t = 50 s.

Figure 4.8: Suction head evolution from 10 s to 50 s for an initial water level at 0.5 m.

The safety factor is evaluated for each scenario after a 50-second flow simulation, providing an objective basis for comparing the different cases. A rotational block failure mechanism is visible as the FEM calculation stops to converge. An illustration of a typical potential failure surface can be seen at Figure 4.9.

It shows that in the case of a cohesive material, led by suction forces, a rotational failure mechanism is likely observed rather than a sliding failure. Potential effect of the size of the geomechanical domain was not explored in the context of this work. The observed failure pattern seems

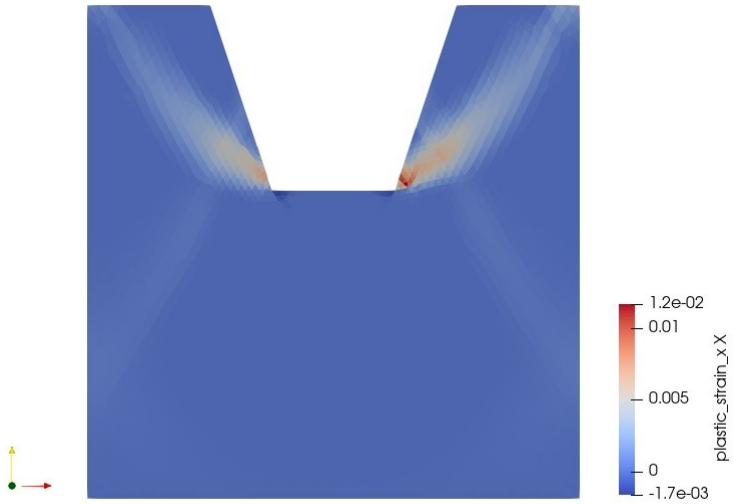


Figure 4.9: Rotational failure surface. The figure corresponds to the observed plastic strain field at the lowest safety factor.

coherent but further investigations would be required to ensure that the domain size does not lead the failure mechanism in this specific case.

The safety factor associated to each situation is strongly influenced by the initial groundwater level, as shown at Figure 4.10. This is mainly due to the fact that the initial groundwater level influences the rate of saturation in the dam.

The higher the initial groundwater level, the lower the safety factor becomes. The dynamics of breaching and the likelihood of block failures propagating laterally are significantly affected by the degree of saturation. Consequently, traditional bank failure models that rely solely on the friction angle fail to adequately represent this behavior.

Although a wet material will tend to fail faster, it should be noted that our model does not account for desiccation cracks, which also affect failure when the soil undergoes high suction. It can be concluded that keeping optimal saturation degrees is crucial in the way breaching will propagate laterally due to block failures.

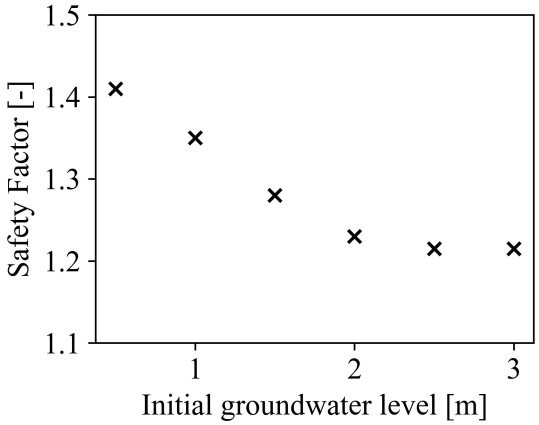


Figure 4.10: A comparison of the safety factor for different initial groundwater levels after 50 seconds for the lateral block failure mechanism.

4.3.3 An experimental test case: dam overtopping

Awal et al. (2008) presented the results of various experimental overtopping embankment failures. One of these tests exhibited a geomechanical failure by longitudinal sliding caused by the combined action of surface flow forces and the variation in water content in the soil. The geometry of the test case is represented in Figure 4.11.

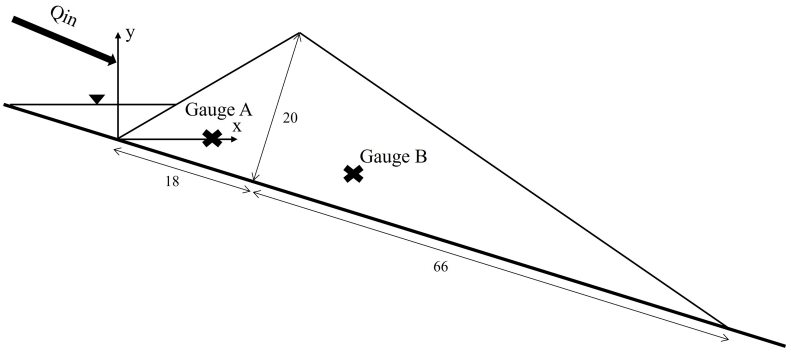


Figure 4.11: Geometry of the test case. The dike has a triangular shape and is located in a slope.

It consists of a sandy dike, built on a 5-meter long slope, with a

steep upstream slope and a smoother downstream slope. The soil water retention curve parameters were measured and are described in Table 4.3. Initially the saturation degree S_e is set to 20 %.

Parameter	Value	Unit	Parameter	Value	Units
K_s	0.03	cm s^{-1}	α	0.055	cm^{-1}
θ_r	0.045	-	$\hat{\eta}$	3.2	-
θ_s	0.287	-	μ	0.312	-

Table 4.3: Soil water retention curve properties.

The geomechanical properties of the sand are the one of a cohesionless sand with a 34° friction angle. A 30.5 $cm^3 s^{-1}$ constant inflow discharge was imposed at the upstream end of the setup. The sandy dike is overtopped after approximatively 300 s and a sliding failure is observed after 447 s.

4.3.3.1 Comparison with the coupled surface-subsurface flows model

A typical mesh size of 0.01 m is used for the dike in the numerical simulation, and a time step of 10 s is used for the Richards equation. The threshold for the convergence of the Richards equation solver is set to $1 \times 10^{-3} cm$. The shallow-water domain is discretized using a 0.01 m mesh size on the full length of the flume. The outcomes generated by the numerical model were compared with the volumetric water content data recorded at two gauges throughout the experiment. Although the exact positions of these gauges were not explicitly specified in the original paper, they were estimated to be at the coordinates listed in Table 4.4.

Gauge	X	Y
A	0.13	0
B	0.31	-0.05

Table 4.4: Gauges position.

Initial simulations with the parameters of Table 4.3 resulted in an overshoot in the saturation degree evolution, with the model response outpacing the measured data.

Given the significant uncertainties associated with both gauge positions and the measurement of saturated hydraulic conductivity, the latter parameter was adjusted to $K_s = 0.015\ cm.s^{-1}$, which remains in the same order of magnitude. The final results are presented at Figure 4.12, where the wetting process is compared and visually validated.

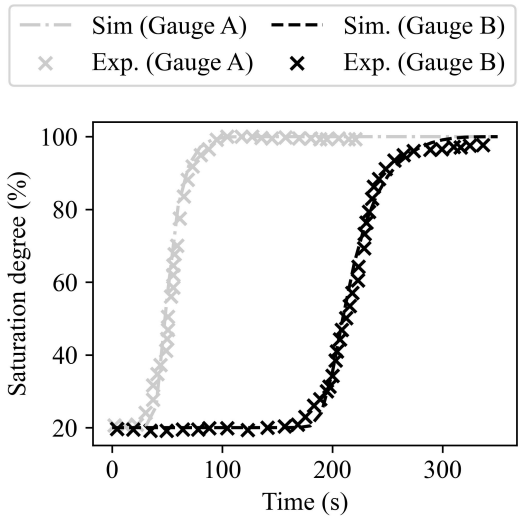


Figure 4.12: Comparison between experimental (crosses) and numerical results (dashed).

4.3.3.2 Safety factor evolution

The same mesh is used for the geomechanical computation than for the Richards equation. The safety factor is assessed during the event using the shear strength reduction method detailed earlier. Considering the nature of the soil, with likely coarse grains, a microscopic degree of saturation $S_r^m = 0$ was selected. Also, a 60 Pa cohesion was considered for the material, preventing local non physical convergence of the SSRM process. The boundary condition applied on the bottom of the dike is a full restriction of the displacement, which seems reasonable given the expected shear failure mechanism located in the dike body. The safety factor evolved greatly throughout the event as shown on Figure 4.13.

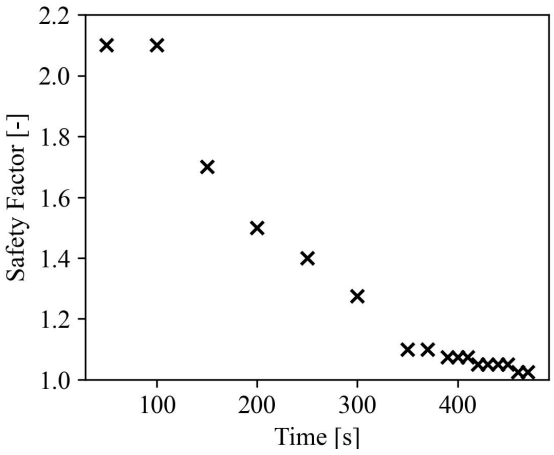


Figure 4.13: Safety factor evolution of the downstream slope during overtopping.

Initially, the safety factor is high, with a 2.1 value. Then, the safety factor evolves as a consequence of the changing water content, leading to a higher density but also to important cohesion losses.

Finally, after approximatively 460 seconds the safety factor drops to 1.02 meaning that the dike is close to instability. The obtained failure surface is evaluated and represented on Figure 4.14 along with the experimental slip surface. Strong similarities appear between the calculated surface and the experimental one displayed Awal et al. (2008). The stress path in the $p' - q$ plane, (mean effective stress versus deviatoric stress) is computed and is represented in Figure 4.15. The stresses are recorded at the point $x = 0.205, y = 0.081$ m, which is located in the middle of the shear band. Initially, the effective stress increases as the water level on the dike rises. Then, as water infiltrates, the degree of saturation increases and the weight of the water is counterbalanced. This leads to a final decrease in mean effective stress and failure.

4.4 Rainfall-induced shallow landslide

Shallow landslides are powerful and unpredictable natural events, capable of causing extensive destruction despite their typically limited size and depth. Once initiated, these landslides can rapidly accelerate, devastating

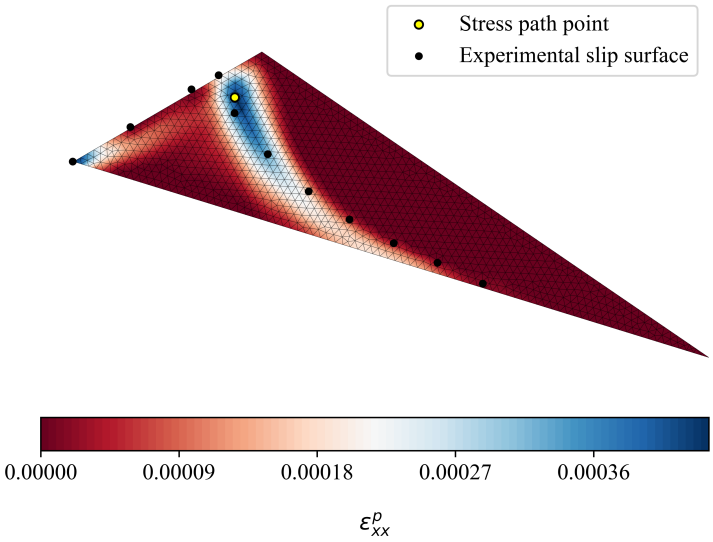


Figure 4.14: Comparison between numerical and experimental slip surfaces. The computed plastic strain in the x direction is plotted.

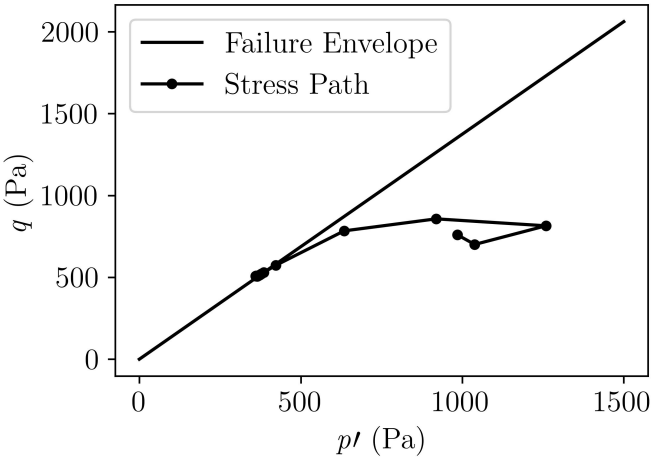


Figure 4.15: Stress path in the $p' - q$ plane in the middle of the shear band. The mean effective stress p' decreases following the increase in pore pressure.

properties and claiming lives (Bugnion and Wendeler, 2010). Given their hazardous nature, enhancing our understanding of shallow landslides and the various factors influencing slope stability is crucial for effective prevention, prediction, and risk mitigation.

To study the physics behind rainfall-induced shallow landslides, experiments were conducted at the Gap2Lab (Laboratorio di Geologia e Geofisica Applicata) at the Lecco Campus of Politecnico di Milano. In this laboratory, a small-scale landslide simulator was developed to replicate conditions leading to shallow landslides.

4.4.1 Experimental setup

The landslide simulator (depicted in Figure 4.16) featured a plexiglass flume divided into two rectangular planes. The upper one held the soil at an imposed slope, which could be achieved by using a motorised system to tilt the flume to the desired slope. The lower plane serves as a transition zone for material from the collapsed upper soil. A geogrid was installed on the surface of the tiltable plane to realistically simulate the bedrock of the slope. The geogrid (High Friction Tenax HF produced by TENAX) guarantees basal friction, enabling the basement to reach an inclination up to 36°, which corresponds to its friction angle, without causing soil slippage. For this research project, the inclination was consistently set between 33° to 35°.

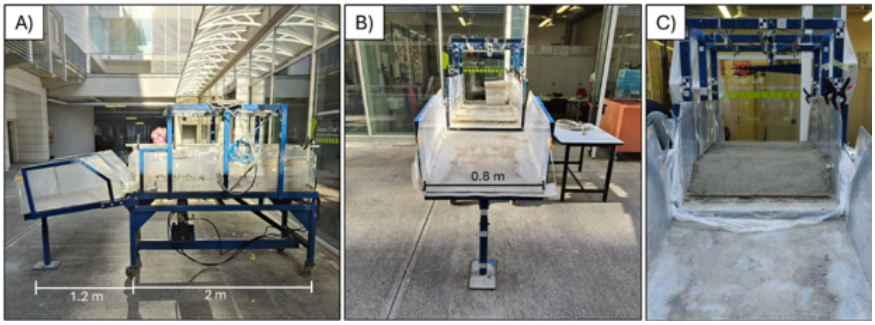


Figure 4.16: Shallow-landslide simulator geometry without soil lateral view (a) Front view (b) Simulator with a soil layer of 15 cm positioned on the slab (c)

In the preparation phase, sand with a dry density of 2650 kg/m^3 was placed in the flume, reaching a soil thickness of 15 cm. This value

was chosen to simulate a real thickness of about 1 meter, using a scale factor of 6. The total soil weight, around 300 kg, was measured, and the volume, around 0.2 m^3, was calculated geometrically. This allowed for determining the bulk density and porosity of the sample.

Additionally, the landslide body ends with a foot wedge, inclined at around 30°, set to maintain initial soil stability.

The rainfall event is simulated through four sprinklers located on the metallic frame and properly oriented to provide homogeneously water to the landslide body. This system was previously calibrated to accurately convert the pressure of the water outgoing from a tap to a rainfall value in millimetres per hour (mm/h).

The setup is also equipped with cameras, tensiometers, water content sensors. Electric Resistivity Tomography (ERT), visible in Figure 4.17, is also used to monitor the evolution of the water content in the soil during the rainfall event.

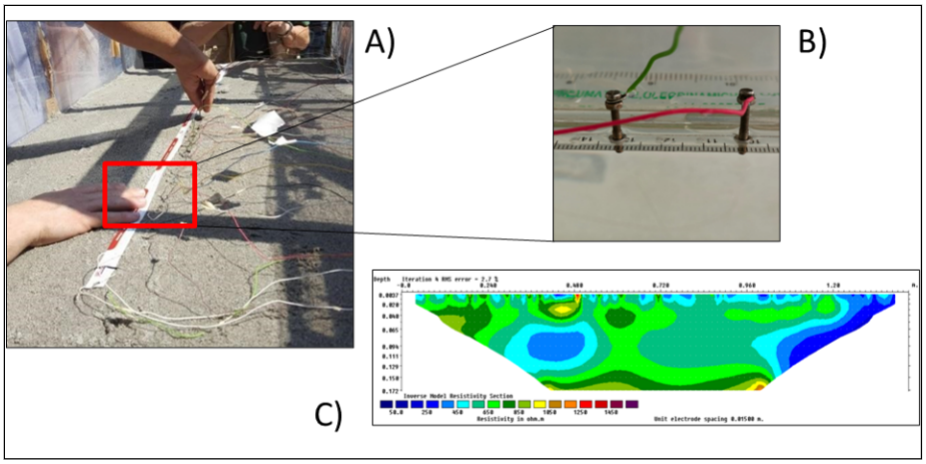


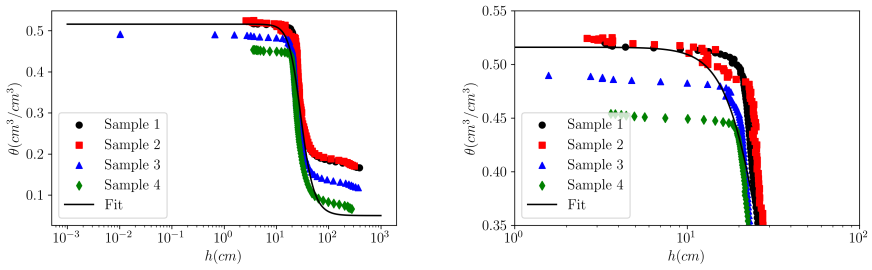
Figure 4.17: ERT DC geophysical system. 48 electrodes located on the surface of the landslide (a) Downscaled stainless steel electrodes (b) Example of inverted section obtained with Res2DInv (c)

Longoni et al. (2025) present detailed information about the experimental setup, instrumentation and experiments performed at the Gap2Lab.

4.4.2 Experimental test case

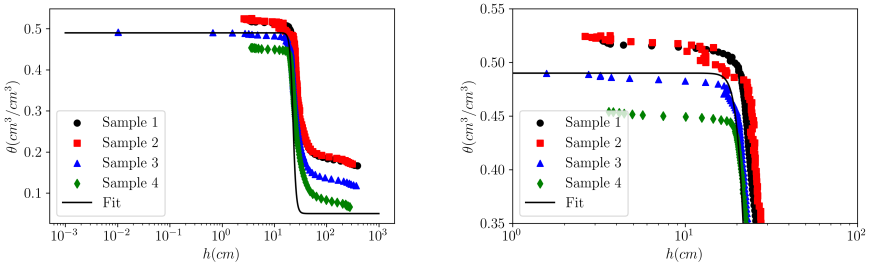
In this section, we present the results obtained for one specific experimental case. Other experiments and analysis can be found in Panzeri et al. (2025), different rainfall patterns, or different material properties were studied.

An industrial sand with a d_{50} of 0.35 mm was used for the test presented here. The soil water retention curve parameters are presented in Table 4.5. The value of the parameter η is very high, which indicates a very uniform pore size distribution. This is consistent with the fact that the sand is an industrial one, that has been filtered. Figure 4.18 presents the Hyprop measurement result and the fitted Mualem-van Genuchten curve obtained with the Hyprop-fit software. A η value of 3.96 and a α value of 0.037 cm^{-1} are obtained. The set of value provides a lower RMSE (0.053) than the one obtained with the parameters of Table 4.5 (RMSE = 0.139). Here, the aim is to provide an estimate of the time to failure of the slope subjected to rainfall. This means that the near-saturation region of the soil water retention curve is of particular importance, as it will influence the rate of saturation and thus the rate of strength loss. The parameters were manually adjusted to provide a better fit in the region of suction head h below to -20 cm. Figure 4.19 shows the resulting curve, with the adjusted parameters that provide a RMSE of 0.024 in the near-saturation region while the Hyprop-Fit paramers provide a RMSE of 0.027 in the same region.



(a) (b)

Figure 4.18: (a) Measurement of the soil water retention curve for the industrial sand with fitted Mualem-van Genuchten parameters. (b) Zoom on the near-saturation region. The fit is performed by the Hyprop fit software.



(a) (b)

Figure 4.19: (a) Measurement of the soil water retention curve for the industrial sand with fitted Mualem-van Genuchten parameters. (b) Zoom on the near-saturation region. The fit has been modified and manually adjusted to provide a more accurate representation of the near-saturation region.

Parameter	Value	Unit	Parameter	Value	Units
K_s	0.071	cm s^{-1}	α	0.044	cm^{-1}
θ_r	0.05	-	$\hat{\eta}$	15	-
θ_s	0.49	-	μ	0.93	-

Table 4.5: Soil water retention curve properties of the industrial sand.

This test, whose geometry and parameters are depicted at Table 4.6, aims to reproduce a two-phase rainfall event. The two events have the same precipitation intensity of 62.5 mm/h, with a 6 min break in the rainfall. The failure of the slope followed the retrogressive pattern. Its development is consequent to the first crack which occurred 34 min from the beginning. The initial volumetric water content θ is measured to be 0.15.

4.4.3 Numerical simulation of the experimental shallow landslide

Based on the soil properties and the geometry of the problem, a numerical model is built to simulate the event. An unstructured triangular mesh is generated to represent the particular geometrical feature with a 2cm typical element size. The same mesh is employed for both the subsurface flow simulation and the geomechanical stability evaluation.

Table 4.6: Slope features and triggering factors.

Category	Parameter	Value
Slope features		
Geometrical features	β [°]	33
	Base high [m]	1.80
	Base low [m]	1.20
	Height [m]	0.17
	Soil weight [kg]	300.6
Triggering factor and collapse		
Rainfalls details	P [mm/h]	62.5
	Stop duration [min]	6
	Stop beginning [min]	8
	Stop ending [min]	14
	Time first fracture [min]	34

The initial condition of $\theta = 0.15$ corresponding to an initial suction head of $h = -24.9cm$ is selected. The rain is imposed at the top-soil boundary as an input flow boundary condition, a transmissive (seepage face) boundary condition is set at the end of the slope and the bottom is a wall bottom condition.

In this case, a constant 62.5 mm/h rain is imposed at the top-soil boundary for 8 min and then stopped for 6 min. The rain is reactivated and finally provokes the failure. Figure 4.20 shows the suction head and the volumetric water content distribution after 15 min of experimental procedure. Water then settles at the bottom of the slope and slowly flows downward.

Nine min later, after 25 min of experimental measurement, the water is seeping out the slope, as shown in Figure 4.21. The instability is therefore expected to come soon.

The safety factor is again evaluated all along the subsurface flow simulation as shown in Figure 4.22. A 35ř friction angle is considered with an associated flow rule and a cohesion of 0 Pa. The estimated change in stress state suggests that the failure of the slope is after 34 min. This provides a fairly satisfactory reflection of reality: experimentally, the first (small) crack was observed after 34 min.

This test case demonstrates that the combination of a comprehensive

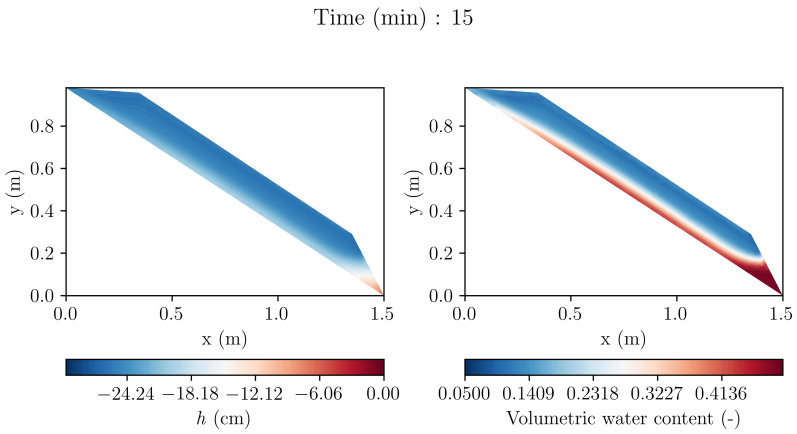


Figure 4.20: Suction head and volumetric water content distribution after 15 min of rainfall.

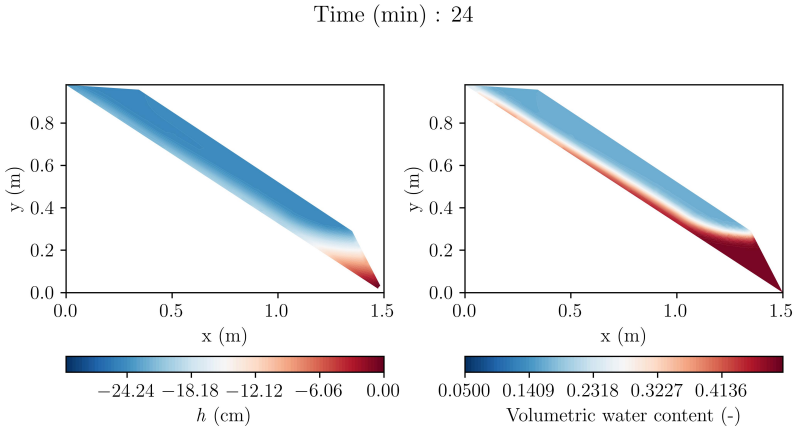


Figure 4.21: Suction head and volumetric water content distribution after 24 min of rainfall.

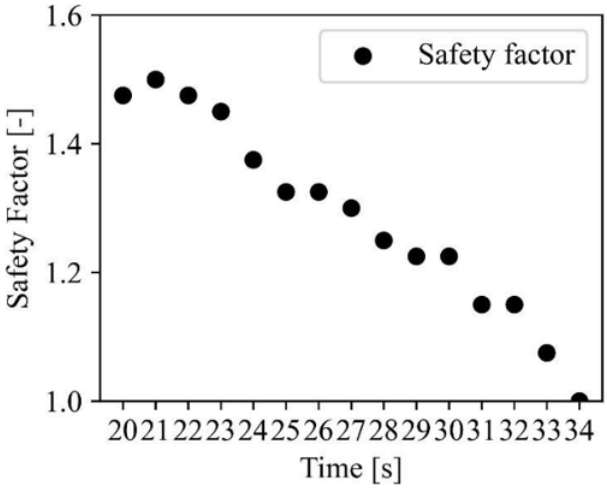


Figure 4.22: Safety factor evolution in time during the rainfall event. The safety factor reaches a value of 1 at the time of the first crack (34 min).

physical description of unsaturated porous media flow and an appropriate effective stress formulation can successfully predict the initiation of shallow landslides in well-controlled laboratory conditions.

4.5 Conclusion

In this chapter, we presented a model that predicts the evolution of stability in earthen embankments subjected to overtopping flows, relying solely on physical parameters. The model accounts for the impact of overtopping on the subsurface flow, which in turn influences the shear strength, the soil's density and thus the stability of the structure.

We first discussed the various possibilities described in the literature to model the impact of suction on the geomechanical properties of the soil. We presented the effective stress formulation, developed by Alonso et al. (2010), used to describe the relationship between suction and shear strength evolution. We showed that, using this law, we were able to numerically reproduce direct shear test data, retrieved from the literature. This proves that the selection of an appropriate plastic law combined

with an effective stress formulation is an adequate way of approaching the simulation of shear failure occurring in unsaturated soils.

The combination of the surface-subsurface flows model with an appropriate effective stress formulation, is the main novelty of this chapter. From the soil water retention curve and the saturated shear strength, the evolution of the stability of the embankment subjected to different events is predicted.

We showed several theoretical applications where the model proved to perform physically. We then showed that the model is effectively able to predict the onset of failure by successfully comparing with a complex experimental failure. We were able to reproduce not only the subsurface flow, but also the failure mechanism and the onset time.

These developments demonstrate that the effects of pore pressure variations on dam stability during overtopping events should not be overlooked, as relying on a simplified bank failure operator that ignores soil suction and cohesion can lead to unrealistic results in many situations.

Finally, we discussed of the problematic of rainfall-induced shallow landslides. This allowed to show that the range of application of the model is not restricted to dike failure. After describing the experimental setup and one specific experiment, we managed to successfully predict the failure mechanism and time of the slope.

Still, the current model is not able to predict the peak discharge flow during overtopping events. A comprehensive physical model should account for erosion by relying on appropriate sediment transport laws, but also for large displacements that occur during the failure (blocks failure, slope sliding). The large displacements of the geomechanical model is an aspect that will be discussed in the next chapter. The combination of all these aspects will ultimately lead us to the comprehensive physical model we are looking for in this thesis.

Key takeaways from this chapter

→ Combining an effective stress formulation with an appropriate elasto-plastic model is an adequate way of simulating shear strength evolution in unsaturated soils.

→ The geomechanical model is combined with the surface-subsurface flow model.

→ The shear strength reduction method is used to evaluate the safety factor of a given scenario.

→ The model is able to predict the evolution of the safety factor during overtopping events.

→ The model successfully predicts the sliding failure of an experimental dam overtopping case.

→ The model is also applied to the simulation of rainfall-induced shallow landslides.

→ The model cannot reproduce large soil displacements, but only predicts the onset of failure.

CHAPTER 5

Slope failure propagation in unsaturated earth dikes: Particle Finite Element method

The model developed in the previous chapter predicts dike slope failure initiation due to overtopping but cannot reproduce large displacements. Here, we present different methods available in the literature to simulate large displacements of materials. Then, we focus on the Particle Finite Element Method (PFEM), a lagrangian method based on an efficient remeshing algorithm. This chapter is the result of a collaboration with colleagues from Applied mechanics and mathematics, especially with Dr. Thomas Leyssens and Prof. Jean-François Remacle. We explain the underlying principles of the approach and demonstrate its application to geomechanical problems. Specifically, we employ Cosserat theory as a means to mitigate mesh dependence, which commonly arises from strain localisation associated with the softening behaviour of geomaterials. We show that a range of realistic geomechanical scenarios, such as landslides and slope stability can be effectively simulated.

Contents

5.1 Context **128**

5.2 The Particle Finite Element Method 133
5.3 Application in the classical Cauchy mechanics framework 139
5.3.1 Perfectly plastic slope failure 142
5.3.2 Granular column collapse 145
5.3.3 Retroactive slope failures 149
5.3.4 Biaxial testing to underline strain softening? 157
5.4 Cosserat continuum theory to mitigate mesh dependence 159
5.4.1 Benchmark - shear band 164
5.4.2 Retroactive slope failure 167
5.5 Conclusion 168

Symbol	Description	Units
α	Desired element size	m
R_e	Circumcircle radius of element e	m
α_e	Ratio between circumcircle radius and desired element size	–
$\boldsymbol{\sigma}$	Stress tensor	Pa
$\boldsymbol{\varepsilon}$	Strain tensor	–
$\boldsymbol{u}$	Displacement vector	m
$\boldsymbol{D}^e$	Elastic Stiffness tensor	Pa
E	Young's modulus	Pa
ν	Poisson's ratio	–
$\boldsymbol{f}$	Body force vector	$\mathrm{N} \cdot \mathrm{m}^{-3}$
ρ	Density	$\mathrm{kg} \cdot \mathrm{m}^{-3}$
$\overline{\epsilon}^p$	Equivalent plastic strain	–
c	Cohesion	Pa
ϕ	Friction angle	$^\circ$
ψ	Dilatancy angle	$^\circ$
$\boldsymbol{M}$	Mass matrix	kg
$\boldsymbol{C}$	Damping matrix	$\mathrm{kg} \cdot \mathrm{s}^{-1}$
$\boldsymbol{K}$	Stiffness matrix	$\mathrm{N} \cdot \mathrm{m}^{-1}$
η	Rayleigh damping coefficient	–
ζ	Rayleigh damping coefficient	–
$\boldsymbol{\tau}$	Cosserat stress tensor	Pa
$\boldsymbol{\mu}$	Cosserat couple-stress tensor	$\mathrm{Pa} \cdot \mathrm{m}^{-1}$
$\boldsymbol{\kappa}$	Curvature strain tensor	m^{-1}
$\boldsymbol{\gamma}$	Cosserat strain tensor	–
$\boldsymbol{\omega}$	Cosserat rotational component	–
$\boldsymbol{I}$	Cosserat micro inertia tensor	m^2
K	Bulk modulus	Pa
G	Shear modulus	Pa
G_c	Cosserat shear modulus	Pa
M	Cosserat couple coefficient	$\mathrm{Pa} \cdot \mathrm{m}^2$
M_c	Cosserat couple coefficient	$\mathrm{Pa} \cdot \mathrm{m}^2$
R	Cosserat grain radius	m

5.1 Context

In the previous chapter, we presented a geomechanical model that, when combined with the surface-subsurface flow model developed in Chapter 3, is able to predict the onset of dike failure due to overtopping. The ultimate goal of the thesis is to simulate the full breaching of dikes, that potentially involves large displacements of the soil. This chapter explores the Particle Finite Element Method (PFEM) as a potential solution to handle large displacements in geomechanics, keeping as final objective the ability to model the failure of an overtopped dike.

The prediction of slope stability has traditionally been approached using limit equilibrium methods, where a safety factor is computed as the ratio of the resisting forces to driving forces (Yu et al., 1998). While these methods are practical in that they provide a quick answer to evaluate the stability of a given slope, they require an iterative procedure to find the failure surface and are unable to predict the full extent of the failure and rely on simple constitutive laws.

Following the development of the Finite Element Method (FEM), the shear strength reduction method has been widely used to evaluate the safety factor of slopes. In this framework, as developed in the previous chapter, the slope stability is assessed by progressively reducing the shear strength of the soil, which consists of cohesion and friction angle in the case of a Mohr-Coulomb type constitutive law. The initiation of failure and its shape are detected, like in limit equilibrium methods, but the extent, or runout, of the failure cannot be obtain.

However the geomechanical processes such as landslide, block failure or pile installation involve large deformations in the soil, making it impossible for classical mesh-based approaches such as the FEM to solve these problems once the distortions become too large. For example, in the case of dike breaching, if a shear band is developed and that a block of soil fails accordingly, the mesh elements will be strongly distorted. Yet, a well known condition, described by Babuška and Aziz (1976), is that no angle of any element should be too close to 180°. Moreover, the domain is moving in space and changes in boundary conditions are impossible to detect in a classical FEM framework.

In the context of large displacements framework, a special attention must be paid to the evolution of boundaries in order to accurately

track the geometrical evolution and apply proper boundary conditions. Considering the case of dike breaching, the free surface of the failing dike may evolve significantly and so will the boundary conditions applied on this surface. The convergence of the model should also be ensured despite the strong distortions of the domain.

Such issues led the computational mechanics community to develop various solutions to handle large displacement simulations. Two categories of methods can be identified: discrete methods and continuum-based methods. Here the focus is set on continuum-based methods.

Continuum-based methods

In a classical small-strain FEM framework, the calculations are performed based on the undeformed initial mesh. This is valid for problems with small deformations but becomes inaccurate when large displacements occur.

This is why the Updated Lagrangian and Total Lagrangian approaches have been developed. In these approaches, the classical small strain assumption is abandoned. A critical issue with the small strain tensor is that it is not objective, meaning that a rigid body rotation generates spurious strain components, which is physically incorrect (Belytschko et al., 2014). Rather, these formulations employ finite strain measures that incorporate non-linear terms to properly account for large rotations and deformations. The Total Lagrangian approach typically uses the Green-Lagrange strain tensor (referred to the initial configuration), while the Updated Lagrangian approach uses strain measures referred to the current configuration, such as the Almansi strain or rate of deformation (Bathe, 1996).

The Total Lagrangian approach refers to a reference configuration that remains fixed throughout the analysis, while the Updated Lagrangian approach updates the reference configuration at each time step to the current deformed state. The Updated Lagrangian approach has the advantage that the Cauchy stress tensor appears explicitly in the linearized equations of equilibrium, which means that standard constitutive models can be employed (Augarde et al., 2021).

In the context of the Updated Lagrangian approach, the quality of the mesh elements may be significantly impacted. Indeed, the large deformations lead to the distortion and deterioration of the mesh, quantified

(e.g) by the aspect ratio (maximum edge length to minimum edge length) or maximum and minimum angles of each element. This deterioration can lead to numerical inaccuracies or simply convergence issues.

To overcome mesh distortion, kinematic descriptions such as the arbitrary Lagrangian-Eulerian (ALE) method (Ghosh and Kikuchi, 1991; Van den Berg et al., 1996) were developed. The mesh nodes can move in a complete Lagrangian fashion or remain fixed in an Eulerian fashion, or move according to an arbitrary velocity field designed to minimize element distortion (Donea et al., 2004). When the mesh becomes too distorted, a smoothing or remapping procedure is triggered from the old mesh to a new one, both sharing the same boundaries. The solution variables must then be advected from the old mesh to the new one. This remapping procedure must be carefully performed to ensure conservation of physical quantities and to limit numerical diffusion. The tracking of the boundaries can be complex in this framework, requiring a relatively high amount of work (Augarde et al., 2021). Moreover, tracking a free surface using the ALE technique can be challenging. It requires knowing the position of the last computed free surface, update it and reproject it on the new mesh.

A method very similar to ALE is the Coupled Eulerian Lagrangian (CEL) method. This method was developed to tackle the interactions between two materials, such as in a pipeline burial process. In this method, a soft material (the soil) is modelled in an Eulerian framework, while the structure (the pipeline, e.g.) is modelled in a Lagrangian framework (Augarde et al., 2021). This method is not directly applicable (and is not designed to) to the dike breaching problem, or more generally to landslides.

Among the famous methods described in the literature to handle landslides, the Material Point Method (MPM), stands for one of the most popular (Sulsky et al., 1994; Soga et al., 2016). In this particle-based method, a static background mesh is used to solve the governing equations. The material points are in fact scattered in the domain and carry the state variables. Before the FEM computation, the information is projected into the background mesh nodes, and the result is used to move the materials points. The nodes of the background mesh are not moving, which avoids mesh distortion. However, this method requires prior knowledge of the maximum extent of the problem in order to define

the background mesh. This can be problematic when trying to determine the maximum extent of a landslide. Another issue is related to the accumulation of error related to the mapping and remapping of state variables, from material points to mesh nodes and vice-versa. Other issues related to the use of MPM are synthetized again by Augarde et al. (2021)

Smooth Particle Hydrodynamics (SPH) is another technique developed to handle large displacements. Significant contributions in the field of geomechanics were made by Bui et al. (2008, 2011). Here, the discretization is based on the particles and the strong form of the physics is solved. Augarde et al. (2021) report two key difficulties in case of solid modelling: the first one is related to the imposition of boundary conditions, which is not straightforward, and the second one is related to tensile instabilities. Moreover, the method requires a neighbor search algorithm to identify the neighboring particles, which can be computationally expensive.

The remeshing and interpolation technique with small strain (RITSS) method was proposed by Hu and Randolph (1998). The concept is very similar to ALE where frequent remeshing are performed. However, in this method, a classical small strain formulation is used. Which implies that frequent remeshing is required to ensure the accuracy of the results. Since the remeshing is very frequent, the geometrical non-linear terms are negligible between two remeshing operations, even tough the formulation remains non objective. The method proved to be effective for large displacements problems such as footing problems or T-bar penetration (Tian et al., 2014). The method suffers from the same type of limitations than ALE when looking at the tracking of free surfaces, that is required for landslide simulations.

In this chapter, we will focus on the Particle Finite Element Method (PFEM). This Lagrangian method was initially proposed for fluid simulations involving free surfaces and strong topological changes (Oñate et al., 2004; Idelsohn et al., 2004). The basic idea is again that it is possible to overcome mesh distortion issues by using a fast and efficient remeshing algorithm (Cremonesi et al., 2020) and to track all the particles in a Lagrangian manner. PFEM is intended to combine the advantages of mesh-based methods with the possibilities of particle-based methods.

In this context, the particles actually correspond to the nodes of

a mesh. Each of the particles transports its own state variables and momentum. Then, to manage the large deformations, the particles are advected using the obtained displacement field.

To avoid excessive mesh distortions, the mesh is frequently reconstructed from a Delaunay triangulation of the particles and used in the subsequent time steps. Specific techniques are employed to detect wrongly shaped elements and improve the mesh quality. This also requires techniques to capture the boundaries during the remeshing which can be done using the alpha-shape algorithm (Edelsbrunner and Mücke, 1999; Leyssens et al., 2024), as detailed in the next sections.

The advantage of the PFEM algorithm is that it is independent of the physics of the problem. As long as a displacement solution is found by a FEM solver, it can be applied. So the method is non-intrusive and can be coupled with any existing FEM code. It can be applied undifferently to solid mechanics, fluid mechanics or multiphysics problems.

In the computational geomechanics field, it has recently gained interest for simulations of strip footings and insertion problems (Monforte et al., 2017, 2019; Carbonell et al., 2022). Slope failures and landslides have also been investigated using PFEM (Zhang et al., 2015; Yuan et al., 2020). Interesting cases of retrogressive landslides have been simulated by Zhang et al. (2023). They employed the infinitesimal strain theory, claiming that the frequent remeshing limits the error linked to non-linear geometrical effects. They also admit that finite strain formulations are more accurate in case of hyperelastic materials that can sustain large rotationnal effects [1]. In this chapter we will first present, in Section 5.2, the PFEM algorithm in detail, discussing the different steps of the method. Then, Section 5.3 will present geomechanical applications of the PFEM algorithm in the Cauchy mechanics framework. Granular column collapse and slope stability problems will be investigated to demonstrate the capabilities of the method. The issue of mesh dependence that arise for strain-softening materials will be discussed. Section 5.4 will explore the use of Cosserat mechanics to mitigate mesh dependence issues.

[1] We can also argue that the amount of error usually linked to geomechanical properties measurements is probably much higher than the error induced by small strain assumptions in most geomechanical problems.

5.2 The Particle Finite Element Method

Let us consider a set of points S at positions $\{\boldsymbol{x}_i\}$, $i = 1, ..., N$ in a two-dimensional space represented in Figure 5.1a. From the perspective of a dike engineer or an attentive reader of this manuscript, this point cloud could be seen as a very simple representation of a dike. Indeed, linking the external points of the cloud would lead to a rough approximation of a trapezoidal dike cross-section. The question we address here is the following: what type of algorithm can be employed to identify the shape of an evolving material domain based only on a point cloud? In the context of dike breaching, the aim it to detect the shape of the dike as it fails and deform as it in turns influences the other physical processes (free surface flow, erosion, subsurfaceflow).

Before starting describing the PFEM methodology, we will recall a few fundamental definitions that will be used hereunder.

The convex hull of a point cloud

The convex hull of a point cloud can be described, in very simple terms, as the shape obtained by stretching a rubber band around the point cloud. Figure 5.1b illustrates the convex hull of the point cloud. The convex hull is designated by Leyssens (2025) as the most simple shape that contains all the points of the set S.



(a) (b)

Figure 5.1: (a) A point cloud in a two-dimensional space. (b) The convex hull of the considered point cloud represented by the dashed lines.

By definition, a Delaunay triangulation $DT(S)$ of the point cloud divides the convex hull into triangles whose circumcircles do not contain any other point. Figure 5.2 presents the Delaunay triangulation of the

point cloud while Figure 5.3 illustrates the circumcircles of each triangle of this triangulation.

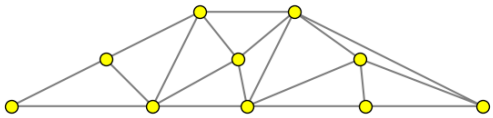


Figure 5.2: Delaunay triangulation $DT(S)$ of the point cloud.

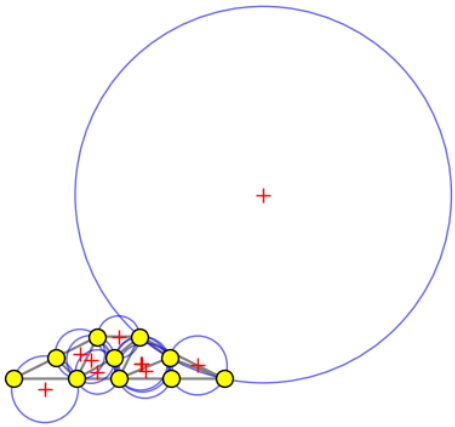


Figure 5.3: The circumcircles of the Delaunay triangulation.

The α-shape algorithm

The α-shape is a shape detection method, first presented by Edelsbrunner et al. (1983), that aims to accurately capture the geometry of a physical domain based only on a point cloud. The parameter α designates the radius of a circle that moves across the point cloud. If the circle of radius α contains no point of the cloud, then the area contained by the circle is

not considered as part of the shape. The α-hull of the point cloud S is the region that does not intersect any empty circle of radius α (Leyssens, 2025). The α-shape has the same topology as the α-hull, but the circles of radius α are replaced by straight lines (See Figure 5.4).

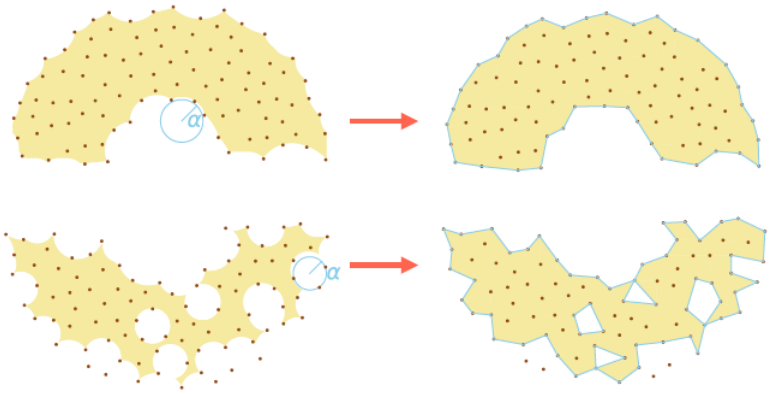


Figure 5.4: Left: the α-hull of a point cloud. Right: the α-shape of the same point cloud. It is observed that different values of α lead to different shapes. The figure is retrieved from Leyssens (2025).

Considering the specific property of the Delaunay triangulation that the circumcircle of each triangle contains no other point of the cloud than the three defining the triangle, we can apply a very efficient algorithm to identify the α-shape of S based on the Delaunay triangulation of the point cloud.

The criterion is based on the ratio between the circumcircle of each element in the mesh and a typical radius of length α, which corresponds to the desired element size at a point with coordinates $\boldsymbol{x}$. The ratio α_e is therefore defined as follows, for an element e of the mesh:

$$\alpha_e = \frac{R_e}{\alpha(\boldsymbol{x}_e)} \tag{5.1}$$

where R_e is the circumcircle radius of element e and $\alpha(\boldsymbol{x}_e)$ the desired typical length at the circumcenter $\boldsymbol{x}_e$ of element e. The method refines the convex hull by removing elements that do not satisfy the criterion.

Let us consider the point cloud S presented in Figure 5.1a and its Delaunay triangulation $DT(S)$ presented in Figure 5.2. Applying the

α-shape algorithm to this configuration allows us to identify the actual shape of the domain represented in green in Figure 5.5. The wrongly shaped element issued from the convex hull is removed and identified in red.

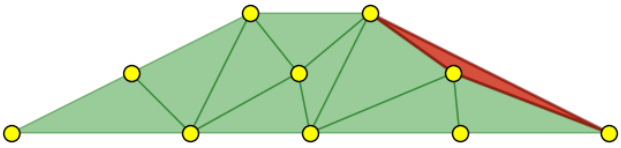


Figure 5.5: Applying the α-shape algorithm to the Delaunay triangulation of a point cloud allows to identify the shape of the material and to eliminate non-physical elements (here colored in red).

If $\alpha_e = 0$ is selected, the α-shape results in the set of points; if $\alpha_e \to \infty$, the α-shape results in the convex hull of the point cloud. Selecting the value of α_e is therefore critical to accurately capture the shape of the material. In general, a value of α_e higher than 1 is required to avoid holes in the shape and a value of 1.2 can typically be used.

Note the following important strength of the algorithm: the alpha-shape algorithm relies on Delaunay triangulation, meaning that identifying the shape of the material is not a complex or time-consuming task since triangulation is already performed.

PFEM working framework

In this section we present how the Particle Finite Element Method was applied in the context of this work for geomechanical applications. Previous works by Leyssens et al. (2024) focused on the use of the same PFEM methodology for fluid mechanics applications. The general framework of the PFEM algorithm remains the same and is presented in

Figure 5.6 considering a granular column collapse situation.

Initially, a point cloud representing the physical domain is considered. In our specific case, this is the representation of the granular column.

The first step consists in finding the initial material shape based on the point cloud. As underlined by Leyssens (2025), this step is complex in the sense that the physical domain may be something subjective.

To obtain this first shape, the point cloud is triangulated using the Delaunay algorithm of GMSH (Geuzaine and Remacle, 2009). A first consequence of this seamless triangulation is visible in the first step of Figure 5.6 where long elements are generated on the sides of the point cloud. Indeed, since the Delaunay triangulation results, by definition, in the convex hull of a point cloud, we must filter out the triangles that are not actually physical.

This filtering is achieved by removing elements that are wrongly shaped or whose sizes are too large applying the α-shape algorithm in step 2.

In this formulation, $\alpha(\boldsymbol{x})$ may take a constant value based on the imposed mesh size, or it can be a field, varying throughout the domain and over the course of the simulation. Every element of the mesh that has a ratio α_e that exceeds a threshold value (typically set to 1.2) is removed from the mesh.

When the full physical domain is detected, we are able to identify the boundaries of the domain. In this work, we make use of a background mesh that represents the maximal geometrical extent of the problem. Boundary edges detected as part of this maximal geometrical extent are considered as physical boundaries, and the rest of these boundary edges are considered as the free surface of the problem.

This allows for a natural treatment of wall boundary conditions, since it suffices to identify which edges of the physical domain belong to a wall. For these edges and their points, proper boundary conditions can then be applied in the finite element formulation. Figure 5.7 illustrates the approach.

In step 4, the physical problem is solved using a method adapted to the problem, which will result in updated state variables and displacements of the nodes. This is the strength of the remeshing algorithm, that we present here as PFEM. As long as a displacement can be computed at each node of the problem, the algorithm can be employed.

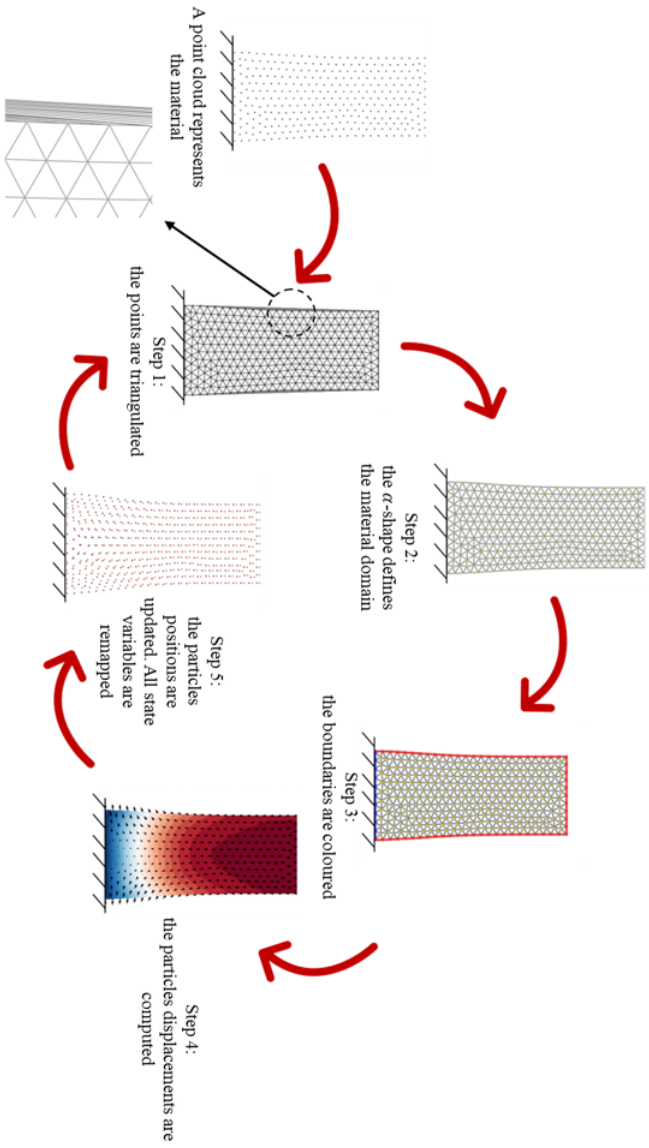


Figure 5.6: The functioning of the PFEM algorithm.

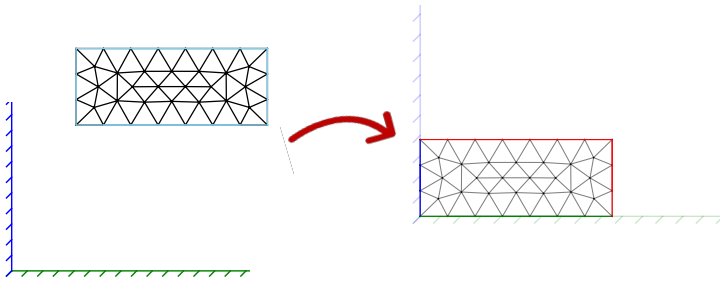


Figure 5.7: The boundaries are managed in two steps: first, the α-shape returns the bounding edges of the physical domain. Next, each edge is coloured according to the walls defined in the background mesh.

In step 5, the position of all the nodes is updated. An important step is the reinitialization of the state variables, such as stresses and strains. Here, we transport this information not only at the mesh nodes, but also at the quadrature points of the mesh, where the solution is computed. A nearest point algorithm is employed to remap the variables from one mesh to the other. Since the amount of points transporting the solution is significant, the numerical error that could arise from this nearest point remapping instead of linear interpolation is rather small. Finally, the entire process is repeated up to the desired final simulation time, with the quality of the mesh maintained throughout.

5.3 Application in the classical Cauchy mechanics framework

A Cauchy medium occupying a volume Ω and bounded by a surface $\partial\Omega$ possesses three translational degrees of freedom, denoted $\boldsymbol{u}$, at each material point.

The stress tensor $\boldsymbol{\sigma}$ is a symmetric tensor with 6 independent stress components that describe the stress state in the domain and that can be written in a compact way, in a vector form as:

$$\boldsymbol{\sigma}^{\mathrm{T}} = (\sigma_{xx}, \sigma_{yy}, \sigma_{zz}, \sigma_{xy}, \sigma_{yz}, \sigma_{zx}) \tag{5.2}$$

Similarly, we introduce the strain tensor $\boldsymbol{\epsilon}$ as a symmetric tensor with 6 independent components directly linked to the displacements $\boldsymbol{u}$

through the small strain assumption:

$$\boldsymbol{\epsilon} = \frac{1}{2}(\nabla \boldsymbol{u} + \nabla \boldsymbol{u}^T) \tag{5.3}$$

That can be similarly written, in Voigt notation, as:

$$\boldsymbol{\epsilon}^{\mathrm{T}} = (\epsilon_{xx}, \epsilon_{yy}, \epsilon_{zz}, 2\,\epsilon_{xy}, 2\,\epsilon_{yz}, 2\,\epsilon_{zx}) \tag{5.4}$$

Considering a purely elastic constitutive law for the medium, the following relation holds:

$$\boldsymbol{\sigma} = \boldsymbol{D}^e : \boldsymbol{\epsilon} \tag{5.5}$$

where $\boldsymbol{D}^e$ is the elastic stiffness tensor that is defined as follows, considering the Young's modulus and the Poisson's ratio for the elastic properties:

$$\mathbf{D}^{\mathrm{e}} = \frac{E}{(1+v)(1-2v)} \begin{bmatrix} 1-v & v & v & 0 & 0 & 0 \\ v & 1-v & v & 0 & 0 & 0 \\ v & v & 1-v & 0 & 0 & 0 \\ 0 & 0 & 0 & \frac{1-2v}{2} & 0 & 0 \\ 0 & 0 & 0 & 0 & \frac{1-2v}{2} & 0 \\ 0 & 0 & 0 & 0 & 0 & \frac{1-2v}{2} \end{bmatrix} \tag{5.6}$$

The Cauchy momentum balance equation is now introduced to describe in a general way the displacement of a body:

$$\nabla \cdot \boldsymbol{\sigma} + \mathbf{f} = \rho \frac{\partial^2 \boldsymbol{u}}{\partial t^2} \tag{5.7}$$

where $\mathbf{f}$ is the body force vector and ρ the density of the material. The system is closed by boundary conditions on the domain surface $\partial\Omega$:

$$\begin{aligned} \boldsymbol{\sigma} \cdot \boldsymbol{n} &= \boldsymbol{t} \text{ on } \partial\Omega_N, \\ \boldsymbol{u} &= \boldsymbol{u}_{imposed} \text{ on } \partial\Omega_D, \end{aligned} \tag{5.8}$$

that consist in prescribed forces $\boldsymbol{t}$ on the Neumann boundary $\partial\Omega_N$ and prescribed displacements $\boldsymbol{u}_{imposed}$ on the Dirichlet boundary $\partial\Omega_D$. The system is then integrated by means of the Finite Element Method, where a weak form must first be derived on the basis of the virtual displacement principle. Here, a pure small-strains incremental displacement-based

formulation is employed, that is the one implemented in the Moose framework, Solid Mechanics module (Adhikary et al., 2016; Wilkins et al., 2019). This means that the increment in stress $\Delta\boldsymbol{\sigma}$ is a function of the incremental displacement $\Delta\boldsymbol{u}$:

$$\Delta\boldsymbol{\sigma} = \Delta\boldsymbol{\sigma}(\Delta\boldsymbol{\epsilon}(\Delta\boldsymbol{u})) \tag{5.9}$$

Following e.g. de Borst et al. (2012), a mass matrix $\boldsymbol{M}$ and stiffness matrix $\boldsymbol{K}_0$ are built for the initial time step. A linear system of equations obtained from the weak form is solved for the incremental displacement vector $\boldsymbol{\Delta u}$:

$$\boldsymbol{M}\ddot{\boldsymbol{u}}^{t+\boldsymbol{\Delta t}} + \boldsymbol{C}\dot{\boldsymbol{u}}^{t+\boldsymbol{\Delta t}} + \boldsymbol{K_0}\Delta\boldsymbol{u} = \boldsymbol{F}_{\boldsymbol{ext}}^{\boldsymbol{t+\Delta t}} - \boldsymbol{F}_{\boldsymbol{int,0}}^{\boldsymbol{t}} \tag{5.10}$$

where $\boldsymbol{F_{ext}}$ vector corresponds to the external forces acting on the nodes and $\boldsymbol{F_{int}}$ vector corresponds to the internal forces. Both vectors are computed by integration on the elements of the domain. $\boldsymbol{C}$ is the damping matrix that is computed as a linear combination of the mass and stiffness matrices (de Borst et al., 2012):

$$\boldsymbol{C} = \eta\boldsymbol{M} + \zeta\boldsymbol{K_0}, \tag{5.11}$$

where η and ζ are the Rayleigh damping coefficients. The damping of the system depends on these two coefficients. The damping ratio $\xi(\omega)$ at a frequency ω of the system is computed as follows:

$$\xi(\omega) = \frac{\eta}{2\omega} + \frac{\zeta}{2}\omega \tag{5.12}$$

An implicit Newmark scheme is employed for the time integration.

From the computed solution $\Delta\boldsymbol{u}$, the strain increment $\Delta\boldsymbol{\epsilon}$ is computed, from where the stress state can finally be computed using Equation 5.5 in a purely elastic model. In this work, we make use of elasto-plastic laws to describe geomaterials, that usually exhibit strongly non-linear behaviors.

In case of an elasto-plastic behavior, the strains are usually decomposed into two parts, namely the elastic and the plastic part:

$$\boldsymbol{\epsilon} = \boldsymbol{\epsilon}^e + \boldsymbol{\epsilon}^p \tag{5.13}$$

Yield functions are usually employed to distinguish between elastic and plastic domain and are written as functions of the stress state $f(\boldsymbol{\sigma})$.

These functions are bounding the admissible domain and must respect the following inequality:

$$f(\boldsymbol{\sigma}) \leq 0 \tag{5.14}$$

Well-known yield functions, presented in de Borst et al. (2012), are, for example, von Mises, the Mohr-Coulomb or the Drucker Prager criteria. Plastic strain occurs when $f(\boldsymbol{\sigma}) = 0$, but $f(\boldsymbol{\sigma})$ can never leave the admissible domain, meaning that $f(\boldsymbol{\sigma}) > 0$ is impossible.

Within the elastic domain, Equation 5.5 remains valid, such that the yield condition satisfies $f(\boldsymbol{\sigma}) < 0$. This relation is evaluated in what is referred to as the trial step of the numerical algorithm. When the trial state leads to a positive value of the yield function, plastic yielding is detected and an algorithm called return-map is employed (Adhikary et al., 2016; Wilkins et al., 2019). The return-mapping procedure employs a Newton–Raphson iterative scheme to compute an admissible stress state that satisfies the constitutive constraints of the material model. Beyond of the stress state, the return map algorithm also computes plastic multipliers that reflect, when summed, the accumulation of plastic strain that will be designated as *equivalent plastic strain*, $\bar{\epsilon}^p$, in this work. In case of strain softening or hardening, these multipliers are used to update the yield function parameters.

5.3.1 Perfectly plastic slope failure

Failure of earthen slopes is a classical problem for geomechanical engineers. Safety factor analysis is the usual way of defining the slope stability by making use of the shear strength reduction method as presented in Chapter 4. Nevertheless in order to describe the dike failure during an overtopping event, we need to model the failure process after the initiation of the rupture using a PFEM algorithm.

Let us consider the slope failure represented in Figure 5.8 computed by the means of the shear strength reduction method with no remeshing. The geomaterial is considered to follow a perfectly elasto-plastic behaviour, defined by a Mohr-Coulomb yield function.

A Young's modulus E of 20 MPa and a Poisson's modulus ν of 0.3 are considered for the elastic properties. An initial cohesion c of 20 kPa and a friction angle ϕ of 25° with a dilatancy angle ψ of 25° are considered for the Mohr-Coulomb yield function. The density of the soil is set to

1937 kg/m^3. The safety factor was found to be equal to 2.05 for this slope configuration. The figure depicts the equivalent plastic strain for a strength reduction factor just below the critical one, $\overline{\epsilon}^p$, that represent the accumulation of plastic strain. The shear band is clearly visible but the computation stops at the following strength reduction factor.

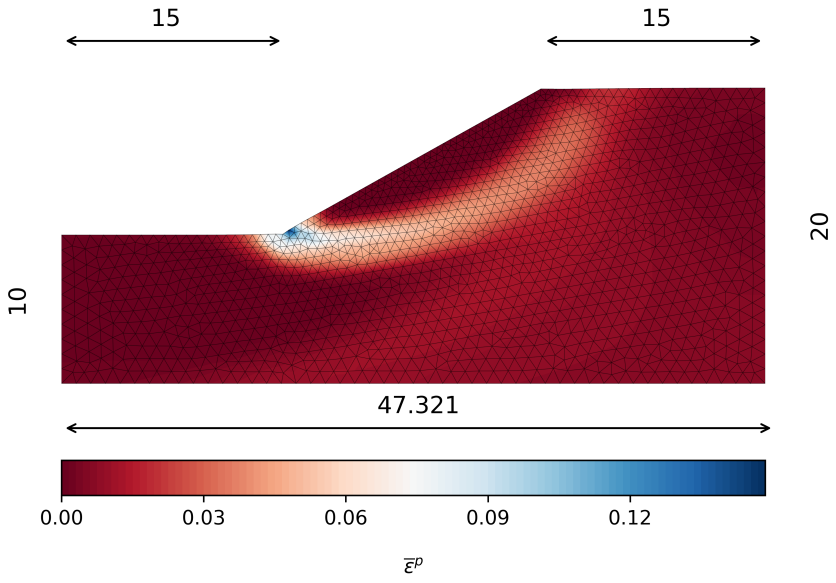


Figure 5.8: State of the slope at the end of the shear strength reduction method analysis.

Now that the safety factor of the slope is known, we can perform a PFEM calculation the full runout of the failure. With this calculation the soil is expected to move and deform along the shear band. The mechanical properties of the soil (cohesion, friction angle) are computed on basis of the safety factor found previously in order to have an initially unstable slope. The initial geometry of the failure is the same than for the shear strength reduction method analysis. The remeshing is performed every 0.01 s. It is not always necessary to remesh so frequently for the convergence, but it allows to keep a well-organized mesh all along the simulation. The choice of the time step is flexible and should be based

on the kinetics of the problem. However, Moose has an algorithm that divides the time step in half when convergence is not achieved for a given time step. This is an asset as it enables a relatively large time step to be used initially, allowing the algorithm to adapt it if necessary. During critical phases of failure, such as initial propagation, the time step is usually smaller than the initial one. As the failure propagates, the time step tends to increase again. Moreover, the computational cost of the non-linear algorithms for plasticity is much higher than that of remeshing, providing additional motivation for frequent remeshing as a well-conditioned mesh allows a faster convergence of the nonlinear problem. The state of the failed slope after 4.5 seconds is visible in Figure 5.9, where the accumulated volumetric change is depicted.

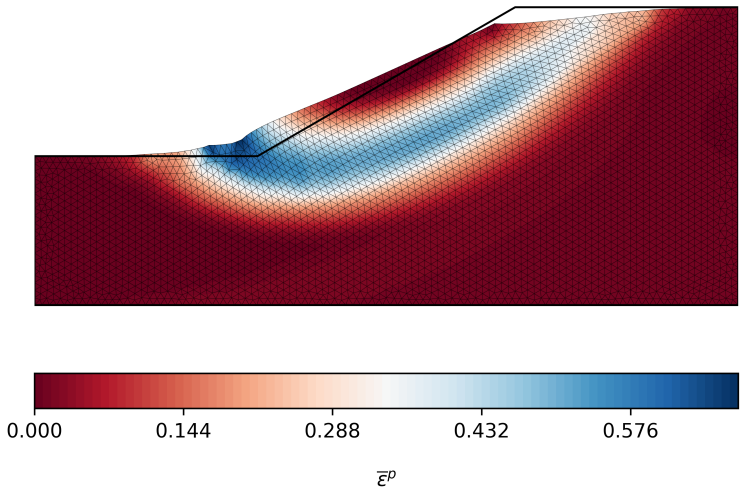


Figure 5.9: The final deformed slope after PFEM analysis.

Here, we observe no detachment of material along the shear band and the progression of the failure has already stopped. This is due to the perfect plastic behaviour of the material. Mass detachments are

generated by softening behaviour of the shear strength along the shear band, that will be incorporated in further examples.

5.3.2 Granular column collapse

Granular column collapse is a common tackled problem in fluid mechanics and in the landslide prediction field. Many phenomena can be simplified as the collapse of granular material: avalanches, submarine landslides, debris or mudflows. In this example, we will study the capacity of the PFEM algorithm to simulate such highly dynamic phenomena undergoing very large deformations. We will consider the collapse of a granular column under its own weight. Two distinct constitutive models and shapes will be employed for the collapsing material to show the influence of these choices on the collapse dynamics. First, a purely cohesive material will be considered to represent what could be associated to a mudflow. Second, a purely frictional material will be considered to represent a dry granular collapse.

Cohesive granular column collapse
A 60-cm high granular column is placed on a layer of soil of the same nature, whose initial geometry is depicted in Figure 5.10.

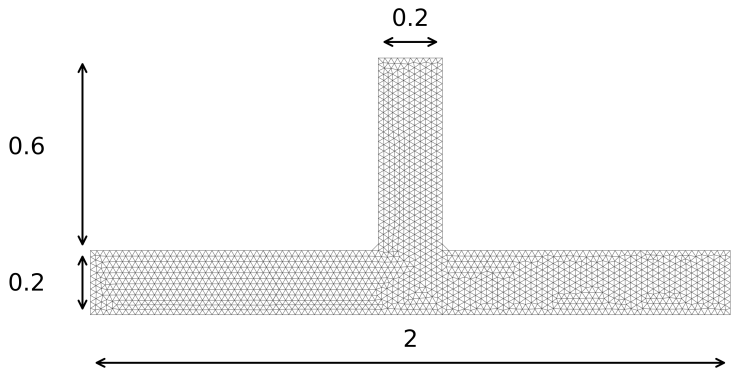


Figure 5.10: Initial geometry of the cohesive granular column collapse, lengths are in meters.

The simulation consists of the natural collapse of the material, sub-

jected to its own weight. Here, a Young's modulus E of 1 MPa and a Poisson's ratio ν of 0.4 are selected for the elastic properties. The column is made of a cohesive material with a 1.5 kPa cohesion representative of mud. A time step of 0.005 s is selected for the simulation, and remeshing is performed at each time step. The choice of the time step results mainly from the problem kinetics. Here, a small time step is required to capture the dynamics of the collapse.

In the first steps of the collapse, the column collapses vertically. Then, the material flows laterally which is expected from a mud-like material. Figure 5.11 presents the state of the column after 1.25 seconds of collapse. Plastic strain has accumulated at the bottom of the collapse, particularly in the center where the material is being redirected to the left and right sides. Figure 5.12 depicts a zoom around the toe of the collapse and indicates the direction of the deformations, which point to the right and left sides.

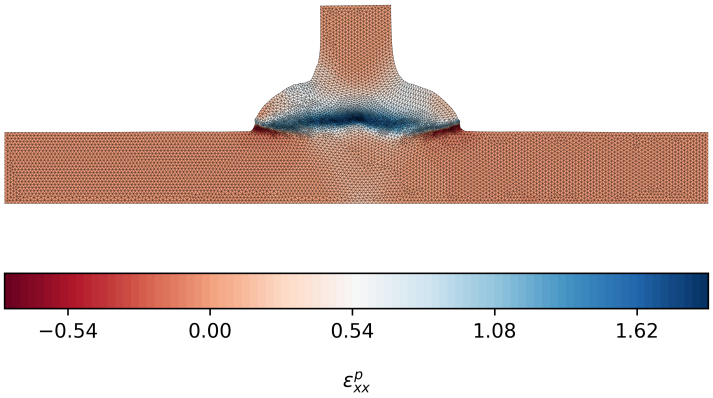


Figure 5.11: Plastic strain distribution in the cohesive column after 1.25 seconds.

Frictional granular column collapse

The initial geometry of the frictional granular column is depicted in Figure 5.13. The problem is very similar to the previous one, where the column is again subjected to its own weight. Nevertheless, the soil is now considered as a frictional material, with a friction angle ϕ of 28.64° and a dilatancy angle ψ of 28.64°. A small cohesion, c of 500 Pa is considered

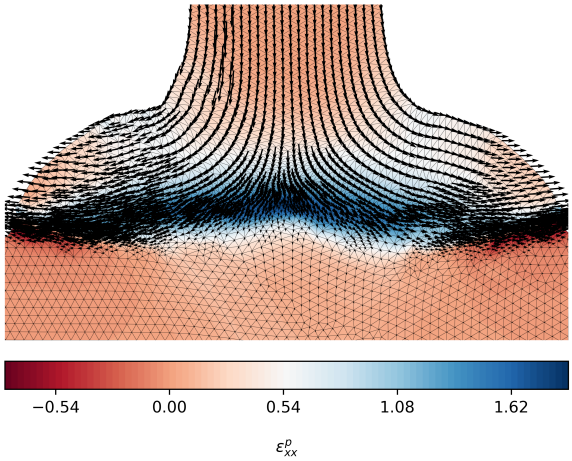


Figure 5.12: Zoomed view of the plastic strain distribution at the toe of the collapse. The arrows indicate the direction of the deformation.

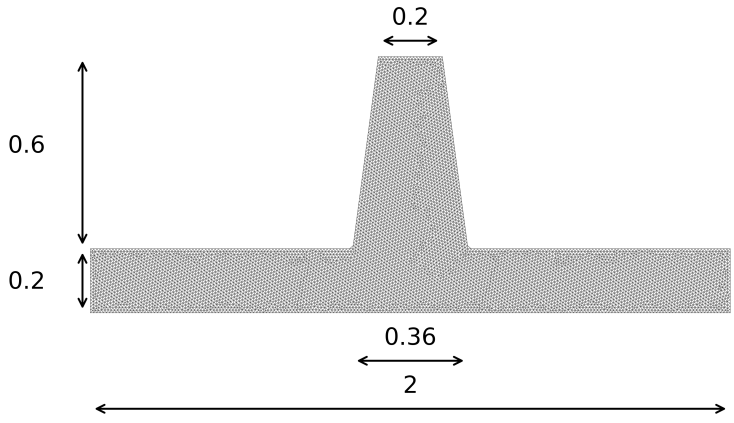


Figure 5.13: Initial geometry of the frictional granular column collapse, lengths are in meters.

to improve the numerical convergence. Without cohesion very small time steps would be required to capture the collapse dynamics. The collapse dynamic appears to be very different from the cohesive case. As shown in Figure 5.14, two shear bands develop on both sides of the column. Figure 5.15 depicts a zoom around the toe of the collapse and indicates the direction of the deformations. It is clear on this figure that the material flows along these bands. The displacements are near to zero in the center of the column, while large deformations occur along the shear bands.

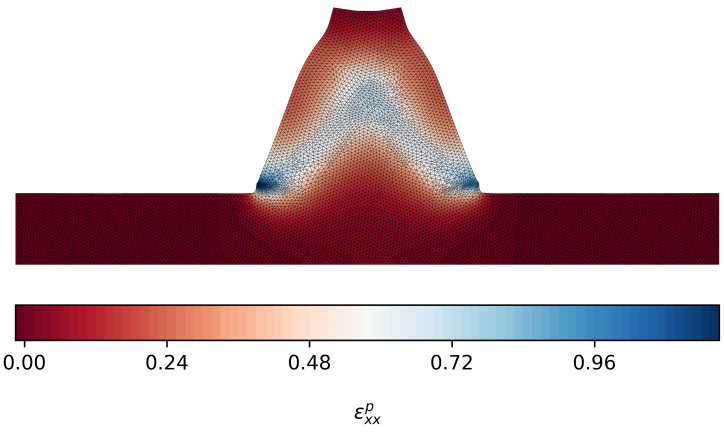


Figure 5.14: Plastic strain distribution in the frictional column after 1.85 seconds.

The examples of granular column collapse demonstrate that the PFEM can reproduce physical phenomena involving large displacements. The two examples also show the impact of the constitutive model on collapse dynamics used to describe the properties of the material. The choice of an appropriate plastic constitutive relationship is of primary importance on failure mechanism of the material. One question that arises is the influence of large strains on the actual mechanical properties of soil, which is probably not well captured by a simple elastoplastic criterion such as the Mohr-Coulomb law.

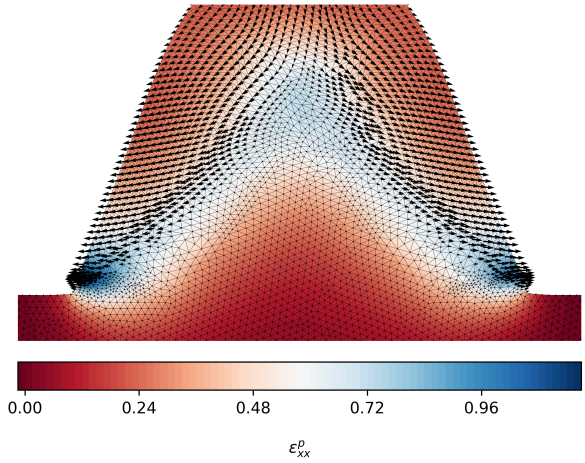


Figure 5.15: Zoomed view of the plastic strain distribution at the toe of the collapse. The arrows indicate the direction of the deformation.

5.3.3 Retroactive slope failures

Retroactive (or retrogressive) landslides are a specific type of landslide in which failure propagates in both directions (forward and backward). Such cases mainly arise in sensitive clays that exhibit important shear strength losses even for small strains. A retroactive landslide is characterised by a first rotational failure that generates the rotational failures of the rest of the slope in a very fast manner in the upwards direction (Kennedy et al., 2021). A final pattern generally arises, where the so-called horst and graben are observed along with long retrogression distances (that corresponds to the distance between the top of the first failure to the remaining stable part of the slope after failure). For example, a landslide occurred in Sainte-Monique, Quebec, Canada, in 1994, and retrogression distances of up to 100 metres have been observed (Locat et al., 2015). Such landslides pose a significant threat to infrastructure and people due to their highly mobile nature. Therefore, numerical models could be used for risk management purposes. However, classical FEM do not allow for large displacements that are required to properly simulate the effects of shear strength losses. It is then likely that a FEM model is not able to

predict nor the initiation nor the backwards propagation of the failure.

Methods that account for large displacements must therefore be employed to capture the runoff and the typical failure pattern. Interest in modelling these events has recently increased. For example, Yuan et al. (2020) managed to reproduce the typical pattern of a retroactive failure using a PFEM formulation, with a linear strain softening model for the cohesion. A similar study was performed by Zhang et al. (2023), in which a 3D PFEM formulation was employed and the sensitive clay was modelled using a linear softening law for cohesion. Note that the general pattern was also captured by MPM models, such as the one presented in Wang et al. (2016).

Here, we present an application of the PFEM model to a retroactive block failure case. The initial geometry is depicted in Figure 5.16.

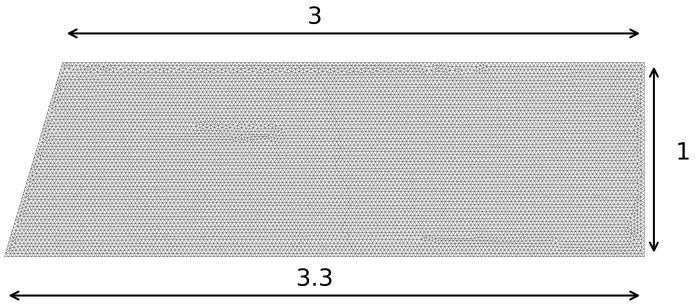


Figure 5.16: Initial geometry of the retrogressive slope failure, lengths are in meters.

The soil is modelled as a sensitive clay, with an exponential softening law on the cohesion such as:

$$c = c_{res} + (c_0 - c_{res}) \cdot e^{-R\bar{\epsilon}^p} \tag{5.15}$$

Where c_0 is the initial cohesion, c_{res} is the residual cohesion, R is the rate and $\bar{\epsilon}^p$ is the equivalent plastic strain.

Here, the initial cohesion, c_0 is set to 5 kPa, the residual cohesion, c_{res} is set to 2.5 kPa and the rate R to 15. A 1 MPa Young's modulus E and a 0.48 Poisson's ratio ν are selected for the elastic properties. The density of the soil is set to 1800 kg/m^3. The simulation is performed with a 0.005 s time step, with the final time being 2.5 s.

Figure 5.17 (a) depicts the initiation of the failure and the localization of the first shear band that appears after 0.25 seconds. It is observed that the failure does not initiate from the toe of the slope, but rather that multiple failures are initiating. From this point, the model shows a very fast retrogressive landslide pattern. New shear bands develop backward as the failure progresses. Strain particularly accumulates in one of these bands, that drives the first rotational failure observed in Figure 5.17 (b). The figures depict the equivalent plastic strain, $\overline{\epsilon}^p$, directly related to the evolution of the cohesion. Along these bands, the cohesion, c, drops significantly. This explains why the blocks are sliding downwards, along these shear bands. Figure 5.17 show the process from 0.25 s to 1 s and Figure 5.18 depict the process from 1.25 s to 2 s.

Influence of the softening law

We already demonstrated the influence of the constitutive model on the collapse dynamics in Section 5.3.2. Here, we investigate the influence of the softening law on the retrogressive failure pattern by comparing the exponential (Equation 5.15) and cubic softening laws. A cubic softening law is now considered for the cohesion, defined as follows:

$$c(\overline{\epsilon}^p) = \begin{cases} c_0, & \overline{\epsilon}^p \leq \overline{\epsilon}^p_0, \\ \alpha(\overline{\epsilon}^p - \overline{\epsilon}^p_0 - \Delta\overline{\epsilon}^p)^3 + \beta(\overline{\epsilon}^p - \overline{\epsilon}^p_0 - \Delta\overline{\epsilon}^p) + \dfrac{c_0 + c_{\text{res}}}{2}, & \overline{\epsilon}^p_0 < \overline{\epsilon}^p < \overline{\epsilon}^p_{\text{lim}}, \\ c_{\text{res}}, & \overline{\epsilon}^p \geq \overline{\epsilon}^p_{\text{lim}}. \end{cases} \tag{5.16}$$

where $\Delta\overline{\epsilon}^p$ and the coefficients α and β are computed as follows:

$$\Delta\overline{\epsilon}^p = \frac{\overline{\epsilon}^p_{\text{lim}} - \overline{\epsilon}^p_0}{2}, \tag{5.17}$$

$$\alpha = \frac{c_0 - c_{\text{res}}}{4(\Delta\overline{\epsilon}^p)^3}, \tag{5.18}$$

$$\beta = -3\,\alpha\,(\Delta\overline{\epsilon}^p)^2. \tag{5.19}$$

Limits of $\overline{\epsilon}^p_0 = 0$ and $\overline{\epsilon}^p_{\text{lim}} = 0.4$ are considered here, i.e. the same initial, c_0, and residual cohesion, c_{res}, than for the exponential case. The two laws are compared in Figure 5.19.

The cubic law appears to be steeper than the exponential one, sharing a similar trend. However, the obtained retrogressive pattern is very

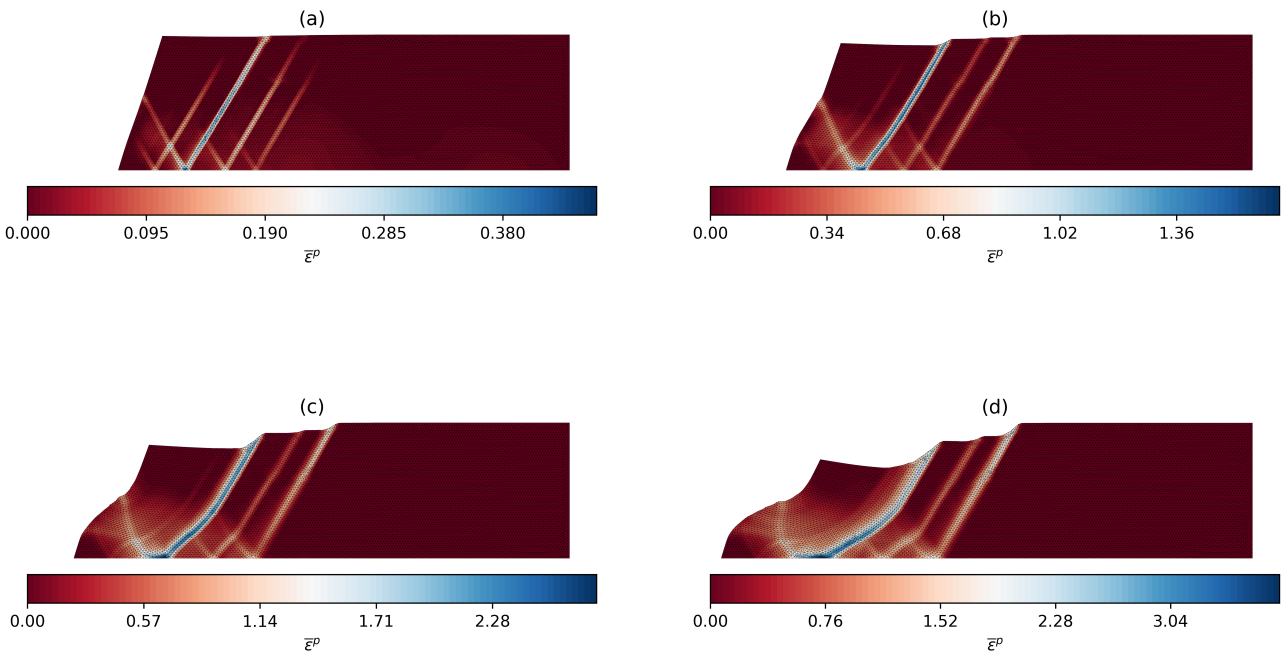


Figure 5.17: The figure depicts the equivalent plastic strain ($\overline{\epsilon}^p$) at different time steps. (a) after 0.25 seconds, (b) after 0.5 seconds, (c) after 0.75 seconds, (d) after 1 second.

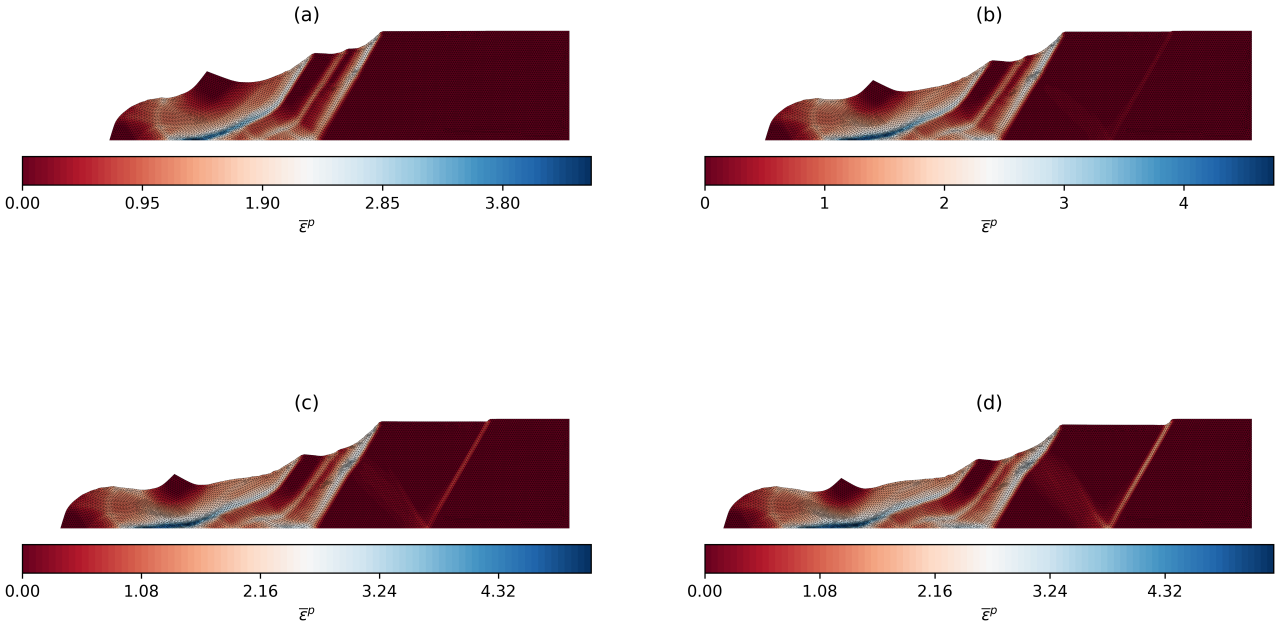


Figure 5.18: The figure depicts the equivalent plastic strain ($\overline{\varepsilon}^p$) at different time steps. (a) after 1.25 seconds, (b) after 1.5 seconds, (c) after 1.75 seconds, (d) after 2 seconds.

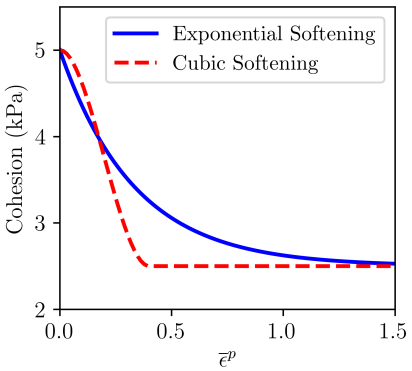


Figure 5.19: Comparison of the exponential and cubic softening laws for the cohesion.

different and the results are depicted in Figure 5.20. First, the volumetric changes appear to be diffuse in the slope (Figure 5.20 (a-b)), while the exponential law generated well-defined shear bands from the beginning of the failure. After 0.75 seconds (Figure 5.20 (c)), a clear shear band appears in the middle of the slope, where a large amount of strain accumulates. Figure 5.20 (d) shows that the sliding has clearly started along this band.

The further evolution of the failure is depicted in Figure 5.21, where the failure appears to be less retrogressive than in the exponential case. The shear band where strain localizes appears much wider than in the exponential case.

It underlines again the influence of the constitutive model on the failure pattern. It shows that the most sensitive part and parameter is the constitutive law that is employed to model the geomaterial.

Mesh-dependence issue

Figure 5.17 (a) shows that the shear band thicknesses tend to localise within a band of one mesh element width. A very well known issue related to strain softening models is the mesh-dependence of the results. The width of the shear bands that are computed strongly depends on the size of the mesh elements. An additional retroactive failure simulation is ran to illustrate this issue. Figure 5.22 shows a result obtained with the

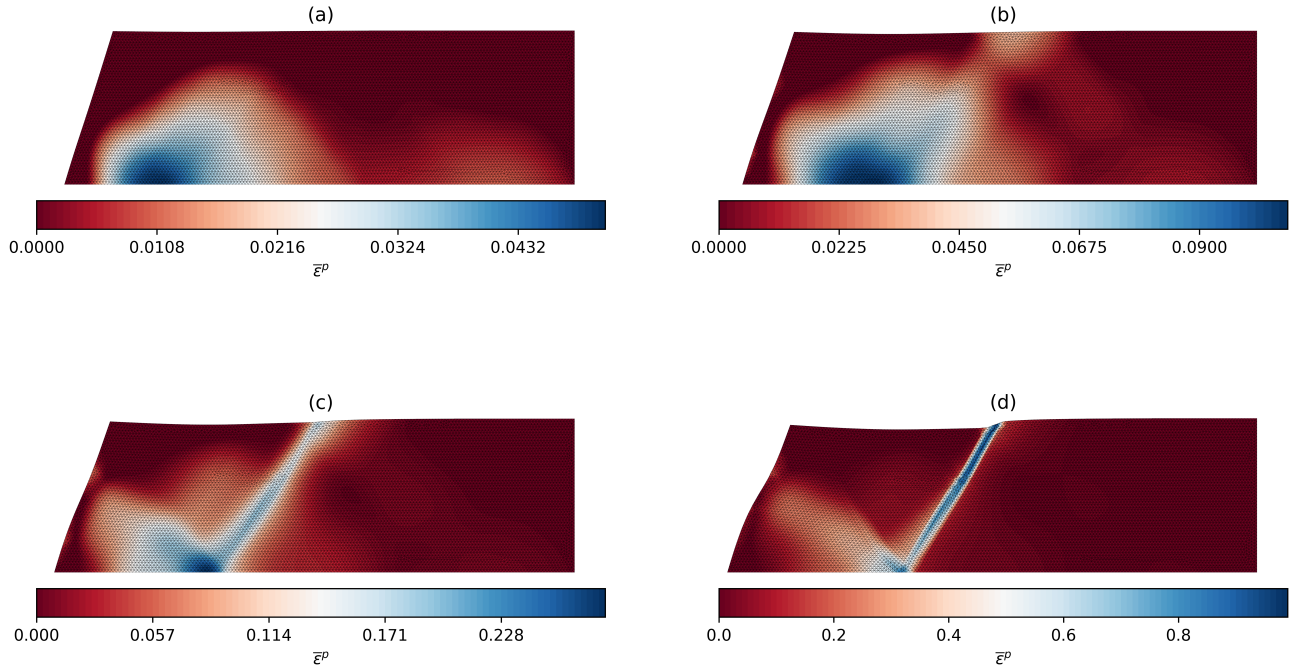


Figure 5.20: The figure depicts the equivalent plastic strain ($\overline{\epsilon}^p$) at different time steps in case of a cubic softening law. (a) after 0.25 seconds, (b) after 0.5 seconds, (c) after 0.75 seconds, (d) after 1 second.

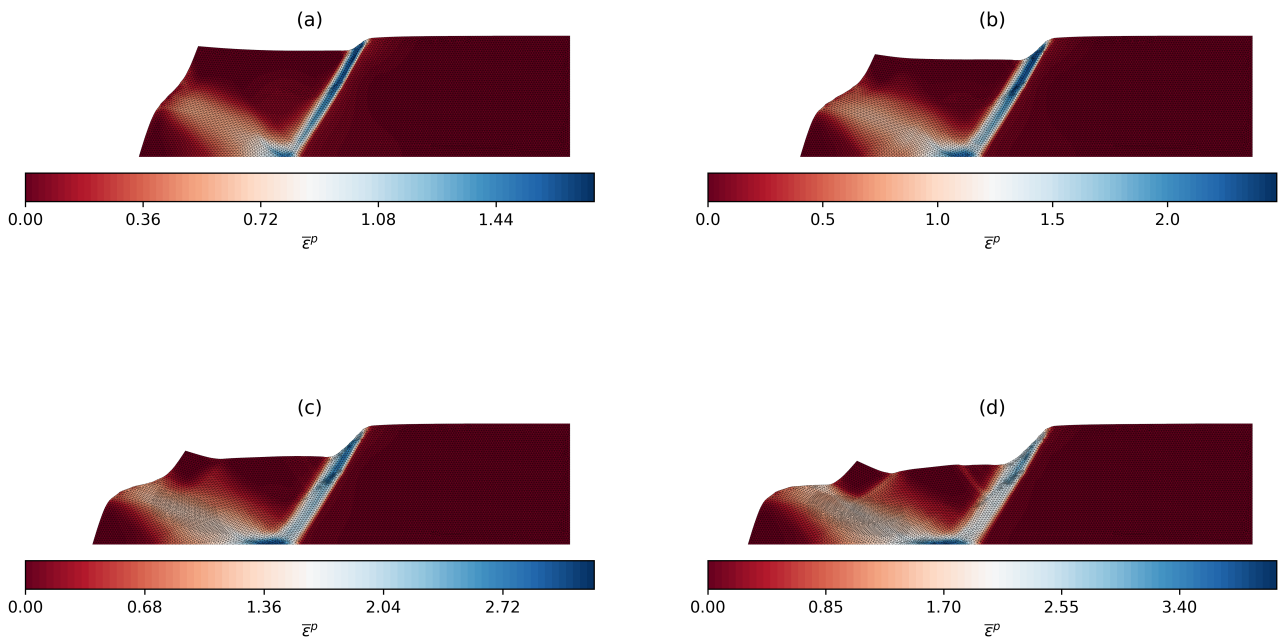


Figure 5.21: The figure depicts the equivalent plastic strain ($\overline{\epsilon}^p$) at different time steps in case of a cubic softening law. (a) after 1.25 seconds, (b) after 1.5 seconds, (c) after 1.75 seconds, (d) after 2 seconds.

same configuration but with a coarser mesh (4 cm of element size).

Localisation of strain is much less pronounced. Strain localises in wider bands, which are led by the mesh size. In fact, two bands appear in this case, while only one band was observed during the initiation of the finer mesh retroactive collapse.

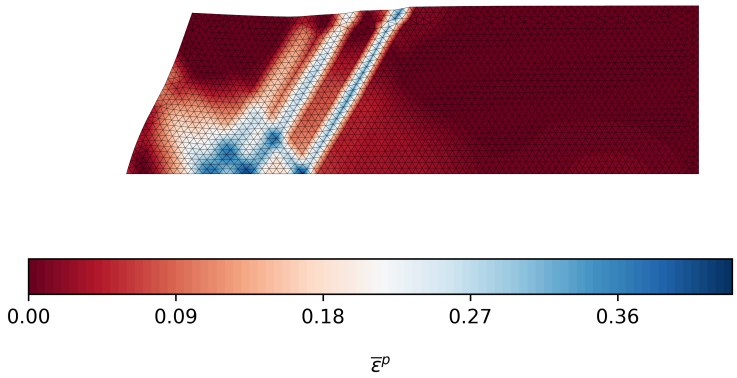


Figure 5.22: The figure depicts the equivalent plastic strain ($\overline{\epsilon}^p$) at 0.25 seconds with a coarser mesh. Two distinct shear bands clearly appear.

The results are clearly affected by the mesh size, which is a very unwanted feature for the developed model (yet expected). An ideal model should provide mesh-independent results, meaning that the shear band thickness should not depend on the mesh size, at least for a certain level of refinement, but on a physical length scale.

5.3.4 Biaxial testing to underline strain softening?

This section presents a simple biaxial test to highlight the strain softening model and to underline the mesh-dependence. A rectangular sample of soil of 0.175 m high and 0.1 m wide is considered. The boundary conditions are depicted in Figure 5.23. The top of the sample is subjected to an vertical displacement of velocity $0.001m/s$, while the bottom of the column is fully fixed. A notch is placed at $y = 0.06m$ in the mesh to provoke the initiation of the shear band at this location.

The soil is modelled as a cohesive massless material with a linear softening law described at Equation 5.20:

$$c(\bar{\epsilon}^p) = \begin{cases} c_0, & \bar{\epsilon}^p \leq \bar{\epsilon}^p_0, \\ c_0 + \dfrac{c_{\text{res}} - c_0}{\bar{\epsilon}^p_{\text{lim}} - \bar{\epsilon}^p_0} \left(\bar{\epsilon}^p - \bar{\epsilon}^p_0\right), & \bar{\epsilon}^p_0 < \bar{\epsilon}^p < \bar{\epsilon}^p_{\text{lim}}, \\ c_{\text{res}}, & \bar{\epsilon}^p \geq \bar{\epsilon}^p_{\text{lim}}. \end{cases} \tag{5.20}$$

The initial cohesion, c_0, is set to 5 kPa, the residual cohesion, c_{res}, to 1 kPa, the residual value is reached as the equivalent plastic strain ε^p reaches 0.1 and the softening starts at $\bar{\epsilon}^p_0 = 0$. The elastic properties consist of a Young's modulus E of 10 MPa and a Poisson's ratio, ν, of 0.2.

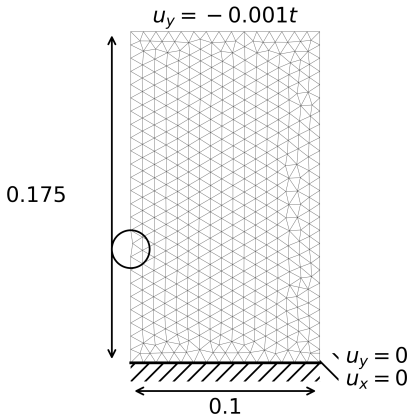


Figure 5.23: Initial geometry of the biaxial test, lengths are in meters. The boundary conditions are represented. The notch is highlighted by a circle.

Three different mesh sizes are considered for the analysis: a fine mesh with an element size of 6 mm, a medium mesh with an element size of 7 mm and a coarse mesh with an element size of 10 mm. The results are depicted for the three meshes in Figure 5.24, where the equivalent plastic strain is represented.

Figure 5.25 shows how the vertical pressure exerted on the top of the sample evolves with the vertical shortening for the three mesh sizes.

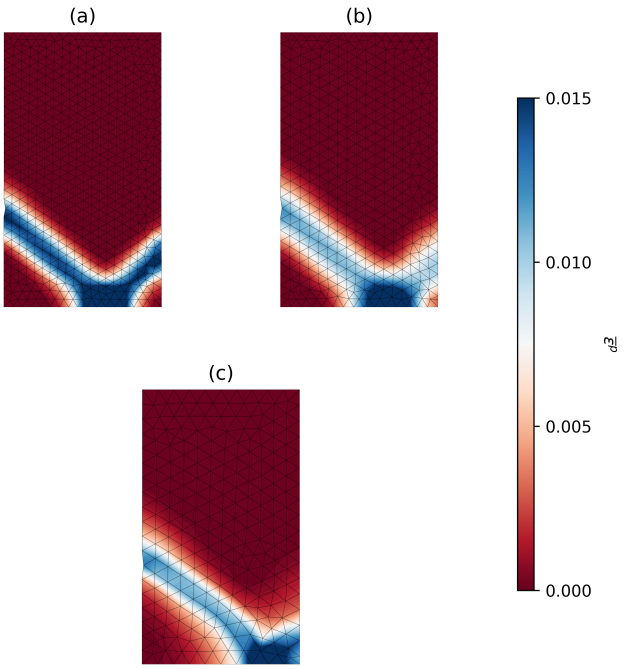


Figure 5.24: The figure shows the equivalent plastic strain for three different mesh sizes after 3.5 seconds: 6 mm (a), 7 mm (b), and 10 mm (c).

The results is the same for the three meshes during the elastic phase of the test. The peak strength of 10 kPa is reached at the same vertical shortening for the three meshes. However, after the peak strength, the results diverge. This is where mesh dependence clearly appears. The finer mesh seems to react in a more steep manner, with a faster softening. In fact, it is the same process than in the previous example of the retroactive slope failure. The smaller mesh leads to higher concentration of strain in the shear band, which leads to a faster drop of the cohesion.

5.4 Cosserat continuum theory to mitigate mesh dependence

Mitigation techniques to reduce mesh dependence
Sheared soils usually exhibit complex elastoplastic behaviour, such as

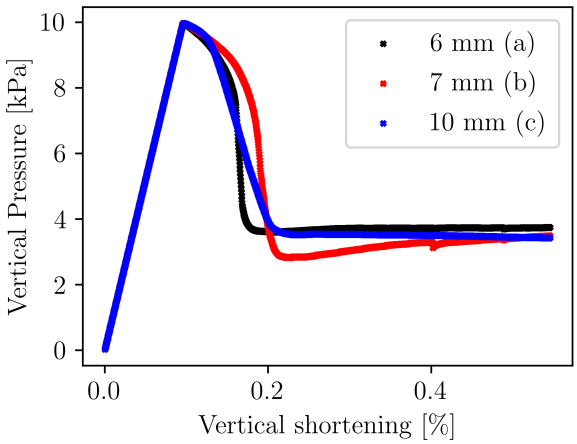


Figure 5.25: Vertical pressure in function of the vertical shortening for the three different mesh sizes: 6 mm, 7 mm, and 10 mm.

softening. Using this behaviour in a classical finite element method formulation typically results in mesh dependency issues, where strain becomes localised within a single element or a single band of elements, as described previously. This issue arises from the loss of convexity of the stress-strain relationship, while perfect plasticity or hardening behaviour generally preserves convexity (Moës and Chevaugeon, 2021). This results in the problem becoming ill-posed according to Vardoulakis (1985) and mesh refinement leading to zero energy dissipation in a non-physical way. To mitigate this mesh dependency, it is required to regularize the problem by introducing a length scale in the formulation. Starting from this observation, several possible techniques have been developed in the literature. Non-local approaches have been employed in PFEM by Monforte et al. (2019). At the end of each converged step, the state variables fields are spatially averaged on a radius that should be physically linked to the characteristic shear band thickness. The implementation of this approach is relatively straightforward and no additional equation has to be solved. Moës and Chevaugeon (2021) proposed to limit the values of the state variable responsible for softening by imposing a Lipschitz regularity. This idea naturally introduces the length scale in the problem but requires a choice from the user. Viscoplasticity is another common

approach to regularize strain localization issues in time, as presented by Wang et al. (1997) and Duretz et al. (2023). The rate dependency of the material introduces a length scale whose effects disappear over time if the time scale of the problem is larger than the relaxation time of the viscous terms (Jacquey et al., 2021). Multiphysics coupling has also been employed to introduce a length scale in the problem and to regularize in space and in time as described by Jacquey et al. (2021).

Cosserat continuum theory

In this work, we propose to use a more physical approach based on the Cosserat continuum theory, where rotational degrees of freedom are also accounted for in the kinematics description of the material countrarywise to the classical Cauchy continuum mechanics. The Cosserat continuum theory is often presented as being more physical for granular materials, such as soils, as the particles composing the material are able to rotate. Strain localisation issues are avoided within this framework, and a mesh convergence is therefore possible as presented in Rattez et al. (2018). A deep presentation of the Cosserat continuum theory is developed by Rattez (2017).

A Cosserat medium occupying a volume Ω and bounded by a surface $\partial\Omega$ possesses six degrees of freedom at each material point: three translational components $\boldsymbol{u}$ and three rotational components $\boldsymbol{\omega}$.

The stress tensor $\boldsymbol{\tau}$ is, in general, non-symmetric and can be decomposed into a symmetric part, denoted as $\boldsymbol{\sigma}$ (associated with the classical Cauchy stress tensor), and a non-symmetric part, denoted as $\boldsymbol{\tau}^{\mathrm{n-sym}}$, which arises from the rotational degrees of freedom:

$$\boldsymbol{\tau} = \boldsymbol{\sigma} + \boldsymbol{\tau}^{\mathrm{n-sym}}, \quad \text{where} \quad \boldsymbol{\sigma} = \frac{1}{2}(\boldsymbol{\tau} + \boldsymbol{\tau}^{\mathsf{T}}), \quad \boldsymbol{\tau}^{\mathrm{n-sym}} = \frac{1}{2}(\boldsymbol{\tau} - \boldsymbol{\tau}^{\mathsf{T}}).$$

To account for rotational effects, a couple-stress tensor $\boldsymbol{\mu}$ is introduced, which is conjugated to the curvature strain tensor $\boldsymbol{\kappa}$. The momentum equations governing mass balance and linear momentum for each material point in the Cosserat continuum are written as follows for general conditions:

$$\begin{aligned} \nabla \cdot \boldsymbol{\tau} + \mathbf{f} &= \rho \frac{\partial^2 \boldsymbol{u}}{\partial t^2} \\ \nabla \cdot \boldsymbol{\mu} + \boldsymbol{e} : \boldsymbol{\tau} + \mathbf{m} &= \rho \mathbf{I} \frac{\partial^2 \boldsymbol{\omega}}{\partial t^2} \end{aligned} \tag{5.21}$$

Where $\mathbf{f}$ and $\mathbf{m}$ are respectively the body forces for stresses and couple stresses, $\mathbf{e}$ is the permutation tensor and $\mathbf{I}$ is the micro inertia tensor (defined as $\mathbf{I} = \frac{1}{2}R^2$ for particles of radius R). From the general degrees of freedom, we can derive the strain tensor $\boldsymbol{\gamma}$, that consists of a symmetric part $\boldsymbol{\epsilon}$ and a non-symmetric part $\boldsymbol{\gamma}^{\mathrm{n-sym}}$:

$$\boldsymbol{\gamma} = \boldsymbol{\epsilon} + \boldsymbol{\gamma}^{\mathrm{n-sym}}, \quad \text{where} \quad \boldsymbol{\epsilon} = \frac{1}{2}(\boldsymbol{\nabla u} + \boldsymbol{\nabla u}^{\mathsf{T}}),$$

$$\boldsymbol{\gamma}^{\mathrm{n-sym}} = \frac{1}{2}(\boldsymbol{\nabla u} - \boldsymbol{\nabla u}^{\mathsf{T}}) + \boldsymbol{e} \cdot \boldsymbol{\omega}.$$

It results that the strain tensor can simply be written as:

$$\boldsymbol{\gamma} = \nabla \boldsymbol{u} + \boldsymbol{e} \cdot \boldsymbol{\omega} \tag{5.22}$$

Similarly, the curvature strain tensor is derived as:

$$\boldsymbol{\kappa} = \nabla \boldsymbol{\omega} \tag{5.23}$$

The classical small-strain assumption is maintained here and both strain tensors can be decomposed into elastic and plastic parts:

$$\boldsymbol{\gamma} = \boldsymbol{\gamma}^e + \boldsymbol{\gamma}^{\mathrm{p}} \quad \text{and} \quad \boldsymbol{\kappa} = \boldsymbol{\kappa}^e + \boldsymbol{\kappa}^p$$

In this work, only a two-dimensional Cartesian (x, y) plane problem is considered. The problem is therefore reduced to solving for the general displacement vector, rewritten as:

$$\boldsymbol{u} = [u_x, u_y, \omega_z] \tag{5.24}$$

The general system of equations presented in Equation 5.21 can also be rewritten for two-dimensional variables as:

$$\begin{aligned} \frac{\partial \tau_{xx}}{\partial x} + \frac{\partial \tau_{xy}}{\partial y} + f_x &= \rho \frac{\partial^2 u_x}{\partial t^2} \\ \frac{\partial \tau_{yx}}{\partial x} + \frac{\partial \tau_{yy}}{\partial y} + f_y &= \rho \frac{\partial^2 u_y}{\partial t^2} \\ \frac{\partial \mu_{zx}}{\partial x} + \frac{\partial \mu_{zy}}{\partial y} + \tau_{yx} - \tau_{xy} + m_z &= \rho I_z \frac{\partial^2 \omega_z}{\partial t^2} \end{aligned} \tag{5.25}$$

The strain components for the Cartesian plane are defined as:

$$\begin{aligned} \gamma_{xx} &= \frac{\partial u_x}{\partial x}, \quad \gamma_{xy} = \frac{\partial u_y}{\partial x} + \omega_z \\ \gamma_{yy} &= \frac{\partial u_y}{\partial y}, \quad \gamma_{yx} = \frac{\partial u_x}{\partial y} - \omega_z \end{aligned} \tag{5.26}$$

In a perfect isotropic and elastic bi-dimensional Cosserat medium, the stress-strain relationship is defined as follows:

$$\begin{bmatrix} \tau_{xx} \\ \tau_{yy} \\ \tau_{xy} \\ \tau_{yx} \\ \mu_{zx} \\ \mu_{zy} \end{bmatrix} = \begin{bmatrix} K+\frac{4}{3}G & K-\frac{2}{3}G & 0 & 0 & 0 & 0 \\ K-\frac{2}{3}G & K+\frac{4}{3}G & 0 & 0 & 0 & 0 \\ 0 & 0 & G+G_c & G-G_c & 0 & 0 \\ 0 & 0 & G-G_c & G+G_c & 0 & 0 \\ 0 & 0 & 0 & 0 & M+M_c & 0 \\ 0 & 0 & 0 & 0 & 0 & M+M_c \end{bmatrix} \begin{bmatrix} \gamma_{xx} \\ \gamma_{yy} \\ \gamma_{xy} \\ \gamma_{yx} \\ \kappa_{zx} \\ \kappa_{zy} \end{bmatrix}$$

Where K is the bulk modulus, G is the shear modulus that corresponds to the Cauchy mechanics modulus. G_c is the Cosserat shear modulus, that links the non-symmetric parts of stresses and strains tensors. M and M_c are Cosserat couple coefficients with dimensions of a stress multiplied by a length squared, often set equal to $M = M_c = \frac{5GR^2}{2}$, where R is the Cosserat grain radius (Rattez, 2017).

Finally, the elasto-plastic stress-strain relationship is described by a Drucker-Prager yield surface and plastic potential, expressed in Equations 5.27 and 5.28, which have been extensively presented in previous works by Rattez et al. (2018) (paper) or Rattez (2017) (thesis).

$$F = \tau + \mu\sigma - c \tag{5.27}$$

$$G = \tau + \beta\sigma \tag{5.28}$$

where μ and β are the friction and dilatancy coefficients, respectively, and c is the cohesion. τ is the generalized second invariant of the deviatoric stresses expressed in Equation 5.29 and $\sigma = \frac{tr(\tau)}{3}$.

$$\tau = \sqrt{h_1 \boldsymbol{\tau}^d : \boldsymbol{\tau}^d + h_2 \boldsymbol{\tau}^d : \boldsymbol{\tau}^{d,T} + \frac{1}{R^2}(h_3 \boldsymbol{\mu}^d : \boldsymbol{\mu}^d + h_4 \boldsymbol{\mu}^d : \boldsymbol{\mu}^{d,T})} \tag{5.29}$$

where $\boldsymbol{\tau}^d$ and $\boldsymbol{\mu}^d$ are the deviatoric parts of the stress and couple-stress tensors, respectively, and h_1, h_2, h_3, and h_4 are coefficients that can be determined on basis of micromechanical considerations (Stefanou et al., 2017; Rattez, 2017). The system is numerically integrated with the same displacement-rotation incremental finite element formulation as presented in Rattez et al. (2018), that was first implemented in Redback (Poulet et al., 2017), an adjacent module of the MOOSE open-source Finite Element framework (Giudicelli et al., 2024).

This section validates the numerical implementation of the Cosserat continuum coupled to the PFEM algorithm using numerical examples. Firstly, we compare the performance, in Section 5.4.1, of the PFEM model with the numerical results of FEM simulations of a shear band problem presented in Rattez (2017). The results obtained using a FEM formulation with a structured layered mesh and with an unstructured mesh are compared with results obtained with the PFEM coupling. The aim of this benchmark is to demonstrate that all state variables are correctly remapped at each PFEM remeshing step, and that remeshing does not affect the numerical response. In addition of the strain, plastic strain and stress field, the curvature strain, plastic curvature strain field and the couple-stress tensor are also remapped. If a dynamics problem is performed, the velocities, accelerations, angular velocities and angular accelerations are also remapped. Secondly, we demonstrate how the Cosserat continuum, coupled with an efficient remeshing algorithm, enables accurate computation of retroactive failures of soil blocks.

5.4.1 Benchmark - shear band

This numerical example studies the shearing of a fault core represented as an infinite layer of height h. The top of the layer is subjected to a shearing velocity V and is fixed for the rotations. The bottom layer is fully fixed in the x and y directions, as well as the rotations. These boundary conditions are represented in Figure 5.26. The modelled shear band is 60 mm high. A shear modulus K of 4000 MPa, a bulk modulus G of 4000 MPa and a Cosserat bulk modulus G_c of 2000 MPa are considered for the elastic properties. The Cosserat radius R is set to 2.5 mm. In this example, a purely cohesive material is considered with a cohesion $c = 100$ MPa. Strain softening is modelled with a linear softening rule

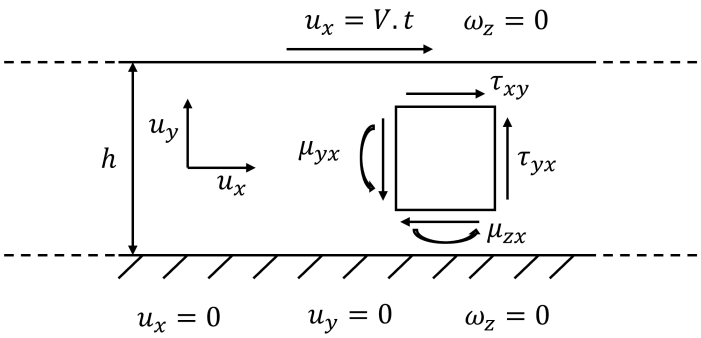


Figure 5.26: Boundary conditions of the sheared fault core.

with a hardening coefficient $h_s = -4$ MPa, that corresponds to the slope of the linear softening curve described in Equation 5.20.

Numerically, periodic boundary conditions are considered on both sides of the block. Figure 5.27 shows the evolution of the tangential stress τ_{xy} at the top of the band as a function of $\frac{u_x}{h}$, the adimensionalized horizontal displacement. Note that a mesh convergence was first performed for both the structured and the unstructured meshes. This step is not detailed here. But it allowed to determine the characteristic mesh size that provides mesh-independent results for both the layered and the unstructured meshes. The characteristic mesh size in the shear band is 1 mm for the unstructured mesh, while the structured mesh is composed of 200 layers. Mesh sizes below this value converge to the same stress-strain relationship.

This result shows that a fine mesh is required to capture the shear band, with a length scale to mesh size ratio of 2.5. Sharbati and Naghdabadi (2006) report that, in their specific test case, the mesh-independency of the results was reached from a length scale to mesh size ratio of 0.15, which is much smaller than the one obtained in this work. A common observation is that a large internal length results in a larger shear band thickness (Mühlhaus and Vardoulakis, 1987). Moreover, de Borst et al. (2022) report a rule of thumb stating that the element mesh size should be 3-5 times the internal length.

It is observed that the PFEM algorithm provides satisfying results in comparison with the FEM formulation. This lends confidence to the PFEM algorithm, in the sense that the solution is not affected by

remeshing or the way state variables are remapped.

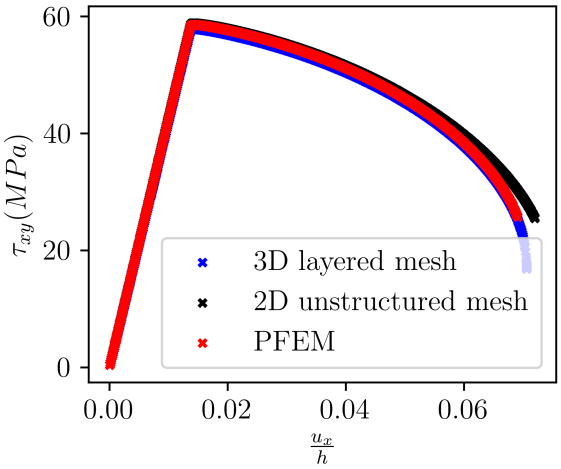


Figure 5.27: Comparison between FEM and PFEM results. The PFEM solution does not modify the stress-strain relationship.

The plastic curvature computed with the PFEM algorithm is plotted on the final deformed shape computed in Figure 5.28. The shear band is clearly identified and the results are symmetrical. Interestingly, the plastic curvature is zero at the centre of the shear band. This indicates that the material is rolling above and below this zero plastic curvature zone, as we could expect.

As depicted in Figure 5.7, the tracking of the boundary requires a specific treatment in the PFEM algorithm. In the specific implementation of PFEM presented in this work, a background mesh is used in addition to the physical mesh to perform the remeshing step. In most cases, the background mesh is intended to remain static. But in the specific case of the sheared layer, the top boundary has to be tracked, as it is allowed to move vertically. Therefore, the top of the background mesh is composed of the nodes that correspond to the top of the physical mesh. Before each remeshing step, these nodes are moved accordingly in both meshes allowing the top physical boundary to be tracked and identified. The identification of the boundary nodes is required to apply the proper boundary conditions after remeshing.

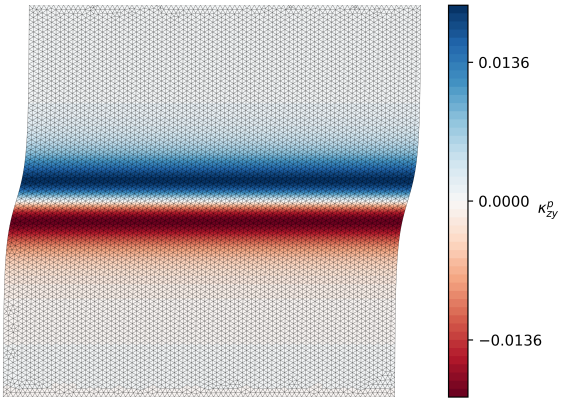


Figure 5.28: Plastic curvature (κ^p_{zy}) field computed with the PFEM algorithm for the sheared layer test.

5.4.2 Retroactive slope failure

In this section, we present the application of the developed Cosserat PFEM formulation to the retroactive slope failure case already presented in Section 5.3.3. The same geometry, boundary conditions and elasto-plastic properties are selected. In addition, a Cosserat radius R of 1.2 mm is selected. The time step used for the simulation is 0.0005 s. The mesh size is set to 0.04 m, which is relatively large compared to the selected Cosserat radius. A proper mesh convergence study should be performed, consisting in reducing the mesh size until the results do not change significantly. However, the computational cost of the Cosserat elasto-plastic algorithm, coupled with the PFEM to simulate large displacements is very high and the convergence study is not performed here. Figure 5.29 depicts the plastic curvature computed by the Cosserat-PFEM framework. Two shear bands are clearly identified, but they appear wider than in the previous case without Cosserat mechanics.

Here, the objective is to demonstrate the ability of the framework to be employed for such complex problems. It shows the the PFEM-Cosserat framework appears to be promising in its ability to simulate retroactive landslides. A more complete parametric study should be performed, as

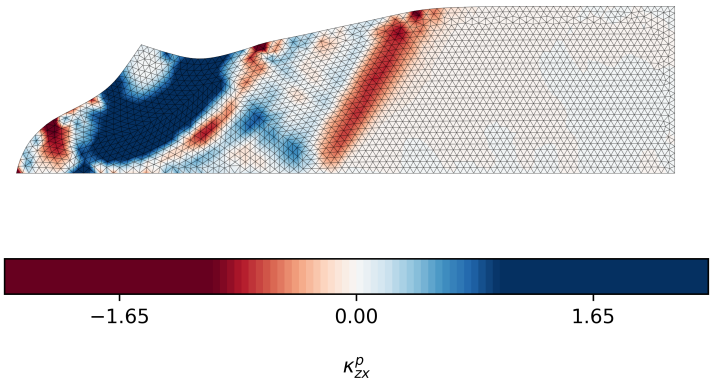


Figure 5.29: Plastic curvature (κ^p_{zx}) field at t = 0.85 s

well as a proper mesh convergence analysis.

5.5 Conclusion

This chapter was dedicated to the development of a large-displacement geomechanical model. In the context of dike breaching, the aim of such a model is to simulate the widening of the breach, or the longitudinal sliding of dike material which are key factors driving the evolution of the discharge through the breach. The development of this model is essential for simulating the dike breaching process in a more physical way than the bank failure operator proposed in Chapter 2, which simply relies on a friction angle.

After analysing the different possible numerical methods, the Particle Finite Element Method (PFEM) was selected. This lagrangian method is particularly suited to problems involving large free-surface displacements. As described, the method has the key advantage of relying on a classical finite element formulation. In fact, PFEM can be described as a "blind" formulation applicable to any type of large deformation problem: the only requirement is to provide a displacement field to the remeshing algorithm. From there, a remeshing step is performed, and the problem can be solved again on a new mesh.

After describing the general PFEM steps, granular column collapses examples were presented to illustrate the ability of the algorithm to simulate large displacements. Retroactive slope failures, which are particularly challenging to model were also successfully simulated. Moreover, these problems can be associated to blocks failures that occur during dike breaching. The influence of the constitutive model for the softening law and of the mesh size were underlined.

To mitigate the mesh-dependence issue, the PFEM formulation was then coupled with a Cosserat elasto-plastic model. This model introduces a length scale in the problem, which allows to regularize strain localization issues. The numerical implementation of the Cosserat PFEM algorithm was validated through a shear band benchmark. Finally, the developed Cosserat PFEM framework was applied to the retroactive slope failure case. The high computational cost of the Cosserat-PFEM model was recognized as a major limitation. Moreover, a proper mesh convergence analysis is required to validate the results obtained for a given situation. The numerical test performed in this chapter required a high ratio of Cosserat radius to mesh size (2.5), which is not ideal. This means that to simulate realistic problems, such as the retrogressive landslide occuring in soft clays, a very fine mesh should be used to ensure mesh-convergence.

With the developments presented in this chapter, together with those of the preceding ones, it is now possible to simulate all the processes involved in dike breaching within a two-dimensional framework. The next chapter will present a proof-of-concept demonstration of a complete dike breaching simulation.

Key takeaways from this chapter

→ A Particle Finite Element Method (PFEM) algorithm was developed to simulate large displacements in geomechanics.

→ The objective is to use PFEM to simulate large geomechanical displacements occurring during dike breaching.

→ The PFEM algorithm is applied to various problems, including granular column collapses and retroactive slope failures.

→ The influence of the constitutive model and mesh refinement are underlined.

→ A Cosserat elasto-plastic model is coupled with the PFEM algorithm to mitigate mesh-dependence issues.

→ The high computational cost of the Cosserat-PFEM model is recognized as a major limitation.

CHAPTER 6

Proof-of-concept for a coupled hydraulics and geomechanics model

This chapter combines the approaches from previous chapters to simulate a dike breaching event. Using the idealized test case from Van Emelen et al. (2012) (discussed in the introduction), two simulations are performed to examine the dike breaching process, with different assumptions and models for the dike failure. First, the dike is modeled using only the sediment transport-based approach presented in Chapter 2, in which the dike is progressively eroded by the overtopping flow. Second, a coupled simulation integrates both the sediment transport-based approach and the geomechanical approach based on PFEM (Chapter 5) to account for slope failures and the consequent large displacements. The analysis focuses on the differences between these two models, as reflected in the output hydrographs. The goal of the chapter is to underline the need of tightened coupling between hydrodynamic, sediment transport and geomechanical processes to accurately simulate dike breaching events.

Contents

6.1 Description of the model 173

6.2 Erosive failure of the dike 174
6.3 Downstream slope failure scenario 176

6.1 Description of the model

The modeled situation corresponds to a modified version of the idealized test case from Van Emelen et al. (2012). In their work, an idealized 1:50 scale model of the 17th street canal breach during Hurricane Katrina was considered. As mentioned in the introduction, the dike was not included in either the experiments or the numerical model. Rather, the breaching process was considered to be instantaneous. In this chapter, the numerical setup is modified to include a dike made of erodible material. The dike is 0.2 m high with a 1:3 (vertical-horizontal) slope in the upstream part and a 1:2 slope in the downstream part. This steep downstream slope is selected to enhance the slope failure process The crest is 0.05 m wide. The initial geometry of the problem is depicted in Figure 6.1. A 3D view of the channel with the dike is also represented in Figure 6.2.

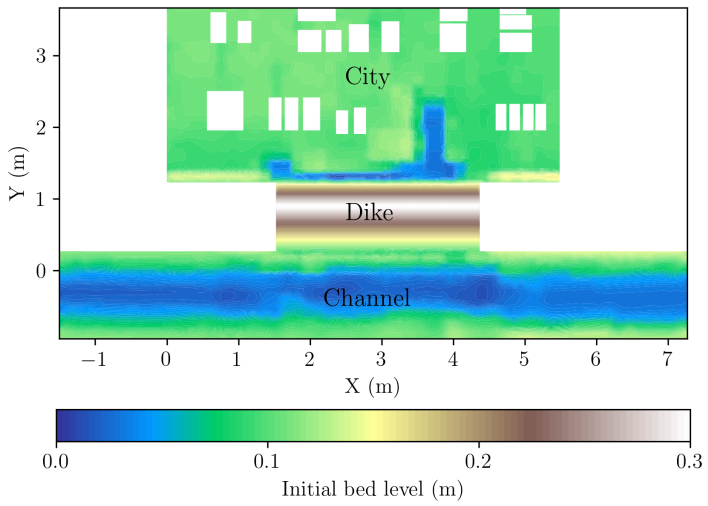


Figure 6.1: Bed level representation before the breaching of the dike.

An initial water depth of 0.2 m is set in the channel. A constant water discharge of 0.057 m^3/s is provided at the upstream boundary of the channel. The dike breaching is studied in two scenarios. First, the dike is modeled using only the sediment transport-based approach

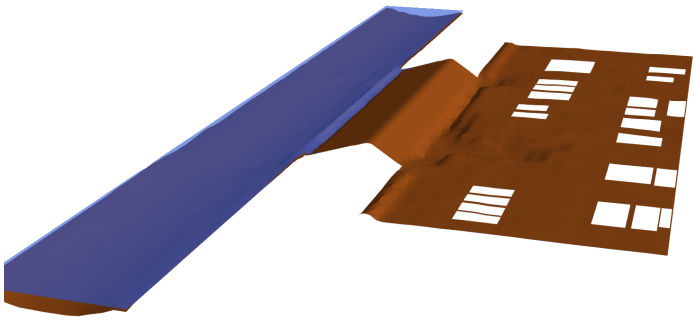


Figure 6.2: 3D view of the channel with the dike before the breaching.

presented in Chapter 2. The following parameters are considered for the sediment transport model: a porosity of 0.44, a Manning friction coefficient of 0.0167 $m^{-1/3}s$, a critical Shields parameter of 0.047, and a median grain diameter of 0.0017 m.

Yet a critical question remains: what if the downstream slope of the dike could fail due to geomechanical instability? Would this failure impact the breaching process and the outflow hydrograph? To answer these questions, a second simulation is performed where the dike is modeled using a coupled model integrating both the sediment transport-based approach and the geomechanical approach based on PFEM (Chapter 5).

6.2 Erosive failure of the dike

The water level rises upstream the dike until overtopping occus at around t=30 s as shown in Figure 6.3. This initial overflow occurs at a point on the crest located upstream of the channel. This is due to the natural slope of the channel, which implies a higher water level in this area. From this point, the erosion process starts to severly affect the dike morphological evolution. Figure 6.4 shows the bed level at t=35 s.

The erosion process continues until the dike is completely breached.

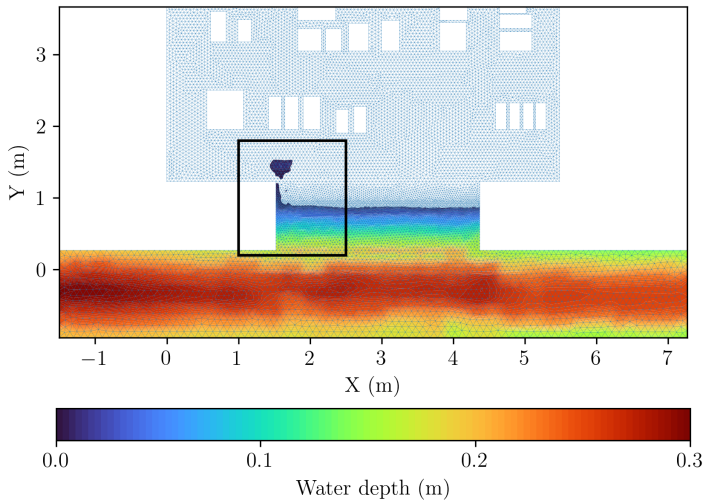


Figure 6.3: Water starts to flow on the downstream slope of the dike after 30 seconds.

Figure 6.5 shows the bed level at t=100 s. At this point, the dike has been almost totally eroded.

Yet, contrariwise to the simulation presented in the introduction where the breaching was considered to be instantaneous, the current model provides a more realistic representation of the breaching process, and thus of the outflow hydrograph. Figure 6.6 shows the comparison between the outflow hydrograph obtained with the sediment transport-based approach and the one obtained with the instantaneous breaching assumption from the introduction. The instantaneous breaching assumption produces a much more important initial discharge since the water accumulating upstream of the dike is suddenly released. This assumption clearly leads to an overestimation of the outflow discharge. The sediment transport approach produces a gradual increase of the outflow discharge, with a lag time before the outflow starts. This is a critical aspect for decisionmakers as it provides the actual possible evacuation time before the flooding occurs downstream of the dike.

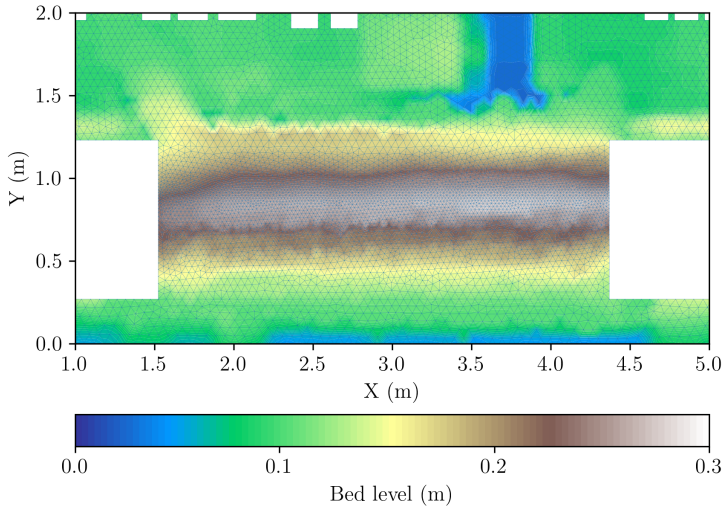


Figure 6.4: The erosion process after 35 seconds.

6.3 Downstream slope failure scenario

In this section, the geomechanical failure of the unstable downstream slope is considered. The scenario is fictive, but illustrates that combining all the processes involved is possible. As the water level rises, the downstream slope becomes saturated and the effective stresses decrease leading to the instability. In this idealised example, the sliding occurs in a 2D plane, and this plane is extruded in the 3D space to represent the volume of the dike. In this scenario, the subsurface flow is not considered and does not generate shear strength losses. An exponential softening law is used to represent the decrease of the shear strength, from 1 kPa to 0.5 kPa with a softening rate of 15. The elastic properties of the soil consist of a Young's modulus of 1 MPa and a Poisson's ratio of 0.4. The Cauchy mechanics is used, so the problem is not regularized for mesh dependency. A mesh with a characteristic element size of 5 mm is selected.

The dike surface is updated every 0.1 seconds in the Shallow-Water-Exner domain to account for the geomechanical failure that was imposed

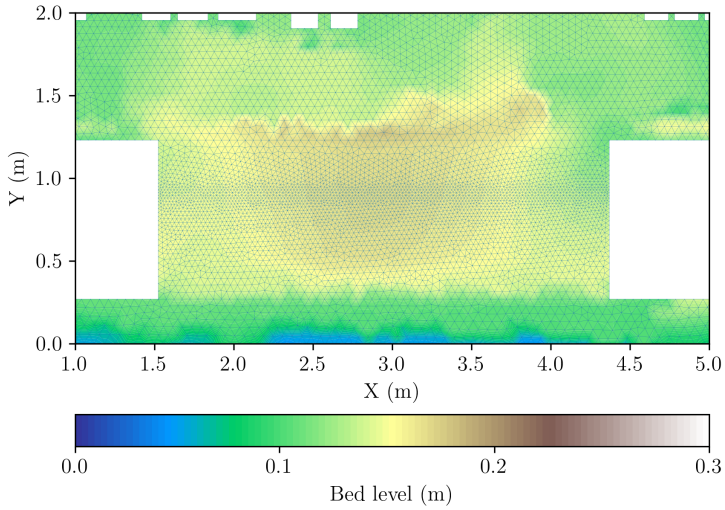


Figure 6.5: The erosion process after 100 seconds. The dike is almost totally eroded.

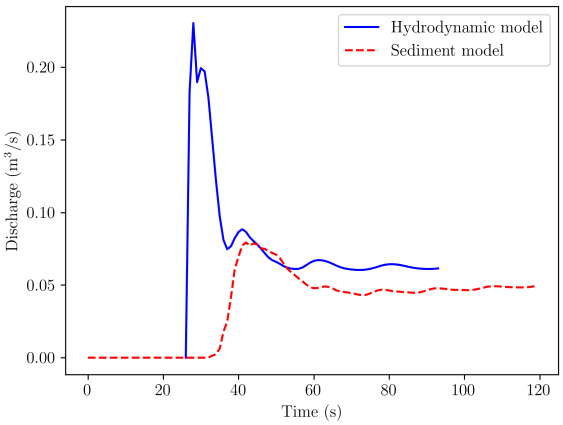


Figure 6.6: Comparison between the output hydrographs obtained with the sediment transport-based approach and the instantaneous breaching assumption.

to start after 26 s of water-level rising, i.e. the starting time of the actual overtopping. A linear interpolation is used to update the Shallow-Water-Exner cells bed level based on the bed level computed in the geomechanical domain. This arbitrary choice is motivated by the idea that the water at the crest is very likely to generate saturation of the downstream slope, leading to shear strength losses and slope failure. The state of the slope after 26.5 seconds is depicted in Figure 6.7. Figure 6.8 shows the computed equivalent plastic strain in the sliding mass, in the 2D plane. Finally 6.9 shows the bed level in a top view after 26.5 seconds in the Shallow-Water-Exner domain.

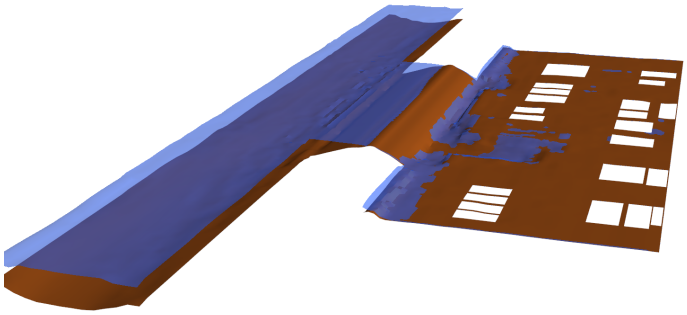


Figure 6.7: 3D view of the channel at time t=26.5 s. The failure of the downstream slope has started.

The full extent of the geomechanical failure is reached after 28.4 seconds. Three figures are provided to illustrate the state of the dike at this time: a 3D view of the channel (Figure 6.10), the equivalent plastic strain in the sliding mass (Figure 6.11) and the bed level in a top view (Figure 6.12). After this time, the erosion process takes over and continuously erodes the failed slope.

Figure 6.13 shows the outflow hydrograph obtained using the coupled approach, which is compared with those obtained using the sediment transport approach and the hydrodynamics approach alone.
The geomechanical failure produces a lag in the outflow. This lag is

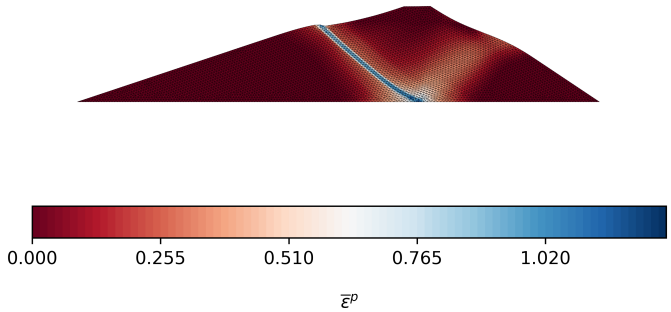


Figure 6.8: The equivalent plastic strain ($\bar{\epsilon}^p$) at time t=26.5 s. The sliding failure propagates.

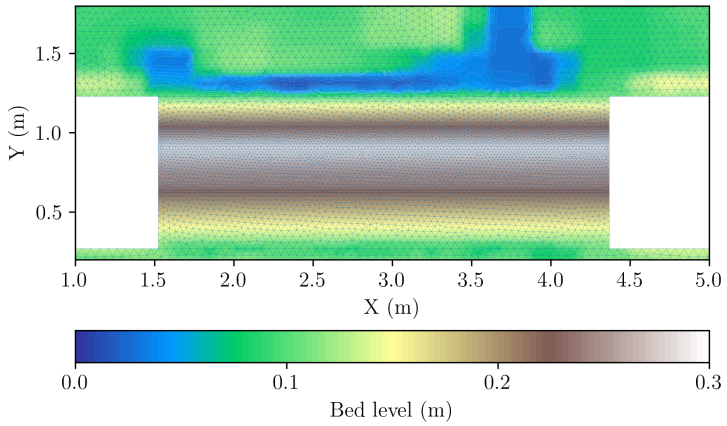


Figure 6.9: A zoom on the bed level at time t=26.5 s in the shallow-water-Exner domain during the geomechanical failure.

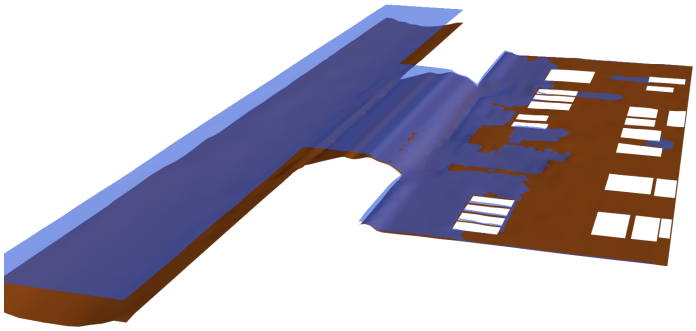


Figure 6.10: 3D view of the channel at time t=28.4 s. The full extent of the geomechanical failure is reached and water flows downstream.

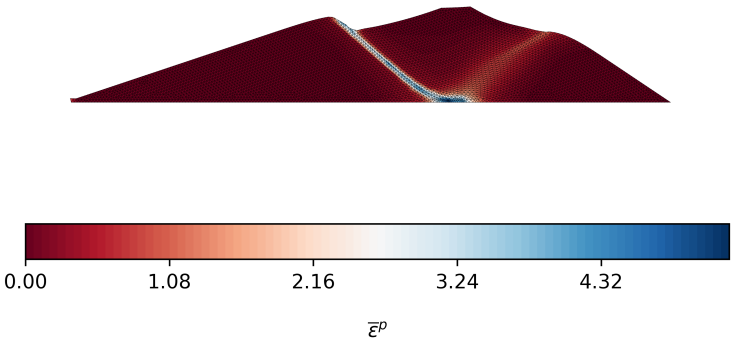


Figure 6.11: The equivalent plastic strain ($\overline{\epsilon}^p$) at time t=28.4 s. The sliding failure is fully developed.

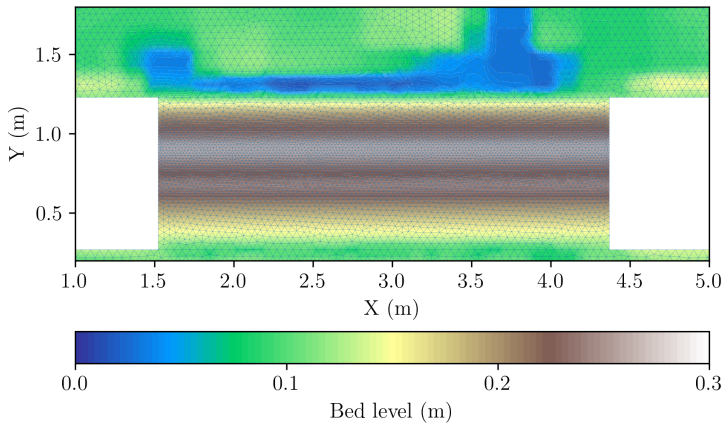


Figure 6.12: A zoom of the bed level at time t = 28.4 s in the shallow-water Exner domain. It shows the modification of the bed level following geomechanical failure.

conditioned by the selection of the initiating time, but the key point is that a geomechanical failure will generate a delay in the response of the system. As soon as the slope fails, a large volume of water is released, producing the first peak flow. Then, the erosion process takes over and leads to the second peak flow. The decrease in outflow discharge appears sooner than in the sediment transport only case.

Regarding the computational cost, no specific and systematic analysis is performed. However, the order of magnitude for the different components is very different. While the hydrodynamics and sediment transport components run in a few minutes on a standard workstation, the geomechanics component runs in a few hours on a computer with 40 CPU cores.

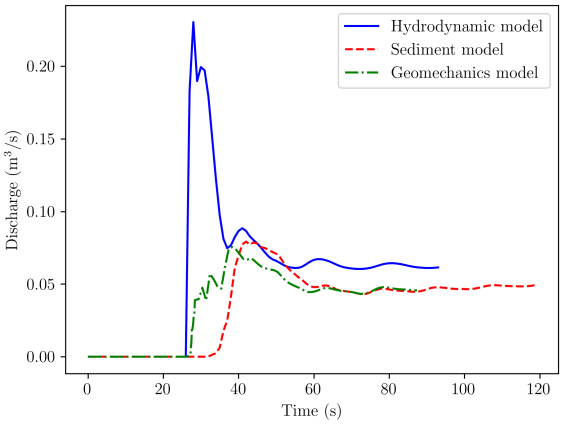


Figure 6.13: Comparison between the output hydrographs obtained with the three approaches: hydrodynamics only, sediment transport based and fully coupled.

Key takeaways from this chapter

→ A proof-of-concept for a coupled hydraulics and geomechanics model is presented.

→ An overtopping scenario is modelled combining sediment transport and geomechanics.

→ The model shows that a combination of the different physical aspects of overtopping is possible.

→ Geomechanics has the highest computational cost.

CHAPTER 7

Conclusion

The first intent of this thesis is to propose and conceptualize a holistic modelling approach of the dike breaching process by overtopping. Starting from observations of the process in the field and in laboratory experiments, the main physical mechanisms involved were identified. **Sediment transport, surface-subsurface flow interaction, effect of suction on the material's strength, and large deformations of the dike structure were recognized as key processes.** The main steps of the thesis are summarized below.

As a dike is overtopped by water, the very first visible effect is the erosion of the dike material by the fast flow. The erosion process is responsible for a significant morphological evolution of the dike. To model this process, **a sediment transport-based** approach was presented in Chapter 2. This approach is well established in the literature. It consists in coupling the Shallow-Water equations system with the Exner equation, a sediment conservation equation complemented by a transport formula. Here, the Meyer-Peter-Müller formula was selected. To complement the approach, a **bank-failure** operator is included to account for mass failures as the breach slopes become too steep.

While the approach provides a good representation of the erosion process and offers a direct answer to outflow hydrograph quantification, it does have significant limitations. Specifically, the bank-failure operator does not account for the saturation degree of the dike, any time scale effects, or shear strength beyond a simple friction angle.

The first cornerstone of the thesis is the following hypothesis: the evolution of the suction influences in a significant way the breaching process. To investigate the hypothesis, **a coupled surface-subsurface flow model** was developed in Chapter 3. In this Chapter, it is shown that combining the Shallow-Water equations (for the surface flow) with the Richards equation (for the unsaturated porous media flow) allows to capture the evolution of the pore water pressure and saturation degree in the dike before and during the breaching process.

As the pore water pressure evolves, the stress state and thus the strength of the dike is affected. Chapter 4 was dedicated to the effect of suction on the **shear strength of unsaturated soils**. To study the evolution of dike stability during overtopping, the shear strength reduction method (SSRM) was employed to associate a given suction field with a safety factor. At each step of a given overtopping event, the

pore water pressure field responsible for changes in effective stress, was obtained from the coupled surface-subsurface flow model. Then, it served as input into a geomechanical model to determine the associated safety factor and its evolution in time. With this approach, it is possible to predict with physical accuracy, dike failure initiation due to overtopping and infiltration. From this, a clear workflow was established to link hydrodynamic, subsurface flow and geomechanical processes. Nevertheless, the approach remained limited to the prediction of failure initiation, without considering the full runout.

To further enhance the model, Chapter 5 introduced the **Particle Finite Element Method (PFEM)**. This Lagrangian method captures the large geomechanical deformations that could occur during an overtopping event. PFEM was presented in detail, insisting on the ability of the method to be adapted to various geomechanical problems such as granular column collapse or landslides. The Cosserat continuum theory was used to regularize strain localization problems. The coupling between PFEM and the Cosserat continuum theory was performed and validated by comparing the numerical results of the coupling with numerical results retrieved from the litterature for a shear band problem. The implementation appeared to be promising but associated with challenges such as the high computational cost.

The final Chapter, Chapter 6, combined previous developments to simulate a dike breaching event. This Chapter must be seen as a proof of concept of the holistic approach proposed in this thesis. It intends to demonstrate the feasibility of this integrated approach, capable of simulating a full dike breaching process while accounting for the main physical processes introduced initially.

Perspectives

There are numerous potential future developments associated with this thesis, and improvements to the modelling are always possible. The increasing complexity of the model must not cause us to lose sight of the objective, which is to provide a quantitative answer to the question: “If the dike fails, what flow rate will pass through the breach over time?”. In a paper of philosophical scope (Biot, 1963), Prof. Maurice Biot asks an essential question: “Are we drowning in complexity?”. He notes the importance of simplicity in technical solutions, coupled with a deep

understanding of the problem at hand. He also questions the importance given to formalism in solving practical problems, which he describes as excessive if pursued only for its own sake. This reflection should encourage us to prioritize future developments that aim to bring the model even closer to physical reality and to ask ourselves whether the added complexity is justified by a significant improvement in the model's predictive capabilities.

The global approach proposed in this thesis at least allows to underline the key processes that could be incorporated in simpler models. A duality could be considered: on one side a very complex model that accounts for every physical process involved, on the other side a simplified model where key processes are added gradually in a lighter way. Each of these models having the ability to complement the perspective of the other with the aim of converging towards operational use.

The uncertainty associated with the developed modelling approach must be recognized. Each physical process involved being complex and mainly nonlinear. Let us consider for instance water infiltration, governed by the Soil-Water Retention Curve, explored in Chapter 3. The measurement of this soil's property on different soils samples often lead to a certain range of values. Variations of a few percent of each parameter are very likely to be observed. Then measuring the soil's shear strength parameters with a triaxial test also leads to an important uncertainty. Combining the outcome of these two physical processes will inevitablely lead to accumulated uncertainties.

The hysteretic behaviour of unsaturated porous media flow was not accounted for in the coupled surface-subsurface flow model. In fact, only the main drying curve was considered to relate suction head and saturation degree. In reality, before and during an overtopping event, the dike undergoes several cycles of wetting and drying. As suction was recognized as a key parameter influencing the breaching process, it remains an open question whether accounting for hysteretic behaviour would meaningfully improve model predictions.

The unsaturated soil geomechanical model could also be improved. The role of suction during shear failure was well modelled, but other aspects of unsaturated soil mechanics could be considered. For instance, what is the impact of suction on the soil's stiffness? Or how does plastic strain modify the soil-water retention curve? If a compresive cap is

considered in the soil's constitutive law, what would be the impact of suction on its evolution?

The PFEM implementation provided interesting results, but remained limited to two-dimensional problems. To fully represent dike breaching events, a three-dimensional implementation is necessary. The block failures observed in the laboratory experiments or in the field are most of the time perpendicular to the flow. Of course, longitudinal dike failure could also occur, but a proper three-dimensional representation of the dike would be necessary to capture all possible failure modes.

The small-strains formulation used for the PFEM implementation could also be questionned. Indeed, large strains formulations are available in the literature and have the advantage of being objective to large rotations. A fundamental physical question is how soil behaves when subjected to large deformations. The classical geomechanical characterization tests are mostly designed to determine failure criteria, not to characterize behavior through full runout and large deformations.

Coupling all the developments together raises a lot of unanswered questions. The coupling strategy has to be carefully examined. To what extent should the different models interact with each other? What is the right time scale to make all the processes interact? Should the spatial coupling be examined as well? These are questions that need to be addressed in future work.

Bibliography

Adhikary, D.P., Jayasundara, C., Podgorney, R.K., Wilkins, A.H., 2016. A robust return-map algorithm for general multisurface plasticity. International Journal for Numerical Methods in Engineering 109, 218–234.

Alonso, E., Pereira, J., Vaunat, J., Olivella, S., 2010. A microstructurally based effective stress for unsaturated soils. Geotechnique 60, 913–925.

Alonso, E.E., Gens, A., Josa, A., 1990. A constitutive model for partially saturated soils. Geotechnique 40, 405–430.

ASCE/EWRI Task Committee on Dam/Levee Breaching, 2011. Earthen embankment breaching. Journal of Hydraulic Engineering 137, 1549–1564.

Augarde, C.E., Lee, S.J., Loukidis, D., 2021. Numerical modelling of large deformation problems in geotechnical engineering: A state-of-the-art review. Soils and Foundations 61, 1718–1735.

Awal, R., Nakagawa, H., Kawaike, K., Baba, Y., Zhang, H., 2008. An integrated approach to predict outflow Hydrograph due to landslide dam failure by overtopping and sliding. Annual Journal of Hydraulic Engineering 52, 151–156.

Babuška, I., Aziz, A.K., 1976. On the Angle Condition in the Finite Element Method. SIAM Journal on Numerical Analysis 13, 214–226.

Barzgaran, M., Mahdizadeh, H., Sharifi, S., 2019. Numerical simulation of bedload sediment transport with the ability to model Wet/Dry interfaces using an Augmented Riemann solver. Journal of Hydroinformatics 21, 834–850.

Bathe, K.J., 1996. Finite Element Procedures. Prentice Hall, Upper Saddle River, NJ.

Belytschko, T., Liu, W.K., Moran, B., Elkhodary, K., 2014. Nonlinear Finite Elements for Continua and Structures. 2nd ed., John Wiley & Sons, Chichester, West Sussex.

Benson, C.H., Chiang, I., Chalermyanont, T., Sawangsuriya, A., . Estimating van Genuchten Parameters α and n for Clean Sands from Particle Size Distribution Data. pp. 410–427.

Van den Berg, P., de Borst, R., Huétink, H., 1996. An Eulerean finite element model for penetration in layered soil. International journal for numerical and analytical methods in geomechanics 20, 865–886.

Bertolazzi, E., Manzini, G., 2007. On vertex reconstructions for cell-centered finite volume approximations of 2D anisotropic diffusion problems. Mathematical Models and Methods in Applied Sciences 17, 1–32.

Bezerra-Coelho, C.R., Zhuang, L., Barbosa, M.C., Alfaro Soto, M., van Genuchten, M.T., 2018. Further tests of the HYPROP evaporation method for estimating the unsaturated soil hydraulic properties. Journal of Hydrology and Hydromechanics 66, 161–169.

Bezuijen, A., Kruse, G.A.M., Van, M.A., 2005. Failure of peat dikes in The Netherlands, in: Proceedings of the 16th International Conference on Soil Mechanics and Geotechnical Engineering, pp. 1857–1860.

Biot, M.A., 1963. Are we drowning in complexity? Mechanical Engineering 85, 26–27.

Bishop, A.W., 1954. The use of pore-pressure coefficients in practice. Geotechnique 4, 148–152.

Bishop, A.W., Donald, I.B., 1961. The Experimental Study of Partly Saturated Soil in the Triaxial Apparatus, in: Proceedings of the 5th International Conference on Soil Mechanics, Paris. pp. 13–21.

Bogaard, T.A., Greco, R., 2016. Landslide hydrology: from hydrology to pore pressure. WIREs Water 3, 439–459.

de Borst, R., Alizadeh Sabet, S., Hageman, T., 2022. Non-associated cosserat plasticity. International Journal of Mechanical Sciences 230, 107535.

de Borst, R., Crisfield, M.A., Remmers, J.J.C., Verhoosel, C.V., 2012. Non-Linear Finite Element Analysis of Solids and Structures.

Brajkovic, J., Fettweis, X., Noël, B., Ghilain, N., Archambeau, P., Pirotton, M., Doutreloup, S., 2025. Increased intensity and frequency of extreme precipitation events in Belgium as simulated by the regional climate model MAR. Journal of Hydrology: Regional Studies 59, 102399.

Brooks, R., Corey, A., 1964. Hydraulic properties of porous media. Hydrology Paper 3. Colorado State University. Fort Collins.

Bugnion, L., Wendeler, C., 2010. Shallow Landslide Full-Scale Experiments in Combination with Testing of a Flexible Barrier, in: WIT Transactions on Engineering Sciences, pp. 161–173.

Bui, H.H., Fukagawa, R., Sako, K., Ohno, S., 2008. Lagrangian meshfree particles method (sph) for large deformation and failure flows of geomaterial using elastic–plastic soil constitutive model. International Journal for Numerical and Analytical Methods in Geomechanics 32, 1537–1570.

Bui, H.H., Fukagawa, R., Sako, K., Wells, J.C., 2011. Slope stability analysis and discontinuous slope failure simulation by elasto-plastic smoothed particle hydrodynamics (sph). Géotechnique 61, 565–574.

Cantero-Chinchilla, F.N., Castro-Orgaz, O., Dey, S., 2019. Prediction of Overtopping Dike Failure: Sediment Transport and Dynamic Granular Bed Deformation Model. Journal of Hydraulic Engineering 145, 04019021.

Carbonell, J.M., Monforte, L., Ciantia, M.O., Arroyo, M., Gens, A., 2022. Geotechnical particle finite element method for modeling of soil-structure interaction under large deformation conditions. Journal of Rock Mechanics and Geotechnical Engineering 14, 967–983.

Casulli, V., 2017. A coupled surface-subsurface model for hydrostatic flows under saturated and variably saturated conditions. International Journal for Numerical Methods in Fluids 85, 449–464.

Caviedes-Voullième, D., García-Navarro, P., Murillo, J., 2013. Verification, conservation, stability and efficiency of a finite volume method for the 1D Richards equation. Journal of Hydrology 480, 69–84.

Caviedes-Voullième, D., Murillo, J., Garcia-Navarro, P., 2012. Numerical simulation of groundwater-surface interactions by external coupling of the 3D Richards equation and the full 2D shallow-water equations, in: XIX International Conference on Water Resources CMWR 2012, University of Illinois at Urbana-Champaign.

Celia, M., Bouloutas, E., Zarba, R., 1990. A general mass-conservative numerical solution for the unsaturated flow equation. Water Resources Research 26, 1483–1496.

Chávez-Negrete, C., Domínguez-Mota, F., Santana-Quinteros, D., 2018. Numerical solution of Richards' equation of water flow by generalized finite differences. Computers and Geotechnics 101, 168–175.

Coleman, S., Andrews, D., Webby, M., 2002. Overtopping breaching of noncohesive homogeneous embankments. Journal of Hydraulic Engineering 128, 829–838.

Cremonesi, M., Franci, A., Idelsohn, S., Oñate, E., 2020. A State of the Art Review of the Particle Finite Element Method (PFEM). Archives of Computational Methods in Engineering 27, 1709–1735.

Danka, J., Zhang, L.M., 2015. Dike Failure Mechanisms and Breaching Parameters. Journal of Geotechnical and Geoenvironmental Engineering 141, 04015039.

De Maet, T., Hanert, E., 2011. An explicit Discontinuous-Galerkin surface-subsurface water flow model, in: Fifth International Conference on Advanced Computational Methods in Engineering (ACOMEN 2011).

Delpierre, N., Franzini, F., Gousenbourger, P.Y., Van Emelen, S., Zech, Y., Soares-Frazao, S., 2024. Breaching of Sand Dikes: Assessment

of 1D and 2D Numerical Models Against Laboratory Experiments. Journal of Hydraulic Research 62, 461–475.

Delpierre, N., Rattez, H., Soares-Frazao, S., 2023. Finite-volume coupled surface-subsurface flow modelling in earth dikes. Journal of Hydraulic Research 61, 754–763.

Delpierre, N., Rattez, H., Soares-Frazão, S., 2025. Surface–subsurface flow effect on earthen dikes geomechanical stability during overtopping event. Geomechanics for Energy and the Environment 43, 100709.

Dettmann, U., Bechtold, M., Frahm, E., Tiemeyer, B., 2014. On the applicability of unimodal and bimodal van Genuchten–Mualem based models to peat and other organic soils under evaporation conditions. Journal of Hydrology 515, 103–115.

Donea, J., Huerta, A., Ponthot, J.P., Rodríguez-Ferran, A., 2004. Arbitrary Lagrangian–Eulerian Methods: Part 1. Fundamentals, in: Stein, E., de Borst, R., Hughes, T.J. (Eds.), Encyclopedia of Computational Mechanics. John Wiley & Sons, Ltd, pp. 1–25.

Duretz, T., Räss, L., de Borst, R., Hageman, T., 2023. A comparison of plasticity regularization approaches for geodynamic modeling. Geochemistry, Geophysics, Geosystems 24, e2022GC010675.

Ebrahimi, K., Falconer, R., Lin, B., 2007. Flow and solute fluxes in integrated wetland and coastal systems. Environmental Modelling & Software 22, 1337–1348.

Ebrahimi, M., Delpierre, N., Gilles, A., Delforge, C.Z., Soares-Frazao, S., Swartenbroekx, C., Bousmar, D., 2025. Monitoring medium-scale dike breaching using photogrammetry: Preliminary results, in: Proceedings of the 12th International Conference on Fluvial Hydraulics, Liverpool, UK, 2nd- 6th September, 2024. 1 ed.. CRC Press.

Edelsbrunner, H., Kirkpatrick, D., Seidel, R., 1983. On the shape of a set of points in the plane. IEEE Transactions on Information Theory 29, 551–559.

Edelsbrunner, H., Mücke, E., 1999. Three dimensional alpha shapes. ACM Transactions on Graphics 13, 43–72.

Farthing, M., Ogden, F., 2017. Numerical solution of richards' equation: A review of advances and challenges. Soil Science Society of America Journal 81, 1257–1269.

Flynn, S., Vahedifard, F., Schaaf, D., 2026. A comprehensive dataset of riverine levee overtopping events for advancing risk assessment. Scientific Data 13, 36.

Foster, M., Fell, R., Spannagle, M., 2000. The statistics of embankment dam failures and accidents. Canadian Geotechnical Journal 37, 1000–1024.

Franzini, F., Soares-Frazao, S., 2018. Coupled finite-volume scheme with adapted Augmented Roe scheme for simulating morphological evolution in arbitrary cross-sections. Journal of Hydroinformatics 20, 1111–1130.

Franzini, F., Soares-Frazão, S., 2016. Efficiency and accuracy of lateralized HLL, HLLS and Augmented Roe's scheme with energy balance for river flows in irregular channels. Applied Mathematical Modelling 40, 7427–7446.

Fredlund, D.G., Morgenstern, N.R., 1977. Stress state variables for unsaturated soils. Journal of the Geotechnical Engineering Division 103, 447–466.

Furman, A., 2008. Modeling coupled surface–subsurface flow processes: A review. Vadose Zone Journal 7, 741.

Gan, J.K.M., Fredlund, D.G., Rahardjo, H., 1988. Determination of the shear strength parameters of an unsaturated soil using the direct shear test. Canadian Geotechnical Journal 25, 500–510.

Gazzini, C., . When the dams in libya burst: A natural or preventable disaster? URL: `https://www.crisisgroup.org/middle-east-north-africa/north-africa/libya/when-dams-libya-burst-natural-or-preventable-disaster`. accessed: October 10, 2025.

van Genuchten, M., 1980. A Closed-form Equation for Predicting the Hydraulic Conductivity of Unsaturated Soils. Soil Science Society of America Journal 44, 892–898.

Geuzaine, C., Remacle, J.F., 2009. Gmsh: A 3-D finite element mesh generator with built-in pre- and post-processing facilities. Int. J. Numer. Methods Eng. 79, 1309–1331.

Ghosh, S., Kikuchi, N., 1991. An arbitrary Lagrangian-Eulerian finite element method for large deformation analysis of elastic-viscoplastic solids. Computer Methods in Applied Mechanics and Engineering 86, 127–188.

Giudicelli, G., Lindsay, A., Harbour, L., Icenhour, C., Li, M., Hansel, J.E., German, P., Behne, P., Marin, O., Stogner, R.H., Miller, J.M., Schwen, D., Wang, Y., Munday, L., Schunert, S., Spencer, B.W., Yushu, D., Recuero, A., Prince, Z.M., Nezdyur, M., Hu, T., Miao, Y., Jung, Y.S., Matthews, C., Novak, A., Langley, B., Truster, T., Nobre, N., Alger, B., Andrš, D., Kong, F., Carlsen, R., Slaughter, A.E., Peterson, J.W., Gaston, D., Permann, C., 2024. 3.0 - MOOSE: Enabling massively parallel multiphysics simulations. SoftwareX 26, 101690.

Horgue, P., Franc, J., Guibert, R., Debenest, G., 2015. An extension of the open-source porousmultiphasefoam toolbox dedicated to groundwater flows solving the richards' equation. URL: `https://arxiv.org/abs/1510.01364v1`. arXiv preprint, accessed on 16 December 2025.

Hu, Y., Randolph, M.F., 1998. A practical numerical approach for large deformation problems in soil. International Journal for Numerical and Analytical Methods in Geomechanics 22, 327–350.

Idelsohn, S.R., Oñate, E., Pin, F.D., 2004. The particle finite element method: a powerful tool to solve incompressible flows with free-surfaces and breaking waves. International journal for numerical methods in engineering 61, 964–989.

IPCC, 2021. Climate change 2021: The physical science basis. Contribution of working group I to the sixth assessment report of the

intergovernmental panel on climate change. Cambridge University Press, Cambridge.

Ivanov, V., Arosio, D., Tresoldi, G., Hojat, A., Zanzi, L., Papini, M., Longoni, L., 2020. Investigation on the role of water for the stability of shallow landslides—insights from experimental tests. Water 12, 1203.

Jacquey, A.B., Rattez, H., Veveakis, M., 2021. Strain localization regularization and patterns formation in rate-dependent plastic materials with multiphysics coupling. Journal of the Mechanics and Physics of Solids 152, 104422.

Jennings, J.E.B., Burland, J.B., 1962. Limitations to the Use of Effective Stresses in Partly Saturated Soils. Geotechnique 12, 125–144.

Juez, C., Murillo, J., García-Navarro, P., 2014. A 2D weakly-coupled and efficient numerical model for transient shallow flow and movable bed. Advances in Water Resources 71, 93–109.

Kavetski, D., Binning, P., Sloan, S.W., 2001. Adaptive time stepping and error control in a mass conservative numerical solution of the mixed form of Richards equation. Advances in Water Resources 24, 595–605.

Kennedy, R., Take, W.A., Siemens, G., 2021. Geotechnical centrifuge modelling of retrogressive sensitive clay landslides. Canadian Geotechnical Journal 58, 1452–1465.

Khalili, N., Geiser, F., Blight, G.E., 2004. Effective Stress in Unsaturated Soils: Review with New Evidence. Int. J. Geomech. 4, 115–126.

Khalili, N., Romero, E., Marinho, F., 2022. State of the art report. Advances in unsaturated soil mechanics: constitutive modelling, experimental investigation, and field instrumentation, in: Proceedings of Twentieth International Conference on Soil Mechanics and Geotechnical Engineering (ICSMGE 2022): a Geotechnical Discovery Down Under, Sydney, New South Wales, Australia. pp. 297–348.

Kool, J.B., Parker, J.C., 1987. Development and evaluation of closed-form expressions for hysteretic soil hydraulic properties. Water Resources Research 23, 105–114.

Leyssens, T., 2025. Particle Finite Element Method with Mesh Adaptation for Modelling Free Surface Flows in Complex Geometries. Phd thesis. Université catholique de Louvain (UCLouvain). Louvain-la-Neuve, Belgium.

Leyssens, T., Henry, M., Lambrechts, J., Remacle, J.F., 2024. A delaunay refinement algorithm for the particle finite element method applied to free surface flows. International Journal for Numerical Methods in Engineering 125, e7554.

Likos, W.J., Lu, N., Godt, J.W., 2014. Hysteresis and uncertainty in soil water-retention curve parameters. Journal of Geotechnical and Geoenvironmental Engineering 140.

Lindsay, A.D., Gaston, D.R., Permann, C.J., Miller, J.M., Andrš, D., Slaughter, A.E., Kong, F., Hansel, J., Carlsen, R.W., Icenhour, C., Harbour, L., Giudicelli, G.L., Stogner, R.H., German, P., Badger, J., Biswas, S., Chapuis, L., Green, C., Hales, J., Hu, T., Jiang, W., Jung, Y.S., Matthews, C., Miao, Y., Novak, A., Peterson, J.W., Prince, Z.M., Rovinelli, A., Schunert, S., Schwen, D., Spencer, B.W., Veeraraghavan, S., Recuero, A., Yushu, D., Wang, Y., Wilkins, A., Wong, C., 2022. 2.0 - MOOSE: Enabling massively parallel multiphysics simulation. SoftwareX 20, 101202.

Locat, A., Leroueil, S., Fortin, A., Demers, D., Jostad, H., 2015. The 1994 landslide at Sainte-Monique, Quebec: geotechnical investigation and application of progressive failure analysis. Canadian Geotechnical Journal 52, 490–504.

Longoni, L., Scaioli, A., Panzeri, L., Arosio, D., Corti, M., Hojat, A., Papini, M., 2025. A new Landslide Investigation and Simulation Archive through downscaled landslide experiments. Scientific Data 12, 1668.

Martínez-Aranda, S., Fernández-Pato, J., García-Navarro, P., 2023. Non-equilibrium bedload transport model applied to erosive overtopping dambreach. Water 15, 3094.

Martínez-Aranda, S., Meurice, R., Soares-Frazão, S., García-Navarro, P., 2021. Comparative analysis of HLLC- and Roe-based models for the

simulation of a dam-break flow in an erodible channel with a 90° Bend. Water 13, 1840.

Martínez-Aranda, S., Murillo, J., García-Navarro, P., 2019. A 1D numerical model for the simulation of unsteady and highly erosive flows in rivers. Computers & Fluids 181, 8–34.

Matsui, T., San, K.C., 1992. Finite Element Slope Stability Analysis by Shear Strength Reduction Technique. Soils and Foundations 32, 59–70.

Meter Group, . HYPROP – water potential and hydraulic conductivity measurement. URL: `https://metergroup.com/products/hyprop/`. accessed December 13, 2025.

Meurice, R., Soares-Frazão, S., 2020. A 2D HLL-based weakly coupled model for transient flows on mobile beds. Journal of Hydroinformatics 22, 1351–1369.

Meyer-Peter, E., Müller, R., 1948. Formulas for bed-load transport. Proceedings of the 2nd Meeting of the IAHR 3, 39–64.

Mizutani, H., Nakagawa, H., Yoden, T., Kawaike, K., Zhang, H., 2013. Numerical modelling of river embankment failure due to overtopping flow considering infiltration effects. Journal of Hydraulic Research 51, 681–695.

Monforte, L., Arroyo, M., Carbonell, J.M., Gens, A., 2017. Numerical simulation of undrained insertion problems in geotechnical engineering with the Particle Finite Element Method (PFEM). Computers and Geotechnics 82, 144–156.

Monforte, L., Ciantia, M.O., Carbonell, J.M., Arroyo, M., Gens, A., 2019. A stable mesh-independent approach for numerical modelling of structured soils at large strains. Computers and Geotechnics 116, 103215.

Morris, M., Hassan, M., Kortenhaus, A., Visser, P., 2009. Breaching processes: A state of the art review. FLOODsite Project Report .

Moës, N., Chevaugeon, N., 2021. Lipschitz regularization for softening material models: the lip-field approach. Comptes Rendus. Mécanique 349, 415–434.

Mualem, Y., 1976. A new model for predicting the hydraulic conductivity of unsaturated porous media. Water Resources Research 12, 513–522.

Murillo, J., Garcia-Navarro, P., 2014. Accurate numerical modeling of 1D flow in channels with arbitrary shape. Application of the energy balanced property. Journal of Computational Physics 260, 222–248.

Murillo, J., García-Navarro, P., 2010. An Exner-based coupled model for two-dimensional transient flow over erodible bed. Journal of Computational Physics 229, 8704–8732.

Mühlhaus, H.B., Vardoulakis, I., 1987. The thickness of shear bands in granular materials. Geotechnique 37, 271–283.

Müller, C., Frank, P.J., Hager, W., 2016. Dyke overtopping: effects of shape and headwater elevation. Journal of Hydraulic Research 54, 1–13.

Nemnem, A.M., Tanim, A.H., Nahian, A., Khan, S., Goharian, E., Imran, J., 2025. How extreme rainfall and failing dams unleashed the Derna flood disaster. Nat. Commun. 16, 1–12.

Nuth, M., Laloui, L., 2008. Effective stress concept in unsaturated soils: Clarification and validation of a unified framework. International Journal for Numerical and Analytical Methods in Geomechanics 32, 771–801.

Oñate, E., Idelsohn, S.R., Del Pin, F., Aubry, R., 2004. The particle finite element method—an overview. International Journal of Computational Methods 1, 267–307.

Pan, Y., Li, L., Amini, F., Kuang, C., 2015. Overtopping erosion and failure mechanism of earthen levee strengthened by vegetated HPTRM system. Ocean Engineering 96, 139–148.

Paniconi, C., Putti, M., 1994. A comparison of Picard and Newton iteration in the numerical solution of multidimensional variably saturated flow problems. Water Resources Research 30, 3357–3374.

Panzeri, L., Delpierre, N., Scaioli, A., Rattez, H., Papini, M., Longoni, L., 2025. From small-scale laboratory physical tests to the shear strength reduction method in unsaturated soils. Engineering Geology Under review.

Pontillo, M., Schmocker, L., Greco, M., Hager, W.H., 2010. 1D numerical evaluation of dike erosion due to overtopping. Journal of Hydraulic Research 48, 573–582.

Poulet, T., Paesold, M., Veveakis, M., 2017. Multi-Physics Modelling of Fault Mechanics Using REDBACK: A Parallel Open-Source Simulator for Tightly Coupled Problems. Rock Mech. Rock Eng. 50, 733–749.

Rattez, H., 2017. Thermo-hydro-mechanical couplings and strain localization in Cosserat continua: application to stability analysis of rapid shear in faults. Phd thesis. Université Paris-Est. NNT: 2017PESC1181.

Rattez, H., Stefanou, I., Sulem, J., Veveakis, M., Poulet, T., 2018. The importance of Thermo-Hydro-Mechanical couplings and microstructure to strain localization in 3D continua with application to seismic faults. Part II: Numerical implementation and post-bifurcation analysis. J. Mech. Phys. Solids 115, 1–29.

Richards, L., 1931. Capillary conduction of liquids through porous mediums. Physics 1, 318–333.

Richardson, L.F., 1922. Weather Prediction by Numerical Process. Cambridge University Press, Cambridge.

Romero, E., 2013. A microstructural insight into compacted clayey soils and their hydraulic properties. Engineering Geology 165, 3–19.

Romero, E., Gens, A., Lloret, A., 1999. Water permeability, water retention and microstructure of unsaturated compacted Boom clay. Engineering Geology 54, 117–127.

Rotta, L.H.S., Alcântara, E., Park, E., Negri, R.G., Lin, Y.N., Bernardo, N., Mendes, T.S.G., Souza Filho, C.R., 2020. The 2019 brumadinho tailings dam collapse: Possible cause and impacts of the worst human and environmental disaster in brazil. International Journal of Applied Earth Observation and Geoinformation 90, 102119.

Salas, J.D., Obeysekera, J., 2014. Revisiting the Concepts of Return Period and Risk for Nonstationary Hydrologic Extreme Events. J. Hydrol. Eng. 19, 554–568.

Schindler, U., Durner, W., von Unold, G., Müller, L., 2010. Evaporation method for measuring unsaturated hydraulic properties of soils: Extending the measurement range. Soil Science Society of America Journal 74, 1071–1083.

Schmocker, L., Frank, P.J., Hager, W., 2014. Overtopping dike-breach: effect of grain size distribution. Journal of Hydraulic Research 52, 559–564.

Schmocker, L., Hager, W., 2012. Plane dike-breach due to overtopping: effects of sediment, dike height and discharge. Journal of Hydraulic Research 50, 576–586.

Shao, S., Ji, C., Graham, D., Reeve, D., James, P., Chadwick, A., 2006. Simulation of wave overtopping by an incompressible sph model. Coastal Engineering 53, 723–735.

Sharbati, E., Naghdabadi, R., 2006. Computational aspects of the cosserat finite element analysis of localization phenomena. Computational Materials Science 38, 303–315.

Shiach, J., Mingham, C., Ingram, D., Bruce, T., 2004. The applicability of the shallow water equations for modelling violent wave overtopping. Coastal Engineering 51, 1–15.

Shinomiya, Y., Takahashi, K., Kobiyama, M.e.a., 2001. Evaluation of the tortuosity parameter for forest soils to predict unsaturated hydraulic conductivity. Journal of Forest Research 6, 221–225.

Sills, G., Vroman, N., Wahl, R., Schwanz, N., 2008. Overview of new orleans levee failures: lessons learned and their impact on national levee design and assessment. Journal of Geotechnical and Geoenvironmental Engineering 134, 556–565.

Soares-Frazão, S., Le Grelle, N., Spinewine, B., Zech, Y., 2007. Dam-break induced morphological changes in a channel with uniform sediments: measurements by a laser-sheet imaging technique. Journal of Hydraulic Research 45, 87–95.

Soares-Frazão, S., Zech, Y., 2002. Dam break in channels with 90° bend. Journal of Hydraulic Engineering 128, 956–968.

Soares-Frazão, S., Zech, Y., 2011. Hllc scheme with novel wave-speed estimators appropriate for two-dimensional shallow-water flow on erodible bed. International Journal for Numerical Methods in Fluids 66, 1019–1036.

Soga, K., Alonso, E., Yerro, A., Kumar, K., Bandara, S., 2016. Trends in large-deformation analysis of landslide mass movements with particular emphasis on the material point method. Géotechnique 66, 248–273.

Soltani, A., Azimi, M., Boroomandnia, A., O'Kelly, B., 2021. An objective framework for determination of the air-entry value from the soil–water characteristic curve. Results in Engineering 12, 100298.

Stefanou, I., Sulem, J., Rattez, H., 2017. Cosserat approach to localization in geomaterials, in: Voyiadjis, G. (Ed.), Handbook of Nonlocal Continuum Mechanics for Materials and Structures. Springer, Cham.

Su, X., Zhang, M., Zou, D., Zhao, Y., Zhang, J., Su, H., 2022. Numerical scheme for solving the richard's equation based on finite volume model with unstructured mesh and implicit dual-time stepping. Computers and Geotechnics 147, 104768.

Sulsky, D., Chen, Z., Schreyer, H.L., 1994. A particle method for history-dependent materials. Computer methods in applied mechanics and engineering 118, 179–196.

Swartenbroekx, C., Soares-Frazão, S., Staquet, R., Zech, Y., 2010. Two-dimensional operator for bank failures induced by water-level rise in dam-break flows. Journal of Hydraulic Research 48, 302–314.

Terzaghi, K., 1936. The shearing resistance of saturated soils and the angle between the planes of shear, in: Proceedings of the International Conference on Soil Mechanics and Foundation Engineering, Harvard University Press, Cambridge, MA. pp. 54–56.

Tian, Y., Cassidy, M.J., Randolph, M.F., Wang, D., Gaudin, C., 2014. A simple implementation of ritss and its application in large deformation analysis. Computers and Geotechnics 56, 160–167.

Tingsanchali, T., Chinnarasri, C., 2001. Numerical modelling of dam failure due to flow overtopping. Hydrological Sciences Journal 46, 113–130.

Tran, D.K., Ralaizafisoloarivony, N., Charlier, R., Mercatoris, B., Léonard, A., Toye, D., Degré, A., 2019. Studying the effect of desiccation cracking on the evaporation process of a Luvisol – From a small-scale experimental and numerical approach. Soil Tillage Res. 193, 142–152.

Tsai, T.L., Chen, H.E., Yang, J.C., 2008. Numerical modeling of rainstorm-induced shallow landslides in saturated and unsaturated soils. Environmental Geology 55, 1269–1277.

United Nations Office for Disaster Risk Reduction, 2017. The sendai framework terminology on disaster risk reduction: Structural and non-structural measures. URL: `https://www.undrr.org/terminology/structural-and-non-structural-measures`. accessed 6 August 2025.

Van Emelen, S., Soares-Frazão, S., Riahi-Nezhad, C.K., Hanif Chaudhry, M., Imran, J., Zech, Y., 2012. Simulations of the New Orleans 17th Street Canal breach flood. Journal of Hydraulic Research 50, 70–81.

Van Emelen, S., Zech, Y., Soares-Frazão, S., 2015. Impact of sediment transport formulations on breaching modelling. Journal of Hydraulic Research 53, 60–72.

Van Emelen, S., Zech, Y., Soares-Frazão, S., 2016. Closure to "impact of sediment transport formulations on breaching modelling". Journal of Hydraulic Research 54, 481–483.

Vanapalli, S.K., Fredlund, D.G., Pufahl, D.E., Clifton, A.W., 1996. Model for the prediction of shear strength with respect to soil suction. Canadian Geotechnical Journal 33, 379–392.

Vardoulakis, I., 1985. Stability and bifurcation of undrained, plane rectilinear deformations on water-saturated granular soils. Int. J. Numer. Anal. Methods Geomech. 9, 399–414.

Visser, P.J., 1998. Breach growth in sand-dikes. PhD thesis, Delft University of Technology.

Wallace, T., Crawford-Flett, K., Wilson, M., Logan, T., 2024. A framework for modelling the probability of flooding under levee breaching. Journal of Flood Risk Management 17, e12988.

Wang, B., Vardon, P.J., Hicks, M.A., 2016. Investigation of retrogressive and progressive slope failure mechanisms using the material point method. Computer and Geotechnics 78, 88–98.

Wang, W., Sluys, L., de Borst, R., 1997. Viscoplasticity for instabilities due to strain softening and strain-rate softening. International Journal for Numerical Methods in Engineering 40, 3839–3864.

Weill, S., Mouche, E., Patin, J., 2009. A generalized Richards equation for surface/subsurface flow modelling. Journal of Hydrology 366, 9–20.

Weynants, M., Vereecken, H., Javaux, M., 2009. Revisiting Vereecken Pedotransfer Functions: Introducing a Closed-Form Hydraulic Model. Vadose Zone Journal 8, 86–95.

Wilkins, A., Spencer, B.W., Jain, A., Gencturk, B., 2019. A method for smoothing multiple yield functions. International Journal for Numerical Methods in Engineering 121, 434–449.

Wu, W., Marsooli, R., He, Z., 2012. Depth-averaged two-dimensional model of unsteady flow and sediment transport due to noncohesive embankment break/breaching. Journal of Hydraulic Engineering 138, 503–516.

Xue, R., Zhang, X., Cai, Y., Wang, M., Deng, Q., Zhang, H., Kawaike, K., 2021. Numerical simulation of landslide dam overtopping failure considering headward erosion. J. Hydrol. 601, 126608.

Yang, J., Soares-Frazao, S., Shi, Z., Shen, D., 2024. A 2d numerical model for simulating landslide dam failure and induced morphological changes considering multi-layer and non-uniform sediments. Journal of Hydroinformatics 26, 1606–1628.

Yu, H.S., Salgado, R., Sloan, S.W., Kim, J.M., 1998. Limit Analysis versus Limit Equilibrium for Slope Stability. Journal of Geotechnical and Geoenvironmental Engineering 124, 1–11.

Yuan, W.H., Liu, K., Zhang, W., Dai, B., Wang, Y., 2020. Dynamic modeling of large deformation slope failure using smoothed particle finite element method. Landslides 17, 1591–1603.

Zhang, X., Krabbenhoft, K., Sheng, D., Li, W., 2015. Numerical simulation of a flow-like landslide using the particle finite element method. Computational Mechanics 55, 167–177.

Zhang, Y., Chen, G., Hu, J., Chen, X., Yang, W., Tao, A., Zheng, J., 2017. Experimental study on mechanism of sea-dike failure due to wave overtopping. Applied Ocean Research 68, 171–181.

Zhang, Y., Zhang, X., Nguyen, H., Li, X., Wang, L., 2023. An implicit 3d nodal integration based pfem (n-pfem) of natural temporal stability for dynamic analysis of granular flow and landslide problems. Computers and Geotechnics 159, 105434.

Zhong, Q.m., Chen, S.s., Deng, Z., 2017. Numerical model for homogeneous cohesive dam breaching due to overtopping failure. Journal of Mountain Science 14, 571–580.

Zhou, G.G.D., Zhou, M., Shrestha, M.S., Song, D., Choi, C.E., Cui, K.F.E., Peng, M., Shi, Z., Zhu, X., Chen, H., 2019. Experimental investigation on the longitudinal evolution of landslide dam breaching and outburst floods. Geomorphology 334, 29–43.

Zhu, Y., 2006. Breach growth in clay-dikes. Ph.D. thesis. TUDelft.

Özer, I.E., van Damme, M., Jonkman, S.N., 2020. Towards an International Levee Performance Database (ILPD) and Its Use for Macro-Scale Analysis of Levee Breaches and Failures. Water 12, 119.